Doctoral theses at NTNU, 2012:261

Pål Henrik Enger Finstad

# Secondary Flow Fields in Francis Turbines

## Mapping and analyzing dynamics in rotor-stator interaction and draft tube flow with novel methods

Doctoral Thesis

Pål Henrik Enger Finstad

ISBN 978-82-471-3832-8
ISBN 978-82-471-3833-5
ISSN 1503-8181

NTNU – Trondheim
Norwegian University of
Science and Technology

NTNU
Norwegian University of Science and Technology
Thesis for the degree of Philosophiae Doctor
Faculty of Engineering Science & Technology
Department of Energy and Process Engineering

Doctoral theses at NTNU, 2012:261

NTNU

NTNU – Trondheim
Norwegian University of
Science and Technology

Pål Henrik Enger Finstad

# Secondary Flow Fields in Francis Turbines

## Mapping and analyzing dynamics in rotor-stator interaction and draft tube flow with novel methods

Thesis for the degree of Philosophiae Doctor

Trondheim, october 2012

Norwegian University of Science and Technology
Faculty of Engineering Science & Technology
Department of Energy and Process Engineering

**NTNU – Trondheim**
Norwegian University of
Science and Technology

**NTNU**
Norwegian University of Science and Technology

Thesis for the degree of Philosophiae Doctor

Faculty of Engineering Science & Technology
Department of Energy and Process Engineering

© Pål Henrik Enger Finstad

ISBN 978-82-471-3832-8
ISBN 978-82-471-3833-5
ISSN 1503-8181

Doctoral theses at NTNU, 2012:261

Printed by Skipnes Kommunikasjon as

# Abstract

Hydropower, and especially Francis turbines, for electricity production has a history of more than 100 years and has proved to be one of the most efficient ways of utilizing renewable energy for electricity production. Yet, there are several problems to be solved regarding producing and running cost effective, high efficient and durable turbines. Secondary flow fields are all unwanted flow patterns present in the turbine. The major fluctuating flow fields in Francis turbines are caused by rotor-stator interaction when the runner vane passes the guide vane wake and the swirling flow in the draft tube at off-design operation. Such flow fields have a negative effect in terms of causing losses, vibrations, noise or damage to the turbine structure. The flow through a Francis turbine, especially at off-design operation is not optimal, and is characterized by a dynamic and fluctuating flow pattern. It is difficult, but important to understand the behavior of the dynamics to better predict the negative effects of the fluctuating flows, and also in order to minimize or remove the unwanted effects by e.g. geometry modifying or flow control.

This work aims to introduce new methods helping to obtain a deeper understanding on the dynamics present in wake flow and in rotor-stator interaction. It is investigated whether vortex generators, VGs, can have a positive effect on the wake with respect to rotor-stator interaction. Experimental TRPIV (Transient Particle Image Velocimetry) wake data recorded at 10 000 Samples/sec from a cylinder in a stream at 1-6 m/s and hydrofoils in a stream at 9 m/s are studied. Both plain hydrofoils, and hydrofoils where Vortex Generators – VGs are mounted are used in the study. The Reynolds number is in the range of $1.2 \cdot 10^4 – 7.3 \cdot 10^5$. The velocity fields from both the cylinder and the hydrofoils are used as inlet boundary condition in a 2D CFD-case simulating rotor-stator interaction. The characteristic frequencies of the system are the vortex shedding frequency and the rotor passing frequency. The cylinder case shows that leading edge stagnation point moves with the vortex shedding frequency. The shedding frequency is also found in leading edge pressure and lift fluctuations, but the rotor passing frequency is found more dominant. Only the rotor passing frequency and its multiples is observed when looking into the same fluctuations for the hydrofoil case. Vortex shedding is only observed at Angle of Attack - AoA=8 degrees for the hydrofoil. In terms of rotor leading

edge pressure reduction, only AoA=0 and AoA=2 showed equal or slightly improvements with VGs. A time averaged wake is also used as input in the CFD for AoA=4 and it shows large amplitude reduction when looking at the leading edge pressure and lift oscillations.

Proportional Orthogonal Decomposition – POD is introduced to reveal flow structures and their corresponding energy in the wake flow. POD shows that up to 65 % of the total energy is located in the two first POD modes for the cylinder wake. Up to 18 % of the total energy is located in the two first modes for the hydrofoil at AoA=8 degrees where vortex shedding is present. The vortex generators prove to break the characteristic shedding pattern and move the early mode energy to later modes and reduce the energy content in the two first modes from 18 % to 8 % at AoA=8. At other AoAs only slight change in the energy distribution was observed due to the vortex generators.

The second part of the thesis is focusing on measurements and investigation of draft tube flow dynamics. Pairwise radial dynamic measurements of the swirling draft tube flow is done at the 25 MW Svorka power plant in Surnadal operating at 48 % load, at 6 radial and 7 angular positions. The data is analyzed with traditional methods as well as with POD. The pressure fluctuations were found to peak at R5, at 83 % of the radius. The Rheingans frequency is found to be the only distinctive peak, and is very dominant in the pressure signal. The POD addressed 52 % of the total pressure variance to the azimuthal mode 1. As the POD will pin point structures of high energy it is desired to be able to use this information in active flow control applications. This is difficult as the measurements in the draft tube are performed manually and are time consuming. The resulting eigenfunctions from the POD measured at one operating point can later be coupled with a single wall pressure transmitter through Linear Stochastic Estimation – LSE in order to give POD results for other operating points. This work presents the first step of required measurements in one operational point in order to verify the use of POD in draft tube flow. Further development of POD for use in active flow control through LSE will be a continuation of this work.

# Acknowledgements

The study presented has been accomplished at the Water power laboratory (Vannkraftlaboratoriet), department of energy and process engineering at the Norwegian University of Science and Technology (NTNU) in Trondheim from fall 2009 to fall 2012.

This work was not possible without contribution and support from friends and colleagues. I would specially like to thank my supervisors Morten Kjeldsen (FDB) and Torbjørn Nielsen (NTNU) for valuable supervision throughout this work. Also the other employees in FDB, Håkon Hjort Francke and Jarle Vikør Ekanger have been of great value, especially helping at field measurements and with data acquisition.

The experimental work had not been possible without kind help from the mechanics, Joar Grilstad, Trygve Opland, Halvor Haukvik and Bård Brandåstrø. Thanks also a lot for positive attitude regarding my never ending bike repairs and other small fixes in the lab.

Roger Arndt has been of great help on the wake papers, and as he together with Morten Kjeldsen and Bjarte Grytli Seim helped performing the experimental work on wake flow used in the thesis. I want to express my gratitude to Murat Tutkun (FFI) for introducing me and helping me out with the POD analysis.

Thanks to Statkraft and Svorka Energi for letting us drill holes in the draft tube and measure at Svorka Power plant. And thanks to Energi Norge for funding the project.

The work has given both good and frustrating moments. I'm very happy to have had nice colleagues around me for valuable on- and off-topic discussions. Thank you Mette Eltvik, Einar Kobro, Jørgen Ramdal, Idun Østgård, Grunde Olimstad, Lars Frøyd, Celine Faudot, Pål-Tore Storli, Bjørn Winther Solemslie and Eve Walseth.

# List of figures

# List of tables

# Nomenclature

| | |
|---|---|
| $a$ | = Constant in POD integral |
| $a_0$ | = Constant in curve fitting to a standard wake profile |
| $a_1$ | = Constant in curve fitting to a standard wake profile |
| $a_2$ | = Constant in curve fitting to a standard wake profile |
| $A$ | = Area |
| α | = Maximization constant in POD |
| b | = Foil span |
| $b_0$ | = Inlet boundary |
| β | = Angle between rotor velocity and relative velocity |
| $c$ | = Absolute velocity |
| $cm$ | = Meridional velocity |
| $cu$ | = Absolute velocity in peripheral direction |
| $C_D$ | = Drag coefficient |
| $C_L$ | = Lift coefficient |
| $D,d$ | = Diameter |
| $D_F$ | = Drag force |
| $Dm$ | = Integration domain in POD |
| $\delta$ | = Boundary layer thickness |
| $\delta^*$ | = Boundary layer displacement thickness |
| $E$ | = Total energy |
| $f$ | = Frequency |
| $f_n$ | = Rotational frequency |
| $f_R$ | = Rheingans frequency |
| $F$ | = Force |
| $k$ | = Chord length |
| $L$ | = Lift force |
| $Le$ | = Length |
| ι | = Integral length scale |
| $\varepsilon$ | = POD uncertainty based on number of blocks |
| $\rho$ | = Density |
| $\lambda$ | = Eigenmode in POD |
| $\phi$ | = Eigenfunction in POD |
| $\nu$ | = Kinematic viscosity |

| | |
|---|---|
| $\vartheta$ | = Angular direction |
| $\psi$ | = Peak to peak value |
| $m$ | = Number (azimuthal modes) |
| $n$ | = Number (samples, POD modes) |
| $\eta_F$ | = Lift to drag ratio, hydrofoil efficiency |
| $p$ | = Pressure |
| $\tilde{p}$ | = Variable in POD |
| $\hat{p}$ | = Fourier coefficient of pressure |
| $plain$ | = Plain hydrofoil case |
| $R,r$ | = Radius |
| $R.,.$ | = Kernel in POD |
| $Re$ | = Reynolds number |
| $S$ | = Cross spectra |
| $s_0$ | = Distance from cylinder center to inlet boundary |
| $St$ | = Strouhal number |
| $t$ | = Time |
| $T$ | = Time, Block length in POD |
| $u$ | = Local velocity |
| $u1,u2,...u6$ | = Case 1-6 where digit represent free stream velocity |
| $U$ | = Free stream velocity |
| $V1$ | = Hydrofoil with vortex generators V1mm |
| $w$ | = Relative velocity |
| $W$ | = Modified POD kernel |
| $\Lambda$ | = Integral time scale |
| $x$ | = Downstream position |
| $y$ | = Vertical position |

## Subscripts

| | |
|---|---|
| $0$ | = Reference case, related to free stream velocity |
| $1$ | = Inlet position |
| $2$ | = Outlet position |
| $D$ | = Drag component |
| $gvi$ | = Guide vane inlet |
| $gvo$ | = Guide vane outlet |

| | |
|---|---|
| *GV* | = Guide vane |
| *i* | = Index |
| *j* | = Index |
| *L* | = Lift component |
| *m* | = Meridian |
| *RV* | = Runner vane |
| *s* | = Samples |
| *sc* | = Spiral Casing |
| *svi* | = Stay vane inlet |
| *svo* | = Stay vane outlet |
| wake | = When inside wake |

## Abbreviations

| | |
|---|---|
| AoA | = Angle of attack |
| BEP | = Best efficiency point |
| CFD | = Computational Fluid Dynamic |
| FFT | = Fast Fourier Transform |
| LSE | = Linear stochastic estimation |
| norm | = Normalized |
| NTNU | = Norges Teknisk Naturvitenskapelige Universitet |
| PIV | = Particle Image Velocimetry |
| POD | = Proportional Orthogonal Decomposition |
| SAFL | = Saint Anthony Falls Laboratory |
| stag | = Stagnation |
| VG | = Vortex generator |

# 1 Introduction

## 1.1 Structure of the thesis

The thesis is dealing with two major topics within secondary flow fields in Francis turbines and is presented as follows:

- **Wake flow/rotor-stator interaction**
  - Paper based
- **Draft tube flow**
  - Monograph

*Chapter 1:* Introduction to wake flow study and draft tube study

*Chapter 2:* Theory and analysis methods used in wake flow/rotor-stator interaction, POD and draft tube flow

*Chapter 3:* Experimental work on wake flow/rotor-stator interaction

*Chapter 4:* Paper 1 on wake flow/rotor-stator interaction

*Chapter* 5: Paper 2 on wake flow/rotor-stator interaction

*Chapter 6:* Draft tube flow. Experimental work, results, discussion, conclusions

*Chapter 7:* Discussion of findings in the total work and connection of the two parts

*Chapter 8:* Major conclusions of wake flow study and draft tube study

*Chapter 9:* Further work for both parts

*Appendix:* Additional information

## 1.2 Background

Hydropower is by far the most important supplier of electrical energy in Norway. In a normal year Norway produce 120 TWh (99 %) of the electrical energy by hydro power [1]. Not only is hydro power a green energy source, but its possibilities of storing water in a reservoir and short start/stop time makes it also crucial in governing the electricity system. The Francis turbine is the most important hydro turbine in Norway in terms of energy production as it can operate at a wide range of heads, 30-750 m, with high efficiency [2].

An important energy legislation (§ energiloven) was introduced in 1991. The electricity market was previously strongly controlled by the Norwegian government. The legislation opened up for third parties to take part in the electricity market. Norway was connected to the Danish electricity grid in 1977 by two High Voltage Direct Current - HVDC (Skagerak 1 and Skagerak 2) cables in already in 1977. A new cable (Skagerak 3) was installed in 1993. The legislation lead to increased electricity prices in Norway. Following from the legislation in addition to a new HVDC cable to Denmark was a new way of operating the power plants. Previously, the power plants were run around BEP in which they were designed for. The production had to adapt to the price and demand in a different way leading to more operation off BEP and more start/stop of the power plants.

As money plays a more important role in the power production, the hunt of high efficiency and cost effective turbines has led to thinner blades and more compact turbine construction. This in addition to the change in operation of the power plants has contributed to a rise in structural failure the last years.

## 1.1 Motivation

Cracks, fatigue and structural failure all happen due to heavier loads on the material than it can withstand. It is pressure forces from the water flowing through the turbine that adds the load to the turbine structure. If the load is constant or changes linearly it is easy to construct a structure which can take the load. Since the flow through a Francis turbine is complex and highly dynamic, it is difficult to predict how the pressure forces act on the turbine structure. Cracks and mechanical failure can be caused both by high amplitude

and low cycle pressure fluctuations, as well as by low amplitude and high cycle pressure fluctuation. The latter is the source to high cycle fatigue. Unwanted flow patterns in the turbine which cause some type of negative flow effect is called **secondary flow fields**. The secondary flow fields often create disturbing and highly dynamic flow patterns causing losses, noise and vibrations. The behavior and effect of the secondary flow fields are not fully understood.

The motivation of the work is to investigate secondary flow fields with focus on the dynamics in the flow, since the dynamic part of the phenomena are believed to play a major role in the negative effects observed. It is also believed that introducing novel methods to the investigations can help explaining and lead to better understanding of the phenomena. By gaining a deeper understanding on the dynamics in secondary flow fields it is hoped this will lead to better knowledge on how to predict the loads in a turbine. More precise load prediction makes it easier to design or modify high efficiency turbines to avoid structural failure. It is also believed that good methods for prediction of the dynamics can be implemented in flow control devices where the aim is to decrease or terminate the unwanted flow fields.

## 1.2 Scope of work

These thesis will focus on the following two secondary flow phenomena present in the Francis turbine:

- **Wake flow and Rotor-stator interaction**
- **Swirling draft tube flow**

The major focus is to introduce new analysis methods to study the dynamics, which can help to obtain a deeper understanding of the behavior and the consequences of having a dynamic part in the above mentioned phenomena. Time averaged analysis is also performed to complete the total understanding. Wake flow and rotor-stator interaction are closely coupled, and are partly investigated together. Experimental data of cylinder and hydrofoil wakes is collected in order to study wake dynamics. Further investigations are done by introducing the experimental wake data into the computational domain in order to study the effect of rotor stator interaction in the cylinder and hydrofoil wakes. In this context it is of special interest to investigate how mounting of vortex generators on hydrofoils will influence the effect on dynamic wake flow

and rotor stator interaction. If there are energy wise large and dominant structures in the wake it is believed that the vortex generators can disturb the large scale flow structures and redistribute the energy over smaller flow structures.

An important aspect of the work in addition to better understand the importance of dynamic behavior in secondary flow fields is to introduce and verify novel and advanced analysis methods into the study. The methods referred to are TRPIV measurements in combination with CFD and Proportional Orthogonal Decomposition, POD.

Draft tube flow is investigated at a full size power plant. While dynamic draft tube measurements earlier are performed at the draft tube wall, two measuring probes are developed to be inserted through holes in the draft tube wall and measure dynamic pressure in radial positions. The data is later analyzed with traditional methods in addition to the POD method.

Introducing POD into the studies of wake- and draft tube dynamics can be an important factor in controlling possible flow control applications. Water injection is already installed as active flow control in the turbine where the draft tube measurements took place. The water injection is now controlled by pressure pulsation and vibration measurements. The resulting eigenfunctions from the POD-analysis can be coupled to a single wall pressure measurement through linear stochastic estimation - LSE, and give more detailed information about the flow structures present in the draft tube with respect to energy for all operational ranges. The POD-results can give additional information to better control the water injection system or other active flow control.

The main objectives of the thesis can be summarized as follows:

- Analyze dynamic behavior in specified secondary flow fields
- Combine and verify experimental PIV-velocity fields and CFD
- Verify the effect of vortex generators on wake dynamics
- Perform dynamic radial measurements in the draft tube
- Introduce and verify the use of POD in the study of secondary flow fields
- Obtain POD eigenfunctions for future use in linear stochastic estimation

## 1.3 Methods

The study is based on experimental work from both the laboratory and the field. The wake flow study data are collected in the high speed cavitation tunnel in the laboratory at SAFL in Minnesota. Draft tube data are collected at Svorka power plant close to Surnadal in Norway. Much of the study is based on analysis of the experimental data, but numerical simulations, CFD, in combination with the experimental wake data is also a part of the work performed. Proportional Orthogonal Decomposition, POD, is introduced to both experimental data collections as a tool to map dynamic structures in the flows. POD is not commonly used in the hydro power industry, but is often used in studies of turbulent jets, boundary layers, turbulence, etc.

## 1.4 Limitations

Secondary flow fields consist of several topics where the most important are presented in chapter 2.2. No other secondary flow fields than the one mentioned in chapter 1.2 will be dealt with in this thesis.

In terms of dynamic behavior of wakes and rotor stator interaction, the flow phenomena of interest is isolated, without any disturbances or influence from system dynamics such as water hammer or U-tube oscillations normally present in a hydro power plant. The experiments were performed in an water tunnel at SAFL.

The draft tube data are collected at a full scale power plant, hence the data can be influenced by other dynamic phenomena in the system. Though were the tests performed at steady state conditions with no governing. This to ensure similar conditions and reliable data for the flow fields of interest.

## 1.5 Previous work

Many studies have been made on secondary flow fields in terms of wake flow, rotor-stator interaction and draft tube flow. The water power laboratory at NTNU has traditions in studying these and related phenomena, together with several international scientific institutions. At the water power laboratory at NTNU the most relevant studies are listed below.

**Antonsen's** study "*Unsteady flow in wicket gate and runner with focus on static and dynamic load on runner"* [3] investigated the effect of profiled guide vanes with respect to static and dynamic load on the runner and how it affects the wake. By profiling the guide vane one can create a pressure field contrary to the pressure field caused by the flow passing the guide vane cascade which cause a non-uniform pressure and velocity distribution, and level the non-uniform pressure field.

**Chen** and her "*Theoretical and experimental study of flow through the double cascade of a Francis Turbine" [*4] study looked into the flow field behavior in a double cascade including pressure measurements along wetted surfaces showing the non-uniformity of the inlet flow in a Francis Turbine.

**Larsson** made a study called "*Experimental and theoretical analysis of inlet flow of a Francis Turbine Runner" [*5]. He studied the unsteady inlet flow of a Francis pump turbine where he combined LDA measurements and CFD calculations. He found that the flow in the vane less space could fluctuate up to 15 % of the mean flow due to pressure pulses originating from the rotor-stator interaction. He also found that the pressure and velocity field drastically changed character by increasing the rotational speed 20 % above BEP.

**Jernsletten's** study called *"Analysis of a non- stationary flow in a Francis reversible pump turbine runner"* [6] found that the pressure pulses on the runner was reduced by 30 % by increasing the distance between the guide vanes and runner by 5.1 mm.

**Kobro** wrote the thesis called *"Measurements of pressure pulsations in Francis Turbines"* [7] where he performed onboard dynamic pressure and strain measurements on both model and prototype of the Tokke Francis turbine as it was refurbished. The load addressed back to blade passing through the guide vane wake proved to be the most severe source of dynamic pressure in the runner. Pressure pulsations from the rotating vortex rope in the draft tube was also found to propagate upstream into the runner, but did not appear as a significant frequency in the runner strain measurements.

**Vekve** investigated draft tube flow in a study called *"An experimental investigation of draft tube flow"* [8]. He measured dynamic draft tube pressure on one Francis pump turbine model, and on two prototype Francis turbines with different runner cones. He also measured the velocity distribution by LDV in the model. The cylindrical inserts as an extension of the shaft in the draft tube were found to suppress the rotating vortex rope and the pressure fluctuations in the model, but the inserts in the prototypes were small and had little effect at part load. One of the prototypes showed improved performance at over load.

**Oledal** included both numerical simulations as well as experimental work in his thesis "*Cavitation in complex separated flows" [9].* He studied cavitated vortex break down over delta shaped vortex generators. A major finding was that re-entrant jets were found to be frequently present in the vortex upstream the vortex generator apex when breakdown appeared above the model. It was found that the transition from vortex to bubble cavitation is determined by the position of breakdown. Cavities were also observed in secondary vortices when breakdown occurred above the vortex generator or close to the trailing edge. Oledal also included a study of the flow field around cavitation inducers on a rotating disk set up. The circular cavitation inducer proved to be superior over other inducers due to efficient transport of bubbles from generation location to where they collapse.

There are also several publications on wake flow, rotor-stator interaction, cavitation and draft tube flow internationally. Especially the scientific group at EPFL in Lausanne has come up with much important research especially on wake flow, vortex shedding and cavitation the past years.

**Ausoni** published his doctoral thesis in 2009 with the title, *"Turbulent vortex shedding from a blunt trailing edge hydrofoil"* [10]. Experiments on a symmetrical hydrofoil with a blunt trailing edge are carried out using advanced equipment like PIV, LDV, laser doppler vibrometer and high speed camera. Lock-off mode is where no resonance frequency of the hydrofoil is excited. In the cavitation free regime in this mode, it is found that the vortex shedding frequency is quasi-linearly dependent on the free stream velocity. This is according to earlier findings. It is also found that the shedding frequency exhibit

strong span-wise instabilities and dislocations in the lock-off mode. When pressure falls below vapor pressure cavitation occurs. For the lock-off mode the cavitation inception is dependent on the square root of the Reynolds number according to previous models. For lock-in modes, the vortex shedding is strongly amplified by the resonance frequency. Regarding the cavitation inception index and the trailing edge displacement velocity, a new correlation relationship which includes the lock-off and lock-in conditions is proposed and validated. In addition, the transverse velocity of the trailing edge increases the vortex strength linearly. For fully developed cavitation it is found a 15 % increase in vortex shedding frequency.

**Ausoni** [11] also investigates the roughness effect of the boundary layer on von Karman vortex shedding off a hydrofoil. He finds that a turbulent boundary layer by a rough leading edge surface reduces the flow induced vibrations of the foil.

**Zobeiri** [12, 13] studied the vortex shedding from blunt and oblique trailing edge hydrofoils. The study takes advantage of both PIV and POD. He found that the truncated trailing edge reduces the vortex shedding off the foil compared to a blunt trailing edge. This is also in good agreement with an early and important study made by Heskestad [14] in 1960.

A numerous of additional publications can be addressed back to EPFL with where topics as fluid structure interaction, vortex shedding and cavitation have been investigated. See [10, 15-21].

**Heskestad** and **Olberts** investigated experimentally the relation between vortex shedding frequency and flow velocity on different trailing edge geometries of flat plates. The plates were supposed to simulate the flow conditions of a hydraulic turbine blade. They found that the shedding frequency cannot be determined accurately by the Strouhal formula or a modification thereof. The shedding frequency varied linearly with flow speed in a given flow speed area (7,6 – 16,7 fps) for a given trailing edge geometry. They also found a resonance area where the linear relation is void, which is also referred to as the lock-in area. Major focus was not on the resonance area, rather on how various trailing edges resulted in different frequencies and amplitude of the shed vortices. A

table of the various trailing edge geometries and corresponding frequencies and amplitudes is presented. The reference geometry is the blunt flat plate, and some geometries proved to give negligible amplitude. Trailing edges result in greatest vortex strengths during non-resonance, induce the greatest vibration amplitudes during resonance, and thus greatest excitation forces. [14]

**Arndt** [22] and his research community at the SAFL cavitation tunnel have done thorough investigation on vorticial cavitation properties of flow fields past immersed bodies as e.g. hydrofoils, propellers and cylinders. Both experimental and numerical work is carried out, but due to the good experimental facilities with the special high speed cavitation tunnel, most effort is put into the experimental parts. Extensive work is done on fundamental flow patterns occurring on propellers and hydro turbines where tip and hub vortex are important topics. A special focus is put into whether cavitation can contribute to positive flow properties, and not only be a disturbing and destructive phenomenon. This can be achieved through active flow control where turbulence or cavitation is triggered to obtain a desired effect. Several articles are published on the mentioned topics. A review called “Cavitation in vorticial flows” [22] gives a good impression of cavitational aspects dealt with at SAFL.

**Vu** and **Nennemann** [15] have done numerical analysis of the vortex shedding off a guide vane in a guide vane/runner cascade. CFD prediction of the hydrofoil natural frequency is estimated within ±18 % of earlier measured values. To surely avoid cavitation, the vortex shedding should be beyond at least ±20 % of the vane natural frequency to avoid resonance.

**Barbi** [23] investigated vortex shedding and lock-in of a cylinder in oscillating flow in both water and air. Results from both air and water are in good coherence. Earlier knowledge stated that bluff bodies shed vortices at their natural frequency of shedding, at the frequency or half of the frequency of an external oscillation for transverse oscillation. For in-line oscillation, half of this value. This report states that the shedding frequency varies smoothly with the driving frequency, until it locks on a sub harmonic frequency. At the lowest frequency of lock-in, vortices are shed simultaneously on both sides of the cylinder. Alternating shedding is observed at higher driving frequencies.

**Mutschke** [24] investigates vortex shedding and separation off a hydrofoil affected by Lorenz forces. The work is related to that previous time periodic air injection or suction can enhance lift of airfoils in certain flow regimes. The Lorenz force originates from surface-mounted actuators of permanent magnets on a NACA 0017 hydrofoil and electrodes in a weakly conducting fluid as in seawater. Numerical analysis has been carried out for laminar low Reynolds number flows. Steady strong applied Lorenz force can depress separation at an angle of 30 deg. Oscillatory control on the front part of the suction side struggles with vortex shedding, but proper chosen excitation frequencies gives more effective control by oscillatory forces, than steady forces in terms of moment coefficient. Oscillatory Lorenz forces do not totally suppress separation. Weak oscillating force control can lead to lift enhancements around the natural shedding frequency. The optimum lift band is found around the natural shedding frequency. As for turbulent high Reynolds number flows, both steady and oscillatory control of Lorenz-force has similar relation between lift and drag. Increase of lift is associated with increase in drag, although airfoil efficiency increases.

**Miklosovic** [25] brought aspects from the aquatic life into the laboratory by comparing flippers with leading edge tubercles similar to those the humpback whale has, against ordinary smooth flippers without tubercles. The ordinary flipper stalled at around 11 degrees while the flipper with tubercles proved to keep attached flow up to angle of attack of 17 deg. As well it gave slightly lower drag at intermediate angles of attack. The aerodynamic efficiency L/D is decreased at some incident angles, but overall shows a better performance for the scalloped model, especially at higher angles of attack. The peak efficiency is still at the same angle of attack, but with slightly higher value. Small vortices are formed between the tubercles, similar to what vortex generators do on an airplane wing. Enhanced lift and drag performance of the tubercles are similar to the vortex generators on airplane wings, which delay flow separation on the wing.

**Nierop** [26] developed an aerodynamic model based on the tubercle experiments carried out by Miklosovic. The experiments showed that humpback whale tubercles on the leading edge of a flipper or hydrofoil will

delay stall. The model predicts gradual stall and no sudden stall for large angles of attack, as the smooth hydrofoil does. A flattened lift curve for increasing bump amplitude is observed. Stall delay is found independent of bump wavelength according to experiments. Increased stall properties contributes to better maneuverability and less unpredictability in lift at high angles of attack.

Proportional Orthogonal Decomposition, POD is utilized in several turbulence studies, but not often directly related to hydro power research. Some important publications are listed below.

**Lumley** [27-29] first introduced POD in 1967 in order to decompose the quantitative flow field to identify and study the dynamics of large scales structures of a turbulent flow.

Especially **Glauser** and **George** brought POD to new applications in the late 1980's by utilizing the method for looking into the dynamics of e.g. turbulent jets which is similar to the flow regime found in the draft tube of a Francis turbine. They also modified the method to fit better to the new applications [30-33].

**Tutkun** [34] has worked on axisymmetric flow fields in the wake behind a disk which in theory is very similar to the flow field present in a draft tube as the constraints are the same. For both cases it yields that the two-point correlation is homogenous in the azimuthal direction and periodic over one revolution in this direction.

Others utilizing the POD analysis are **Sirovich** [35], **Arndt** [36, 37], and **Lu [38].**

# 2 Theory and analysis

## 2.1 Francis turbine theory

This chapter is based on [2, 39, 40] where the theory part is elaborated in closer detail. The Francis turbine is a radial turbine, first developed by James B. Francis in 1849. It has a radial inlet an axial outlet, and is suited for head in the range 30-750 m. At BEP the Francis turbine can reach efficiencies of more than 95 %.

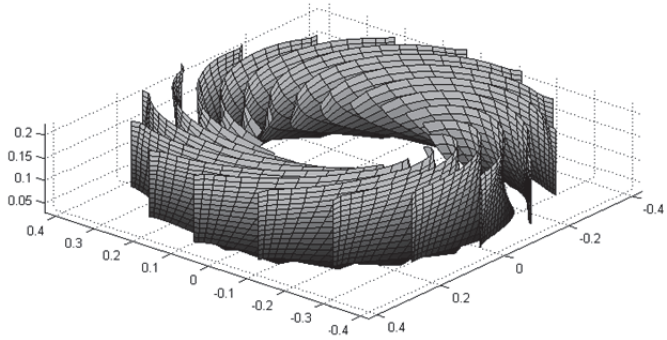


**Figure 1 – Example of runner design from Jøndalsåa power plant**

The main parts of the Francis turbine are:

- **A spiral case** which encloses the inlet and leads the water radial into the inlet of the stay vanes in the turbine.
- **The stay vanes** have the purpose of keeping the hub and shroud together. The stay vanes are stationary and are shaped to lead the water in a free vortex path.
- **The guide vanes** come after the stay vanes with the purpose of controlling the flow rate of the turbine as well as guide the water onto the runner vanes.
- **The runner** is the core of the turbine and has the purpose to transform the pressure- and kinetic energy to rotating mechanical energy. The mechanical energy is converted by the generator to electrical energy.
- **The draft tube** is a diffusor and is placed at the outlet of the runner and recovers unused kinetic energy back to pressure energy. To utilize as much energy as possible, it is normal that the pressure at the runner exit is below atmospheric pressure. The water still has a bit of kinetic energy left at the outlet, and this energy is converted back to pressure

energy to meet the atmospheric pressure level at the end of the draft tube.

The Francis turbine is a reaction turbine and is usually designed so the energy at the inlet consists of 50 % pressure energy and 50 % kinetic energy.

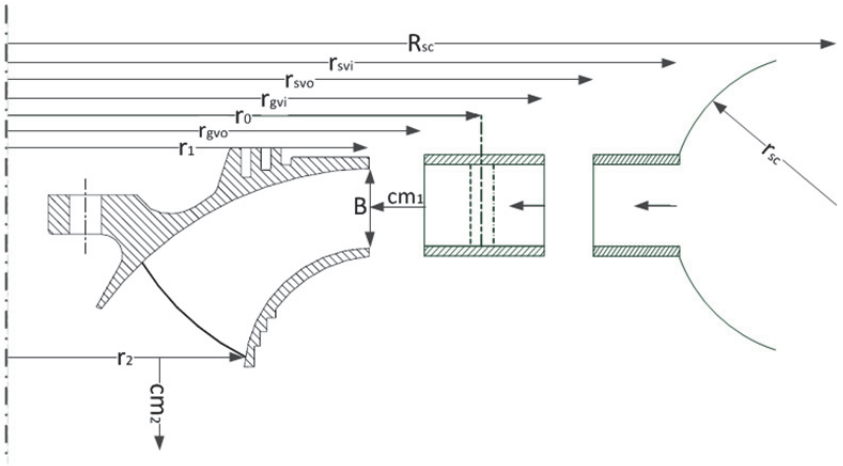


**Figure 2 – Axial view of half the Francis turbine**

The velocities entering and exiting the Francis turbine can be drawn in a 2-D diagram as shown in Figure 3.

### 2.1.1 Velocity components

At BEP the Francis turbine is designed with no rotation at the outlet. This implies that $cu_2$=0. When running outside BEP rotation of the exiting water occurs as the blades are fixed, and the rotational speed is constant to keep the frequency constant at 50 Hz.

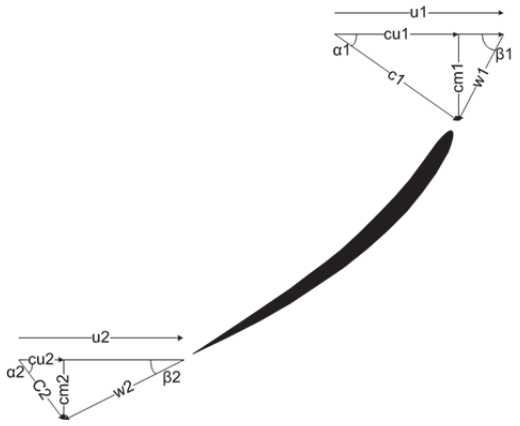


**Figure 3 – Velocity diagram for a Francis runner**

## 2.2 Secondary flows in Francis turbines

Secondary flow fields are unwanted or unfavorable flow patterns. Such flow fields have a negative effect on the application in terms of efficiency loss, noise, vibrations, loss of fluid, increase in temperature etc. In Francis turbines there are several flow patterns referred to as secondary flow fields. Of the most important are:

- **Wake flow**

  There are three blades in a Francis turbine that create wakes. Those are the stay vanes, guide vanes and the runner vanes. Most important is the guide vane wake as this wake is interfered by the passing of the runner vane.

- **Rotor-stator interaction**

  Because the guide vane (stator) creates a wake with a velocity deficit, a disturbance occurs as the runner vane (rotor) passes through this wake. The rotor experiences a reduction of inlet velocity as it moves into the wake, hence also a pressure increase as those variables are strongly coupled. If the wake profile is smooth the pressure variation will also be smooth. The case is that the velocity variation in the wake, hence also the pressure variation, is strongly fluctuating. The rotor experiences this pressure pulse every time it passes a stator. If the pressure fluctuations in the wake coincide with the rotor passing frequency or other frequencies in the system the pressure pulse can be strongly amplified.

- **Leakage flow**

  Leakage is always present between the turbine and the hub/ring. Since the turbine is rotating there must be a tiny gap between the turbine and hub/ring where water will flow due to the high pressure difference. The spacing is typically a few millimeters and the loss is in new turbines less than 0.5 % [41]. However, the sealing is worn after time and especially by high sand and sediment content in the water. This causes increase in leaking and efficiency loss. Leakage flow and horse shoe vortices are also introduced by the flow passing between the guide vanes and hub/ring.

- **Draft tube surge**

As the runner vanes are at a fixed angle, in contradiction to a Kaplan turbine where the runner blades can be adjusted, the flow exits without swirl only at BEP. Many turbines are operated outside the BEP, either at part load P<BEP or at over load P>BEP where swirl is introduced to the outlet flow of the turbine. With a high swirl component and low pressure in the draft tube, a water vapor rope can appear in the draft tube. This vapor rope is highly dynamic and can introduce vibrations as well as loss in efficiency.

- **Cavitation**

  Cavitation is a phenomena occurring when the local pressure decreases below water vapor pressure and causes boiling of the water. This happens even at temperatures close to freezing when the pressure is very low. Low local pressure is often due to high velocity or not sufficient submerging of the turbine. When the water vapor bubbles implode where the pressure again rises, they cause damage to the structure if this happens near the surface. A small synthetic jet is generated by the implosion which is strong enough to flush away a part of the steel structure. Cavitation can be amplified by the presence of secondary flow fields.

### 2.2.1 Foil theory

Some definitions used in foil theory can be seen in Figure 4. Camber line is the line exactly between top and bottom plane of the foil. The chord line is the straight line from leading edge to trailing edge. Symmetric foils as in Figure 4 have coinciding center line and camber line at the same place.

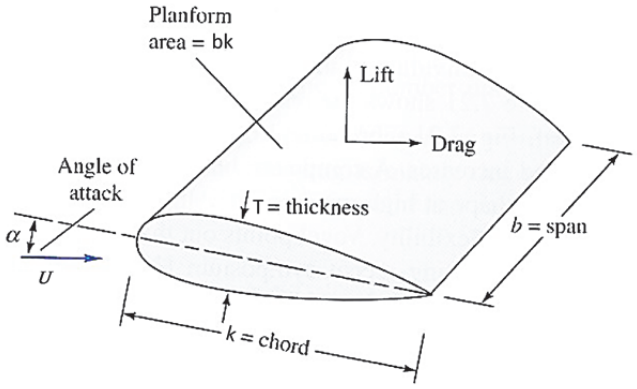


**Figure 4 – Foil property data [42]**

The none dimensional lift coefficient is defined as [42]:

$$C_L = \frac{F_L}{\frac{1}{2}\rho \cdot U^2 \cdot A} \tag{2.1}$$

and the none dimensional drag coefficient is defined as [42]:

$$C_D = \frac{F_D}{\frac{1}{2}\rho \cdot U^2 \cdot A} \tag{2.2}$$

Note that $F_D$ consists of a friction term $F_f$ which is the wall shear and a pressure term $F_p$ which is the force component in the flow direction from integrating the pressure load around the body. It is common to give or calculate the total drag force or drag coefficient which simply is the sum of the friction part and the pressure part. [43]

Lift-to-drag ratio also denoted foil efficiency is defined as lift force divided by drag force:

$$\eta_f = \frac{L}{D} \tag{2.3}$$

The lift-to-drag ratio factor is important in in aviation industry in order to obtain minimum fuel consumption. See chapter 8.7 in [42] for detailed foil theory.

### 2.2.2 Boundary layer

Viscous flows as studied here have a no slip condition at surfaces. This means that the velocity is zero at the surface. The layer where the velocity grows from zero velocity up to 99 % of the free stream velocity is called the boundary layer. Displacement thickness is the height the streamlines of the potential field have to move in order to conserve mass when flowing past a body with boundary layer flow. The displacement thickness at a given position of a foil can be found using Xfoil. By knowing the displacement thickness δ* the thickness of the boundary layer can be estimated from the following equation [42]:

$$\delta \approx 8\delta^* \tag{2.4}$$

### 2.2.3 Flow control

The term “flow control” is a wide term and covers all manipulation done in a flow to enhance the flow performance e.g. by avoiding unwanted phenomena present in the flow. Typical enhancements achieved by flow control can be increased efficiency by reducing flow losses or in/de-creasing heat transfer, reduced vibration and noise, increased operation range etc. Flow control can be applied passive and active.

Passive flow control cannot be adjusted during operation. Fins to guide the flow through an elbow or vortex generators mounted on airfoils to delay flow separation and stall at high AoAs are examples of passive flow control.

Active flow control can be adjusted during operation. Unwanted flow effects are often present only at parts of the operational range. Active flow control is then able to enhance the flow at the problematic operational range, but can be deactivated partly or fully to not cause negative effects in other operational ranges. Examples are flaps and slats on airfoils to increase lift at low speeds, but do not disturb at cruising speed. Water injection contra rotary in the draft tube of a Francis turbine to reduce pressure pulsation at part load is another example.

In order to apply flow control one need to know the details of the problematic flow patterns and when they occur to determine if passive or active (if possible) flow control is most suitable for the given application.

#### *2.2.3.1 Vortex generator*

Vortex generators are a type of passive flow control device. They are used in a variety of applications to improve flow performance. Especially the aviation industry utilizes the benefit from vortex generators. By mounting vortex generators on the wings and on the engine nacelle, small vortices are introduced in the boundary layer. The benefit is that the flow stay attached to the surface for a wider range of velocities and angels of attack. This means the wing reaches stall (flow separation) at a higher AoA and increases the operational range of a wing which is important under take-off and landing. The vortex generators induce drag locally, but can increase overall performance of the foil so total drag is reduced.

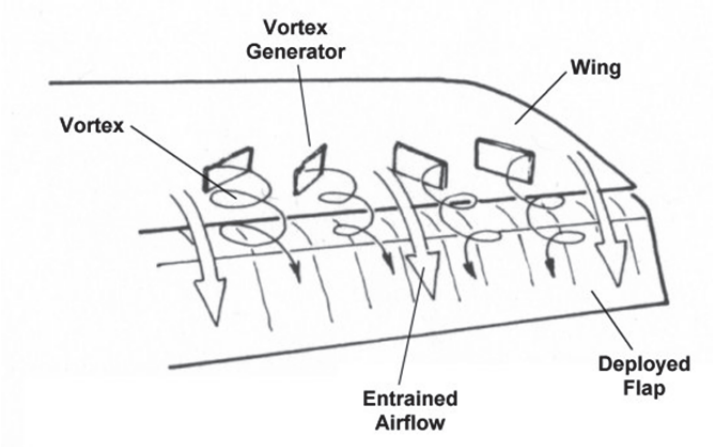


**Figure 5 – Example of wing mounted vortex generators [44]**

In this work the purpose of the vortex generators are to mix the wake which consist of both high and low momentum structures. The goal is to mix the wake so it is more consistent with less velocity fluctuations. The vortex generators come in different shapes and sizes, such as small angular fins, v-shaped fins or triangles. In this work v-shaped vortex generators of 1mm height are used. The VG height should be just higher than the boundary layer thickness estimated in Xfoil, chapter 2.2.2.

**Figure 6 – Vortex generators V1**

### 2.2.4 Wake theory

All solid bodies placed in a fluid where either the body or the fluid moves, will create a wake in the fluid. A wake is the disturbed flow behind the body. The size and behavior is highly dependent on the Reynolds number. A wake often propagates in a V-shape behind the body and can consist of both regular and irregular patterns. The wake width increases downstream the body. The average velocity in the wake decreases compared to the free stream and this velocity deficit is defined in Equation 2.5 , and is shown in Figure 8:

$$\Delta u = U - u(y) \tag{2.5}$$

Wakes can be both laminar and turbulent. In this work the focus is on turbulent wakes and the dynamic behavior of the wake. See Figure 7 for a sketch of cylinder wake dependency of Reynolds number.

The wake behind the body causes drag, which is a loss of energy. A wide wake with heavy velocity deficit implies large drag while a narrow wake with small velocity deficit implies low drag from the body. A wake can also cause trouble if something is passing through it. E.g. an airplane passing a wake behind a mountain range or close behind another airplane. In this work wakes from hydrofoils and blades passing through this wake are investigated.

Examples of bodies generating different type of wakes when moving through their respective media are: a ball, a spinning ball, the hull of a ship, tip vortices from airplanes, wind blowing over and around a mountain, wind blowing around a power line, vehicles among many others. There are numerous different types of wakes. In this work the focus is on wakes that are related to the guide vanes in Francis hydro turbines. Wakes of the following objects are investigated:

- **Cylinder (D=12.7 mm)**
- **Hydrofoil (NACA 0015, k=81 mm)**

The wakes are investigated in a water tunnel where the where the free stream turbulence is low and the approaching flow field is highly uniform. The hydrofoils are of course the most relevant object to study as the guide vanes have a foil shape, but also the cylinder is of interest as the wake pattern is well documented and can work as a reference case for the hydrofoil study.

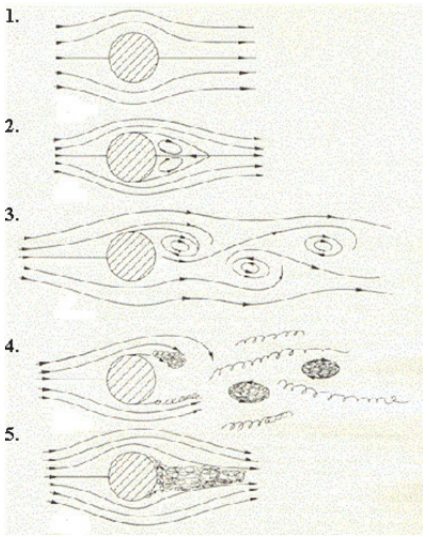


**Figure 7 – Wake behind a cylinder at various Re. 1-3. Re<1000, 4. Re=10000, 5. Re=100000 [45]**

Figure 7 shows cylinder wake at different Reynolds number.

- **1.** Laminar flow with stagnation points both at front and rear part of the cylinder. Only skin friction forces apply. No pressure difference.
- **2.** A small circulation wake forms behind the cylinder. The flow is still laminar and friction forces dominate the drag force.
- **3.** Reynolds number increase close to turbulent (Re≈2000) and defined vortices sheds of the cylinder.
- **4.** Re≈10000. The wake is now in the turbulent regime and does not slow down behind the cylinder to even out the pressure. Now the cylinder experience dominance of pressure drag. Shedding of turbulent vortices is present. The flow separates early from the cylinder.
- **5.** Re>100000. A turbulent boundary layer occurs and the stream lines separate at a later point and follow the edge of the boundary layer. The wake reduces, and the drag force decrease.

The wakes investigated in this work are cylinder wakes and hydrofoil wakes placed in a water tunnel as shown in Figure 8. The wake can be divided into different regions. [46] Close to the object is the near field where the shape of the object plays an important role of the wake flow. Downstream is the transition field where most of the momentum between the free stream and the

wake takes place. In the far field both the maximum velocity deficit Δu and the width $b_{wake}$ will increase with x-downstream. [47]

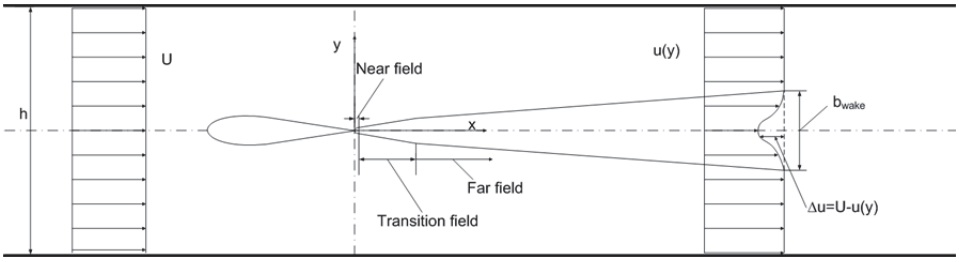


**Figure 8 – Wake properties [47]**

#### *2.2.4.1 Wake profiles*

To compare wake profiles at different x-positions or from different size hydrofoils, the wakes must be normalized. The wakes can be normalized by the maximum velocity deficit Δu and the width $b_{wake}$ as follows:

$$u_{norm} = \frac{U-u}{U}\sqrt{\frac{x}{k}} \tag{2.6}$$

$$y_{norm} = \frac{y}{\sqrt{x \cdot k}} \tag{2.7}$$

It is desirable to describe the different wakes by parameters when comparing different wakes. The wakes are curve fitted to a standard wake profile as follows:

$$U_{wake} = a_0 + a_1 \cdot e^{-a_2(y_{norm}-a_3)^2} \tag{2.8}$$

where $a_0$, $a_1$, $a_2$, $a_3$ are found by curve fitting the measured profile to a standard wake profile. Investigation of standard wake profiles is not a part of this work, but is an important role in steady wake analysis. This work focus mostly on the dynamic behavior of wakes. See Bjarte Grytli Seim's master thesis [47] for a study of wake profiles used in this work.

#### *2.2.4.2 von Karman vortex street*

The von Karman vortex street is the occurrence of alternating vortex shedding coming from unsteady flow separation off a bluff body in a fluid stream. von

Karman shedding is Reynolds number dependent, and for cylinders, continuous alternating vortices are shed from top and bottom of the cylinder in the range $90<Re<10^7$ [43].

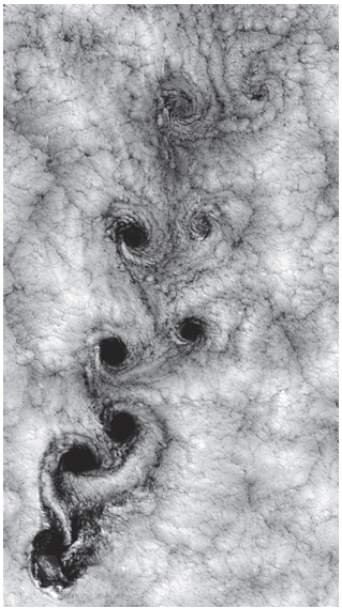

**Figure 9 – von Karman vortex street in clouds near the Juan Fernandez islands [48]**

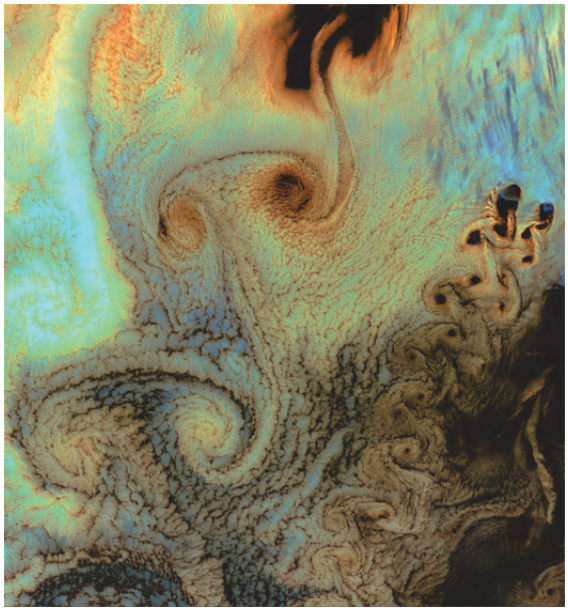

**Figure 10 – von Karman vortex street caused by wind hitting land at Aleuitan islands in Alaska [49]**

von Karman vortices are dominating the dynamics in blunt body wakes, but are also present in slender body wakes such as a hydrofoil. Here the frequencies are much higher. A typically von Karman shedding frequency in a Francis turbine can be in the range hundred to some thousands Hz. von Karman vortices are known to cause fatigue problems on the stay vanes in Kaplan turbines and be the source of severe noise from shedding off trailing edges of stay vanes, guide vanes or runner vanes. [15, 50]

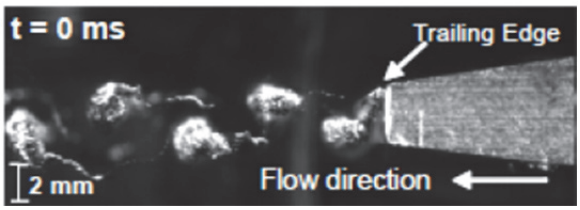


**Figure 11 – Cavitating von Karman vortices shed off a blunt hydrofoil [12]**

### 2.2.4.3 *Strouhal number*

von Karman shedding is highly related to the Strouhal number which is a non-dimensional number describing the shedding frequency and is given as:

$$St = \frac{fL}{U} \tag{2.9}$$

f is the shedding frequency, L the characteristic length (for a cylinder L=D) and U is the free stream velocity.

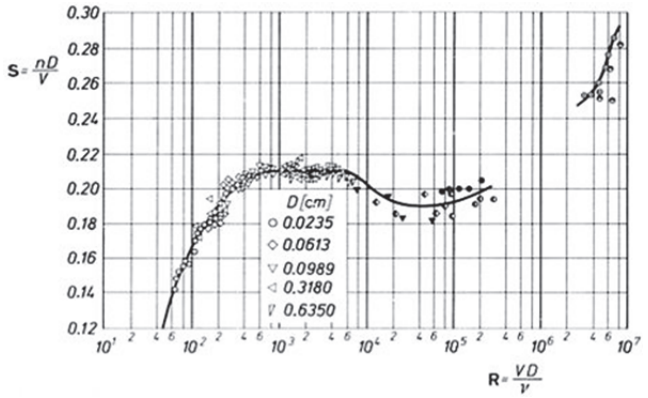


**Figure 12 – Strouhal number dependency on Reynolds number for cylinder [51]**

### 2.2.4.4 *Velocity distribution in the vaneless space*

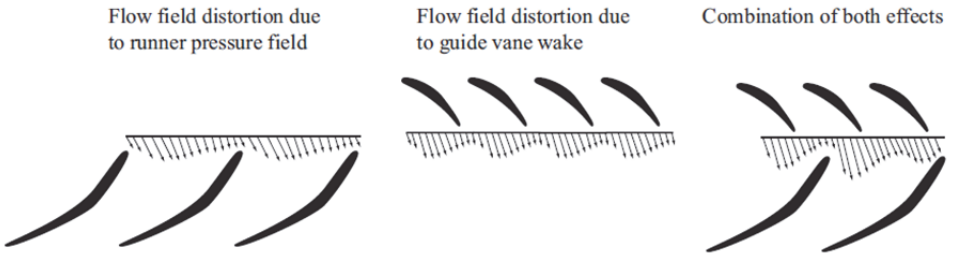


**Figure 13 – Velocity distribution in the vaneless space [52]**

The velocity distribution in the vaneless space is affected by two phenomena:

1. The velocity/pressure distribution due to the movement of the runner (rotor) cascade. Each blade has a pressure/suction side.
2. The velocity/pressure distribution from the guide vane (stator) wake after passing through the guide vane cascade.

The vaneless space experiences both effects which can be seen in Figure 13. The velocity distribution is inverse related to the pressure, so low velocity means high pressure. Note that this consideration is for averaged flow conditions not taking dynamics into consideration. In reality the flow field is affected by unsteady wake dynamics which can both amplify and/or attenuate the indicated flow pattern.

### 2.2.5 Draft tube flow

Because of the tangential velocity component ($cu_2 \neq 0$) outside BEP as mentioned in section 2.1, swirl occurs at the outlet of the turbine. If the pressure inside the swirl is lower than the boiling point for water at the given temperature, water evaporates and makes a helical vortex rope visible. The vortex rope will rotate with a frequency $f_R$ given as:

$$\frac{f_n}{3.6} \leq f_R \leq \frac{f_n}{3} \tag{2.10}$$

which is called the Rheingans frequency [2]. Turbine geometry decides the behavior of the draft tube vortex rope. The part load rope rotates equal to the runner direction, while the overload rope rotates contrary to the runner direction. The part load vortex rope rotates and can cause damage if it hits the turbine structure. The over load vortex rope usually pulsate and can lead to heavy mass oscillations. The mass oscillation can propagate through the turbine and create fluctuation in the water way.

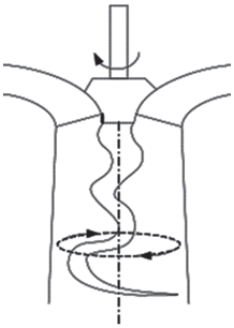

**Figure 14 – Sketch of vortex rope in the draft tube [53]**

**Figure 15 – Part load vortex rope [54]**

**Figure 16 – Over load vortex rope [54]**

Several attempts have been made to deal with the part load pressure pulsation problem. e.g. mounting of fins in the draft tube [55], extension of the runner

shaft by extending the shaft into the draft tube also referred to as “stulk” [8], air injection and water injection into the draft tube [53, 56, 57].

The rotation at the outlet due to off-design operation leads to unfavorable effects in terms of pressure fluctuation in the draft tube. The pressure pulsations can cause extra load on the turbine blades and on the draft tube structure which over time may lead to cracking or fatigue. The draft tube surge pulsations have relatively low frequency, but can experience high amplitudes. The dynamics of the pressure fluctuations can also coincide with other eigenfrequencies in the system, e.g. water hammer frequency and cause severe damage to the power plant. The pressure fluctuations can also affect the power output and propagate to the grid [58].

## 2.3 Statistics

Statistic is a helpful tool when analyzing a large quantum of data. The most important statistical methods used in this work are briefly described below.

### 2.3.1 Mean

The average value of a data series is also referred to as mean and is for discrete data defined as:

$$\overline{X} = \frac{1}{N}\sum_{i=1}^{i=N} x_i \tag{2.11}$$

### 2.3.2 Standard deviation

Standard deviation tells if the data fluctuate much or little around the mean value and is for a discrete data series defined as:

$$\sigma = \sqrt{\frac{1}{N}\sum_{i=1}^{N}(x_i - \overline{X})^2} \tag{2.12}$$

### 2.3.3 Peak to peak (p2p)

The peak to peak value is the largest difference between maximum and minimum value of a signal and is defined as:

$$\psi = \max(f(x)) + \min(f(x)) \tag{2.13}$$

## 2.4 Frequency analysis

Frequency analysis is a convenient way to determine the frequencies that are present in a time resolved signal, and at which amplitude they appear. This is done by transforming the time signal into the frequency domain through a Fast Fourier Transform – FFT. The signal will then be described by superimposing harmonic functions such as sine/cosine functions. Both Matlab and LabView which are used in this work have built in FFT-algorithms as follows:

$$Y = \sum_{n=0}^{N-1} x_n e^{-2\pi \cdot j \cdot k \cdot n/N} \text{ [59]} \tag{2.14}$$

### 2.4.1 Spectral leakage

As the data is discrete the frequency resolution is finite and defined as:

$$\Delta f = \frac{f_s}{n_s} = \frac{1}{t_s} \text{ [59]} \tag{2.15}$$

When the frequency resolution is coarse, the frequency analysis might not hit spot on the actual frequency present in the signal. This will cause the energy at a given frequency to spread out on the neighboring frequencies, thus the amplitude decrease. The effect can be seen in Figure 17.

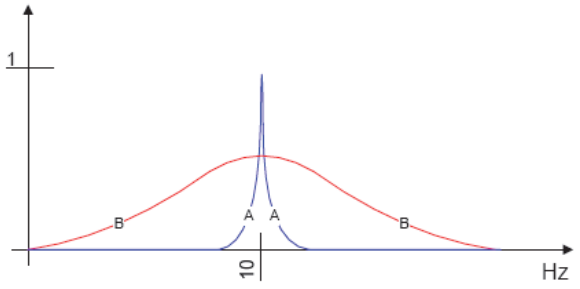


**Figure 17 – Spectral leakage [60]**

Blue signal has a frequency that coincides with Δf while the red signal has a frequency that falls between the discrete values of Δf. To ensure high frequency resolution long enough sampling time has to be chosen.

## 2.5 Integral time scale

The integral time scale describes the time between uncorrelated values in a signal, and is calculated from the autocorrelation function [61]:

$$\Lambda = \int_0^\infty R_{ii}(r,t)dt \tag{2.16}$$

where $R_{ii}$ is the autocorrelation function.

$$R_{ii}(t) = \frac{\langle u_i(x_i,t)u_i(x_i,t+\Delta t)\rangle}{\langle u_i^2\rangle} \tag{2.17}$$

Since the POD requires independent samples, only data separated by 2 times the integral time, $\Lambda$ will contribute to the statistics of the POD-function. More periods separated by 2 times the integral time scale helps the POD to reveal all dynamics present in the signal. Therefore an integral time scale computation is performed prior to the POD analysis. By removing many of the temporal highly resolved data points the POD computation time can be reduced drastically. It also plays an important role in choosing reasonable time blocks for averaging data used in the POD in chapter 2.7.4.1.

## 2.6 Integral length scale

The integral length scale tells over how large distances in space structures in a signal are correlated. It can be found by multiplying the integral time scale by the local mean velocity.

$$\ell = \Lambda \cdot u \tag{2.18}$$

[61] suggests that the investigated field should be at least 6 times the integral length scale in order to calculate the integral length scale.

## 2.7 Proportional Orthogonal Decomposition - POD

### 2.7.1 Introduction

POD was first introduced in 1967 by Lumley [28] to decompose the flow field of a turbulent flow to identify and study the dynamics of the large scale structures. POD is a statistical method that can be applied to a random signal, particular in the inhomogeneous directions. The goal is to describe a random field by a set of deterministic functions sorted according to their contribution to the total flow energy. In this work we want to see what structures are present in the turbulent flow- or pressure field, and if some flow structures represent a significant part of the total energy in the field.

Turbulent flows are described as stochastic, which means quantities can only be described in terms of statistics. The deterministic functions are projected onto the stochastic field and maximized to find the function that best describes the stochastic field. The maximization results in an integral value problem (Fredholm integral equation of the second kind), where the kernel is the two-point cross correlation tensor of the stochastic velocity field. [62] This technique decomposes the turbulent velocity field into eigenvalues and corresponding eigenfunctions which represent the degree of total finite kinetic energy associated with each flow structure of the flow. The eigenvalues are sorted in descending order with its corresponding eigenfunction, where the largest eigenvalue represent the flow structure with the most energy. The orthogonal eigenfunctions describe the motion of the flow structure and can be used to reconstruct the original velocity data similar to Fourier transform reconstruction together with the eigenvalue. [38]

POD can be applied as the “classical POD” where the number of grid points and number of velocity components determine the number of POD modes. This is method is preferred when having low spatial resolution and is used in the draft tube study presented in this thesis.

The “snapshot POD” was developed in 1987 by Sirovich and Kirby and is more suitable for high spatial resolved data measured simultaneously such as PIV data. The number of POD modes are then determined by the number of snapshots. The snapshot POD is applied on the wake data presented in this

thesis. Differences and application of both classical and snapshot POD is presented in [63, 64].

### 2.7.2 POD theory

The theory behind POD is complex, and is thoroughly described in various publications, as by Lumley [28], Lu [38], Hilberg [65], Sirovich [35] and Wanström [66]. The theory described in this chapter is based on chapter 6 of Tutkun [62].

POD is applicable only in fields which are statistically inhomogeneous and of finite total energy. Decomposition of the field is done by maximizing the projection of a deterministic field $\phi_i(\cdot)$ onto the stochastic velocity field $u_i(\cdot)$. Maximization of the deterministic field is performed by calculating the largest inner product of the following expression:

$$\left\langle \left| \alpha^2 \right| \right\rangle = \left\langle \left| (u_i(\cdot), \phi_i^*(\cdot)) \right|^2 \right\rangle \tag{2.19}$$

$\langle\ \rangle$ denotes the ensemble average and $\cdot$ denotes any time or spatial dependence of the field of interest. The inner product results in $\alpha$ can be written as:

$$\alpha = (u_i(\cdot), \phi_i^*(\cdot)) = \int_{Dm} u_i(\cdot)\phi_i^*(\cdot)d(\cdot) \tag{2.20}$$

Integration is performed over the domain D of interest. Normalized projection of the mean square can be obtained by dividing eq. (2.20) by the magnitude of the deterministic field.

$$\lambda = \frac{\left[\int_D u_i(\cdot)\phi_i^*(\cdot)d(\cdot)\right]\left[\int_D u_i(\cdot)\phi_i^*(\cdot)d(\cdot)\right]^*}{\left[\int_D \phi_l(\cdot)\phi_l^*(\cdot)d(\cdot)\right]\left[\int_D \phi_l(\cdot)\phi_l^*(\cdot)d(\cdot)\right]^*} \tag{2.21}$$

Maximizing the normalized mean square results in a Fredholm equation of the second kind:

$$\int_D R_{i,j}(\cdot,\cdot')\phi_j(\cdot') = \lambda\phi_i(\cdot) \tag{2.22}$$

The kernel of eq. (2.22), $R_{i,j}(\cdot,\cdot')$ is the two point cross correlation tensor which is defined as:

$$R_{i,j}(\cdot,\cdot') = \left\langle u_i(\cdot) u_j(\cdot') \right\rangle \tag{2.23}$$

‘ denotes different time or position. i and j represent appropriate velocity components.

If the field of interest is bounded and of finite total turbulent kinetic energy the Hilbert-Schmidt theory applies. Eq. (2.22) produces denumerable solutions $\phi(\cdot)s$ , and not a single solution if the domain is of finite energy. For each of the solutions there is pair of eigenvalue, $\lambda$ , and eigenfunction, $\phi(\cdot)$ . This gives:

$$\int_D R_{i,j}(\cdot,\cdot')\phi_j^{(n)}(\cdot')d(\cdot') = \lambda^{(n)}\phi_i^{(n)}(\cdot) \tag{2.24}$$

n=1,2,3,… denotes the solution index, also called POD mode number. Properties of the solutions to the POD integral, eq. (2.24), for fields of finite total energy can be listed as follows:

Solutions to the POD integral are orthogonal:

$$\int_D \phi_i^{(n)}(\cdot')\phi_i^{(m)}(\cdot')d(\cdot) = \delta_{nm} \tag{2.25}$$

All eigenfunctions are coupled in pairs with a corresponding eigenvalue. The eigenvalues are ordered in descending order, so $\lambda^{(1)} > \lambda^{(2)} > \lambda^{(3)} > \ldots$
Eigenvalues are real and positive. The stochastic field can be reconstructed using the eigenfunctions:

$$u_i(\cdot) = \sum_n a_n \phi_i^n(\cdot) \tag{2.26}$$

$a_n$ is the set of random coefficients obtained by back projecting the eigenfunction onto the turbulent stochastic field:

$$a_n = \int_D u_i(\cdot)\phi_i^{*(n)}(\cdot)d(\cdot) \tag{2.27}$$

The random coefficients from eq. (2.27) are uncorrelated since the eigenfunctions are orthogonal:

$$\lambda^{(n)} = \left\langle a_n a_m^* \right\rangle \delta_{nm} \tag{2.28}$$

The two point cross correlation tensor, $R_{i,j}(\cdot,\cdot')$ can also be reconstructed using the reconstructed velocities given by eq. (2.26):

$$R_{i,j}(\cdot,\cdot') = \sum_n \lambda^{(n)} \phi_i^{(n)}(\cdot) \phi_j^{(n)}(\cdot') \tag{2.29}$$

Contraction of the reconstructed two-point cross-correlation tensor shows that the total energy within the finite domain equals the summation of the eigenvalues:

$$E = \int_D \langle u_i(\cdot) u_i(\cdot) \rangle d(\cdot) = \sum_n \lambda^{(n)} \tag{2.30}$$

This shows that the POD decompose the energy in the turbulent field through the eigenfunctions, where the eigenvalue is directly associated with the energy content of the respective eigenfunction. The largest eigenvalue represent the structure with the most energy. The eigenvalue is directly associated with energy when dealing with velocity. This is true when applying POD on velocity a field. When applying the POD on a pressure signal, the eigenvalue are not directly related to the energy, but to the pressure variance $p^2$. The pressure variance is a measure of the pressure field fluctuations.

### 2.7.3 Axisymmetric assumption

Draft tube flow as presented in this study is assumed to be and treated homogeneous in the azimuthal direction, periodic and axisymmetric. Axisymmetry means that the mean pressure in a given radial position is equal, independent of the angular measuring position. At BEP the flow has no or very little swirl, and the axisymmetric assumption is well fulfilled. At partial discharge the flow develops from a steady axisymmetric flow field as it leaves the runner, to a 3D unsteady flow field with possible formation of a helical vortex rope and associated pressure pulsations. This flow field is not fully axisymmetric, but previous studies [67, 68] have proved that the axisymmetric assumption for numerical simulations serve as a fair assumption and give results in good agreement with experiments.

The axisymmetric assumption is made due to two important reasons:

1. POD on an axisymmetric homogeneous and periodic flow reduces to Fourier series expansion in the homogeneous (this case azimuthal direction). This simplifies the analysis and measurements drastically. To apply POD without an axisymmetric assumption a 2D POD similar to the one used in the wake study must be applied which require a high temporal resolution.

2. Optical windows required for high resolved PIV measurements were not present, and could neither be installed at the power plant. Manual probes seemed to be the only reasonable solution in terms of time and modification requirements at the power plant. Space limitations only allowed measuring 180 degrees of the draft tube.

### 2.7.4 POD on an axisymmetric flow field

The chapter about POD in an axisymmetric flow is based on the axisymmetric theory part in [34].

The POD seeks a deterministic field which has the maximum mean square projection onto the original random pressure field [29]. The maximization of the normalized mean square projection λ results in a Fredholm integral of the second kind, where the symmetric kernel is the two-point cross-correlation tensor, which for the axisymmetric flow can be written as follows:

$$\tilde{R}_{i,j}(x,x';r,r';\theta,\theta';t,t') = \left\langle \widetilde{p_i}(x,r,\theta,t)\widetilde{p_j}(x',r',\theta',t') \right\rangle \qquad (2.31)$$

' denotes different positions for x, r and θ and a different time for t. Ensemble averaging is represented by $\langle\ \rangle$. The subscripts i and j denote appropriate components. When dealing with velocity they refer to the stream wise velocity component $u_x$, the radial velocity component $u_r$ and the azimuthal velocity component $u_\theta$. Analysis presented in this work is performed on pressure, $p$, which is a scalar and gives $\widetilde{p}_i = \widetilde{p}_j = p$.

Because the flow is stationary in time and statistically homogenous in the azimuthal direction, the two point cross-correlation tensor is a function of only the separations in these directions. If $\tau = t - t'$ and $\Delta\theta = \theta' - \theta$ represent the separations in time and in the azimuthal direction the two point cross-correlation becomes

$$\tilde{R}(x,x';r,r';\theta,\theta';t,t') = R(x,x';r,r';\Delta\theta;\tau) \qquad (2.32)$$

In the stationary and homogenous direction the POD reduces to Fourier expansions [28, 31, 33]. If the flow is homogenous in space or periodic as in the azimuthal direction, the decomposition also becomes a Fourier series

expansion. The two-point cross-correlation is first Fourier transformed in time, then in the azimuthal direction, before the proper orthogonal decomposition is performed on the Fourier coefficients. The cross-spectral tensor is given by:

$$S(x,x';r,r';m;f)=\frac{1}{2\pi}\int_{-\infty}^{\infty}\sum_{0}^{2\pi}R(x,x';r,r';\Delta\theta;\tau)e^{-i(2\pi f\tau+im\Delta\theta)}d\tau\Delta\theta \qquad (2.33)$$

f is the frequency corresponding to $\tau$ and m is the azimuthal Fourier mode number corresponding to $\Delta\theta$. When only one downstream position is considered, x in (2.33) is treated as a parameter which reduces the POD equation to slice POD. [31] The field can be considered frozen in time as it convects by the probes for low turbulence intensity in the three dimensional wake [27]. Thus the stream wise dependent variable x is equal to time and the integral equation reduces to

$$\int_{r'}S(r,r';m;f)\phi_i^{*(n)}(r';m;f)r'dr'=\lambda^{(n)}(m;f)\phi_i^{(n)}(r;m;f) \qquad (2.34)$$

where $\lambda^{(n)}(m;f)$ and $\phi_i^{(n)}(r;m;f)$ represent the eigenspectra and the eigenfunction respectively. Since the domain is bounded in the inhomogeneous direction, the Hilbert-Schmidt theory applies.

Standard numerical schemes can be used to solve this eigenvalue problem, eq. (2.34), if the kernel is Hermitian symmetric. The r' on the left hand side in eq. (2.34) creates an asymmetry in the kernel. By multiplying both sides by $r^{\frac{1}{2}}$ and dividing r' into $r'^{\frac{1}{2}}\times r'^{\frac{1}{2}}$ the matrix can be made symmetrical. Eq. (2.34) is the rewritten as:

$$\int_{r'}\underbrace{r^{\frac{1}{2}}S(r,r';m;f)r'^{\frac{1}{2}}}_{W(r,r';m;f)}\phi^{*(n)}\underbrace{(r';m;f)r'^{\frac{1}{2}}}_{\hat{\phi}^{*(n)}(r';m;f)}dr'=\underbrace{\lambda^{(n)}(m;f)}_{\hat{\lambda}^{(n)}(m;f)}\underbrace{r^{\frac{1}{2}}\phi^{(n)}(r;m;f)}_{\hat{\phi}^{*(n)}(r;m;f)} \qquad (2.35)$$

The POD integral equation with a Hermitian symmetric kernel can then be written as:

$$\int_{r'}W(r,r';m;f)\hat{\phi}^{*(n)}(r';m;f)=\hat{\lambda}^{(n)}(m;f)\hat{\phi}^{*(n)}(r;m;f) \qquad (2.36)$$

The number of grid points multiplied with the number of velocity components included in the two-point cross-correlation tensor determine the number of POD eigenfunctions, eq. (2.36) [69].

#### *2.7.4.1 Numerical implementation*

The steps to construct the POD equation, eq. (2.36), can be summarized as follows [34, 70]:

1) Instantaneous pressure is measured simultaneously at two points.
2) The pressure signal is Fourier transformed in time for the finite size record length:

$$\hat{p} = (r, \theta, f) = \int_{-T/2}^{T/2} e^{-i2\pi ft} p(r, \theta, f) dt \tag{2.37}$$

where $\hat{p}(r, \theta, f)$ are the Fourier coefficients and T represents the record length for each block of data.

3) Steps 1 and 2 are repeated for all pair of points
4) The cross-spectra are computed and block averaging is performed as follows:

$$S(r, r'; \Delta\theta; f) = \frac{\left\langle \hat{p}(r, \theta, f) \hat{p}^{*} (r', \theta + \Delta\theta, f) \right\rangle}{T} \tag{2.38}$$

$\langle \ \rangle$ and * denote the block averaging and complex conjugate respectively.

5) The next step is to compute the doubly transformed cross-spectra by numerical approximation to the Fourier series expansion of eq. (2.38) in the azimuthal direction:

$$S(r, r'; m; f) = \frac{1}{2\pi} \sum_{m=0}^{N} \tilde{S}(r, r'; \Delta\theta; f) e^{-im\Delta\theta} d(\Delta\theta) \tag{2.39}$$

N is twice the number of angular separation $\Delta\theta$ in the azimuthal direction. Measurements are performed in half of the measurement plane only as the following symmetry conditions apply [34]:

$$\tilde{S}(r, r'; \Delta\theta; f) = \tilde{S}^{*} (r, r'; -\Delta\theta; f) \tag{2.40}$$

6) The eigenvalue problem, eq. (2.36), is solved for each frequency and azimuthal Fourier mode after construction of the Hermitian symmetric kernel.

#### *2.7.4.2 Choosing block length and number of blocks*

In order to obtain good quality POD results it is important to first calculate the integral time scale of the signal. It is basically the autocorrelation function integrated over the radial domain described in chapter 2.5. The integral time scale is a measure of correlation time. It is desired to capture many blocks separated by 2 times the integral time scale when computing the POD. These blocks are uncorrelated. By choosing too short block length the POD is not able to capture the dominant dynamics in the signal, and it results in poor frequency resolution. The whole record length is divided into blocks, and the data is averaged over all blocks. Many blocks ensure a good statistical base for the POD, and reduces the uncertainty. It is therefore important to find the appropriate ratio between block length and number of blocks from the data series to be analyzed.

#### *2.7.4.3 Interpretation of POD-modes*

In an axisymmetric flow as in the draft tube flow presented in this work, the POD modes describe the motion in radial direction. The number of modes are given by the number of radial measurements. In the draft tube study 6 POD modes are obtained. The resulting eigenvalues represent the POD modes. Negative or complex eigenvalues can occur because of inaccurate positioning while measuring and from poor data in terms of short data series or few data blocks. The POD does not give the direction of the motion, but it addresses the amount of energy, in terms of pressure variance, to the given motion behavior. The pressure addressed to POD mode 1 will experience the same change in value over the radius, but the POD does not tell if it increase or decrease along the radius. Higher POD modes follow the same structure as presented in Figure 18, by adding another sine wave per increased POD mode. The actual signal experience a change in radial direction represented by the sum of all POD modes.

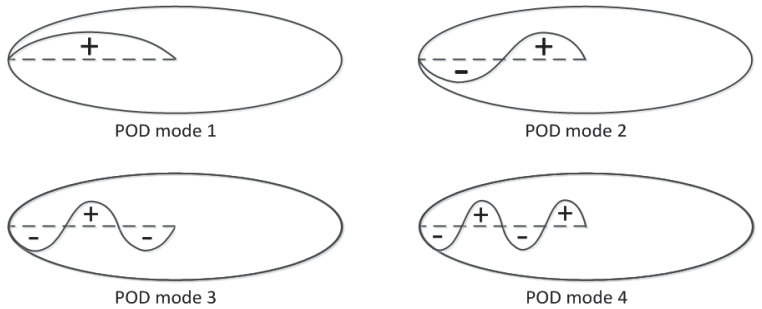


**Figure 18 – Motion of the 4 first POD modes**

#### *2.7.4.4 Interpretation of azimuthal modes*

The number of azimuthal modes are given by the number angular measurements. In this study 7 angular positions are measured from 0-180 degrees. Since symmetry conditions apply this result in 2x7-2=12 (numbered 0-11) azimuthal modes. Measurements performed at 0 and 180 degrees does not take part in the symmetry, therefore 12, and not 14 azimuthal modes are obtained. The azimuthal modes describe the pressure motion in the measured plane. Mode 0 and mode 6 are independent while mode 1-5 are in pairs and are identical to and correspond to mode 11-7 respectively because of the symmetry conditions. A sketch of interpretation of the azimuthal modes is given in Figure 19. All motions are in plane motions, and + and – implies opposite direction. Later azimuthal modes follow the same pattern by adding one more +- motion per increased mode. The total fluctuation is described by the sum of all the azimuthal modes.

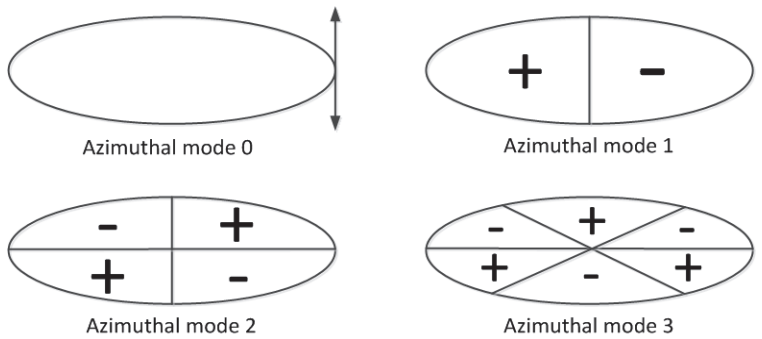


**Figure 19 – Motion of the 4 first azimuthal modes**

# 3 PIV measurements at the UMN-SAFL water tunnel

The laboratory tests at the high-speed water tunnel at Saint Anthony Falls Laboratory (SAFL), see Figure 20, were performed by Bjarte Grytli Seim as a part of his master's thesis in April 2009. The tests consist of Particle Image Velocimetry – PIV performed on the near wake of a cylinder, with diameter D=12.7 mm, and a NACA0015 hydrofoil, with chord length k=81 mm. The hydrofoil wake was recorded of a plain hydrofoil and of a hydrofoil with mounted vortex generators, VGs. Four different VG-set-ups were measured, while only one VG-set-up is used in this work. The VG set-up used in this study is what Seim describes as VG case 2 which showed most promising results in Seim's study. [47] For total review of the experimental measurements and steady wake analysis on all wake set-ups, see Seim's master thesis [47].

## 3.1 The water tunnel

The tunnel was originally built as a free surface test facility but was later modified and is now mostly used for normal water tunnel operation. The test section has a length of 1.2 m, a height of 0.19 m and a width of 0.19 m. It is possible to look in to the test section from the bottom window and the two side windows. Both the velocity and the pressure in the tunnel can be regulated independently. The pressure in the tunnel can be adjusted from about 15 kPa to 200 kPa. The measured uniformity of the flow is better than 1 %, and the turbulence level is found to be approximately 0.3 % [71].

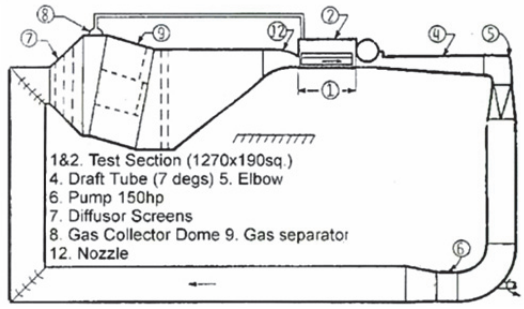


**Figure 20 - The Saint Anthony Falls Laboratory water tunnel [71]**

## 3.2 The PIV-measurement equipment

The PIV equipment that was used was composed of a Nd:YAG laser (Neodymium: Yttrium Aluminum Garnet), Photonics DM30-527. This laser can deliver pulses with energy content of 10 – 400 mJ/pulse. The seeding was hollow glass beads. For taking the photos a high speed camera of the type Fastcam APX-RS was used. This can take images at a frequency up to 10 000 Hz. When taking images at 10 000 Hz, the resolution of the image could be up to 512 by 512 pixels. Higher image resolution is possible at lower frame rates. The lens that was used for the high speed camera was a 105mm Nikon lens.

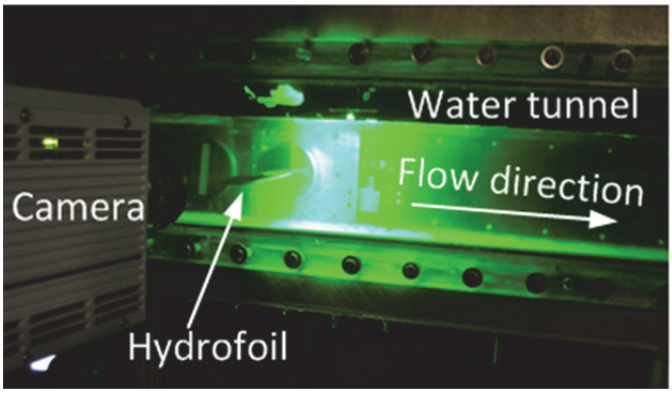


**Figure 21 - PIV measurement setup, with camera, water tunnel, cylinder and laser**

The pressure was measured 165 mm upstream the cylinder to calculate the water velocity in the test section. The pressure measurements were made with a LabView based acquisition program. All the PIV recordings were done with another PC with the DaVis7 software installed.

## 3.3 Cylinder wake

The PIV measurements were performed on a cylinder with D=12.7 mm, and test conditions and main parameters are shown in Table 1, where U refers to free stream velocity, f is sampling frequency and T is record time.

| Case | u1 | u2 | u3 | u4 | u5 | u6 |
|---|---|---|---|---|---|---|
| **U** | 1.34 | 2.01 | 2.84 | 3.95 | 4.95 | 5.94 |
| **$f_s$** | 1000 | 2000 | 4000 | 4000 | 5000 | 6500 |
| **$T_s$** | 4.0 | 2.0 | 1.0 | 1.0 | 0.80 | 0.62 |
| $\Delta t$ | 1000 | 500 | 250 | 250 | 200 | 153.85 |

**Table 1 – Free stream velocity U [m/s], frame rate f [Hz], logging time T [s] and $\Delta t$ [μs] for the cylinder cases**

## 3.4 Hydrofoil wake

The tests were performed on a hydrofoil, k=81 mm, for different angle of attacks (AoAs) at reference speed U=9 m/s. Tests are carried out on plain (denoted plain-AoA) hydrofoils and on hydrofoils where 1mm V-shaped vortex generators (denoted V1-AoA) are mounted on the suction side of the hydrofoil at x/k = 0.38 from the foil tip. The insert can be seen at the bottom of the hydrofoil in Figure 22. Note that the suction side is at the bottom of the foil in Figure 22 when the hydrofoil is pitched at positive AoAs as in this study.

**Figure 22 – Hydrofoil**

**Figure 23 – Vortex generators V1**

Both plain hydrofoil and hydrofoil with VG inserts are tested for AoA ranging from 0-10 degrees with 2 degrees increment. The sampling rate was 10 kHz and the record length was 0.1 s.

### 3.4.1 Boundary layer

The displacement thickness δ* can be calculated in Xfoil [72] for various AoAs, and can be used to calculate boundary layer thickness at the VG insert at x/k=0.38 for AoA=0 and AoA=6 from eq. (2.4).

| **AoA** [degrees] | **δ** [mm] |
|---|---|
| 0 | 0.9 |
| 6 | 1.1 |

**Table 2 – Boundary layer thickness**

This shows that the vortex generators of height 1mm are approximately the height of the boundary layer.

## 3.5 Main results and wake data analysis

Further details and the data analysis along with discussion and conclusions are presented in the two published papers.

Paper 1, "*Characterizing rotor-stator interaction using experimentally obtained wake flow fields, CDF and POD*" in chapter 4 presents the analysis and results from the cylinder wake data. The paper has been submitted to the Journal of Fluids Engineering and is being reviewed.

Paper 2, "*Characterizing rotor-stator Interaction – RSI in hydrofoil wake using CFD and experimentally obtained wake flow fields*" in chapter 5 presents the analysis and results from the hydrofoil wake data. The paper was presented at the International Symposium on Transport Phenomena and Dynamics of Rotating Machinery – ISROMAC 14 at Honolulu in February/March 2012.

The papers serve well as a standalone documentation of the performed study on wake dynamics and rotor-stator interaction. Chapter 7 discuss the major findings and why and how this can be useful information from the two wake papers. This section also link the wake study to the draft tube study presented as a monograph in chapter 6.

Some additional results for the cylinder study and hydrofoil study are presented in chapter 4.1 and 5.1 respectively.

# 4 Paper 1

## CHARACTERIZING ROTOR STATOR INTERACTION USING EXPERIMENTALLY OBTAINED WAKE FLOW FIELDS, CDF AND POD

**Is not included due to copyright**

# 5 Paper 2

## CHARACTERIZING ROTOR STATOR INTERACTION – RSI IN HYDROFOIL WAKE USING CFD AND EXPERIMENTALLY OBTAINED WAKE FLOW FIELDS

14th International Symposium on Transport Phenomena and Dynamics of Rotating Machinery, ISROMAC-14
February 27th - March 2nd, 2012, Honolulu, HI, USA

# CHARACTERIZING ROTOR STATOR INTERACTION - RSI IN HYDROFOIL WAKE USING CFD AND EXPERIMENTALLY OBTAINED WAKE FLOW FIELDS

**Pål Henrik Enger Finstad[1]*, Morten Kjeldsen[1], Roger Arndt[2]**

**[1]NTNU**
**Alfred Getz vei 4, 7491 Trondheim, Norway**
**pal.henrik.finstad@ntnu.no**

**[2]St. Anthony Falls Laboratory,**
**2 Third Avenue SE, Minneapolis, MN 55414, USA**
**arndt001@umn.edu**

## Abstract

Time Resolved PIV – Particle Image Velocimetry, (TRPIV), up to 10,000 frames per second, was used to map the wake flow fields downstream of a NACA 0015 hydrofoil spanning the test section (190 mm x 190 mm) of the water tunnel at the Saint Anthony Falls Laboratory at the University of Minnesota. The chord length of the hydrofoil is k=81 mm. The reference velocity is 9 m/s and the wakes were measured for various angles of attack. The time-average wake is characterized by the width, velocity deficit and a turbulence level. All will be functions of downstream position (x) as well as the traverse (y) position. The wakes will also, depending on test conditions, be characterized by the shedding of coherent vortex structures. The dynamics of this process can be characterized by an average vortex shedding frequency and a vortex strength. Regular spectrum- and POD analysis is made on the experimental data, and hence the CFD boundary condition, to reveal the nature of the wake dynamics.

In rotor-stator-interaction – RSI, the strength will be determined by the non-uniformity of the flow field e.g. exiting the guide vane section of a turbine. This non-uniformity will consist of a velocity variation due to pressure differences between adjacent vanes as well as the viscous wake due to drag on individual vanes. The viscous wake will, as described above, also be characterized by unsteadiness and it is of interest to map the impact of this unsteadiness on the pressure source strength in rotor-stator-interaction.

A method has been developed where CFD is used for mapping pressure and lift variations on a 2D impeller blade when the blade runs through a wake from a cylinder [2]. The stationary hydrofoil will shed different structures in the wake depending on the angle of attack (AoA) and reference speed. In this case plain hydrofoils and hydrofoils equipped with vortex generators, VGs, are investigated. The VGs are included in order to investigate whether an expected decrease in shed vortices will reduce RSI dynamics [4]. It is therefore possible to investigate the consequence on Rotor Stator Interaction RSI

for various hydrofoil configurations; i.e. frequencies and strengths, but also the phase dependency. Here the phase dependency is defined as the difference in time from when the blade cuts through the wake compared with the instant a wake structure was shed from the hydrofoil.

The TRPIV data have a high resolution in both time and space. The impact of a viscous wake, with actual unsteady characteristics, can be modeled by extracting temporal velocity information from a linear rake (y-direction) from the 2D field of view from the PIV measurements, and finally included as the inlet flow boundary condition in the 2D CFD calculation.

The paper will include a brief description of the measurements made, and the results of applying the characterization method on the hydrofoil data.

## Introduction

Secondary and unwanted flow fields are known to cause various problems in hydro turbines and other rotating fluid machinery. Pressure pulsations originating from the rotor stator interaction (RSI) are always present, but not always a problem. Unfavorable RSI conditions occur from wicket gates generating large and relatively low velocity wakes due to large drag, unfavorable flow direction onto rotor, and when the distance between wicket gates and rotor is at minimum, such as fully open wicket gates. Other factors influencing pressure pulsation hazard, are pressure pulsation magnitude, structure thickness, structure material and resonant frequencies. When dimensioning the turbine, pressure pulses are assumed to add a load of constant amplitude and frequency to the turbine structure. This is far from reality as the pressure pulses are highly dynamic. The task of this paper is to investigate the rotor stator interaction similar to the pressure fluctuation occurring as a runner blade passes through the wicket gate wake, with focus on the dynamics of this occurrence. It is important to gain knowledge on the dynamic behavior of a wake with a rotor blade passing through in order to prevent machinery of such character fail from this. A method [2] has been developed to investigate wake dynamics as well as predict the RSI phenomenon through various approaches based on a combination of experimental data and numerical simulation. This paper demonstrates the method on hydrofoils with and without mounted vortex generators. Experimentally obtained wake data will be processed using classical observation of wake parameters, and novel methods for finding coherent structures in the wake applying Proper Orthogonal Decomposition. Furthermore by direct inclusion of experimental data as input in a 2D CFD calculation, the characteristics of an actual RSI event will be observed.

## Experimental set-up

### PIV Measurements in UMN-SAFL Water Tunnel

The tests were performed at the high-speed water tunnel at Saint Anthony Falls Laboratory (SAFL), see Figure 1, by Bjarte Grytli Seim as a part of his master's thesis in April 2009. The tunnel was originally built as a free surface test facility but was later modified and is now mostly used for normal water tunnel operation. The test section has a length of 1200 mm, a height of 190 mm and a width of 190 mm. Visual observations are through the bottom window and the two side windows. The velocity and the pressure in the tunnel can be regulated independently.

The pressure in the tunnel can be adjusted from about 15 kPa to 200 kPa. The measured uniformity of the flow is better than 1 % and the turbulence level is found to be approximately 0.3 % [8].

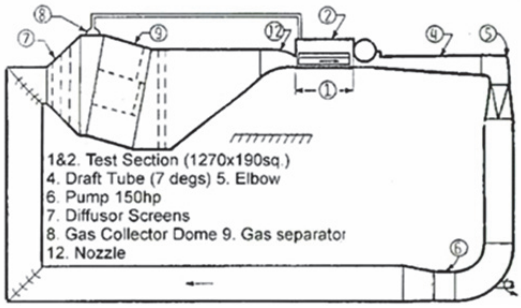


**Figure 1 - The Saint Anthony Falls Laboratory water tunnel**

The tests were performed on a hydrofoil, k=81 mm, for different angle of attacks (AoAs) at reference speed U=9 m/s. Tests are carried out on plain (denoted plain-AoA) hydrofoils and on hydrofoils where 1mm V-shaped vortex generators (denoted V1-AoA) are mounted in the rear section of the suction side.

**Figure 2 – Hydrofoil**

**Figure 3 – Vortex generators V1**

Both plain and VG-mounted hydrofoils were tested for AoA ranging from 0-10 degrees with 2 degrees increment. The sampling frequency was 10 kHz and the sampling time was 0.1 sec.

The PIV equipment that was used was composed of a Nd:YAG laser (Neodymium: Yttrium Aluminum Garnet), Photonics DM30-527. This laser can deliver pulses with energy content of 10 – 400 mJ/pulse. The seeding was hollow glass beads. For taking the photos a high speed camera of the type Fastcam APX-RS was used. This can take images at a frequency up to 10,000 Hz. When taking images at 10,000 Hz, the resolution of the image could be up to 512 by 512 pixels. Higher image resolution is possible at lower frame rates. The lens that was used for the high speed camera was a 105mm Nikon lens.

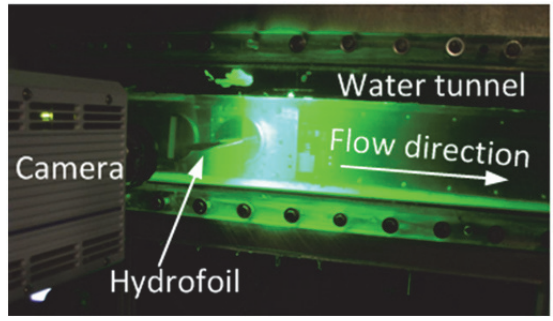


**Figure 4 - PIV measurement setup, with camera, water tunnel, hydrofoil and laser**

The pressure was measured 165 mm upstream the hydrofoil to calculate the water velocity, U in the test section. The pressure measurements were made with a LabView based acquisition program. All the PIV recordings were done with another PC with the DaVis7 software installed.

## Processing of Experimentally Obtained Data

The experimental data is recorded as images of particles in the flow. For the hydrofoil setup, the images are captured at 10 000 fps for 1000 time steps. This results in 1000 images for each setup. The images have to be transformed into vector fields, and later into physical coordinates and velocity data. In order to serve well as input data in CFD

calculations, the experimental data must go through several steps of pre-processing. The important steps of the preprocessing are as follows:

### Pre-Processing in PivView

The area of interest is cropped to avoid disturbing elements. Dimension of the image is 59.6 x 50.9 mm (436 x 511 pixels) starting 8.9 downstream the trailing edge.

### Vector Calculation in PivView

To ensure good conversion of the velocity from images to vectors, several settings must be set correctly. Most important is the time/distance scale. Here, 1 mm equals 8.57 pixels, and the time delay is 1 µs. There are various interrogation algorithms, filters and validation methods. An iterative interrogation from 256 x 256 ending at 6 x 6 pixels with 50 % overlap was chosen. All settings were saved in a parameter file used in the batch conversion.

### Batch Vector Calculation in PivView and LabView

The vector calculating software in PivView was implemented in LabView so batch vector calculation of all images could run smoothly. This step converted all images to coordinates (169 x 144 grid points) and corresponding u-v velocity components.

### Extracting a Constant x Velocity Profile

A velocity rake at x/k=0.235 was extracted for each time step.

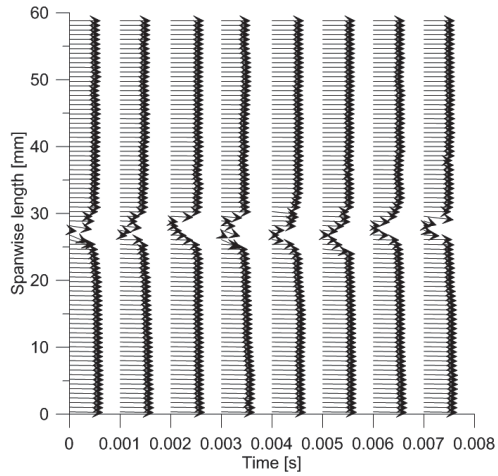


**Figure 5 - Snapshots of vector fields at x/k=0.235 behind the case plain-AoA10 at U=9 m/s**

### Mass Controlling Each Time Step

All velocity rakes were mass flow controlled, and corrected to avoid mass fluctuations in the CFD calculation. The corrections are small and maximum 3.5 % of the original value. At last the files are written in the format Fluent requires for input files.

## Methods for Characterizing Rotor Stator Interaction

### Analytical evaluation of rotor stator interaction

A simplified approach to rotor stator interaction is to observe the motion of the relative velocity vector (w) as the runner leading edge propagates through the wake. The velocity diagram at the inlet of the runner is a shown in Figure 6.

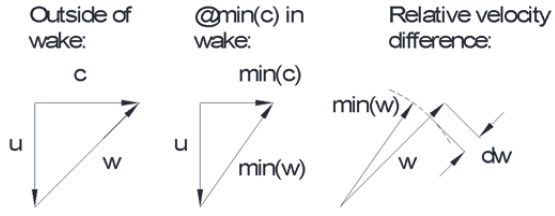


**Figure 6 – Velocity diagram at rotor inlet**

**inside and outside wake flow field**

Figure 6 shows the velocity diagram at the inlet of the runner. (I) when outside of the viscous wake, and (II) when the leading edge is within the wake. The difference in relative velocity (Δw) between situation (I) and (II) can then be found as shown in (III).

Linear differential analysis allows us to express the change in relative velocity magnitude (Δw) as a function of the maximum wake velocity deficit (Δc), see eq. (0.1). Knowing the change in magnitude, a linear estimate of the variation in the stagnation pressure ($\Delta p_{stag}$) can also be given.

$$\Delta w = \left( \frac{1}{\sin\beta_0} - \frac{c_0 \cdot \cos\beta_0}{\sin^2\beta_0} \cdot \frac{1}{u + \frac{c_0^2}{u}} \right) \Delta c \tag{0.1}$$

where

$$\Delta c = \max\left(\Delta c_j\right) \tag{0.2}$$

$$\Delta c_j = c_0 - \overline{c_j} \tag{0.3}$$

$$\overline{c_j} = \frac{1}{N}\sum_{i=1}^{N}\left(c_j\right)_i, \quad j \in [1, 169], \; N = 1000 \tag{0.4}$$

and

$$\beta_0 = \arctan\left(\frac{u}{c_0}\right) \tag{0.5}$$

Then $p_{stag}$ can be found from

$$\Delta p_{stag} \approx \rho w_0 \Delta w \tag{0.6}$$

The pressure variation at the leading edge of the rotor, hereafter referred to as tip, is monitored during the CFD calculations; both the position of the stagnation point and the amplitude. The magnitude of the variation is calculated using eq. (0.7)

$$\Delta p_{stag,CFD} = 2 \cdot \sqrt{2} \cdot stdev\left(p_{stag,i}\right), \; i \in [1, 4000] \tag{0.7}$$

In Figure 11 the calculated stagnation pressure together with the pressure variation magnitude using eq. (0.7) are shown.

## Numerical Simulation of Rotor Stator Interaction

Experimentally obtained velocity profiles are introduced in the computational domain, by letting the velocity inlet boundary condition take the value from actual PIV measurements.

With reference to Figure 7, the velocities from the PIV measurements will be taken from a rake, with length $b_0$, at a distance $s_0$ downstream the trailing edge of the hydrofoil. The very same position corresponds to the inlet boundary condition for the stationary domain in the sliding mesh approach selected.

In order to characterize the RSI of the mentioned wakes, all of them will be transported through the stationary domain of length s1, and enter the rotating domain containing the 2D runner blade. The velocity triangle at the tip of the runner blade is such that nominal incident angle of attack is close to zero degrees. The flow will exit the blade with an induced swirl.

The rotor blade is characterized by a tip radius R. This is selected to correspond to the thickness of the NACA0015 hydrofoil for which comparable experiments has been made. For simplicity the chord length of the runner blade will be of a similar value as that of the same hydrofoil, k=81 mm.

The Rotor Stator Interaction (RSI) case is modeled 2D in Fluent. It consists of a stationary domain with static mesh and a rotor domain containing a passing foil with a sliding mesh. Meshing is done in Gambit, and is structured with refined boundary layer along the rotor structure.

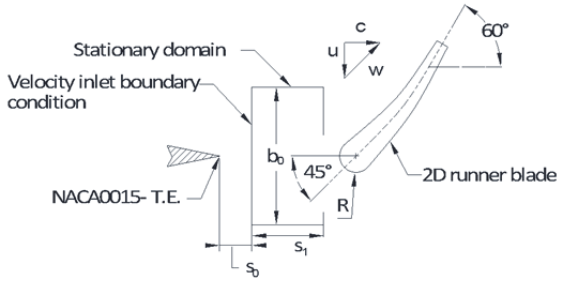


**Figure 7 - CFD model set up when experimentally obtained velocity profiles are included into the computational domain**

### Problems Running an Incompressible Solution

Due to mass oscillation between each time step causing unrealistic pressure variations when importing the data into Ansys Fluent, the simulations had to be run compressible. This allowed small changes in density in order to remain a realistic pressure field. The error in mass conservation was absorbed by small and negligible changes in density. The mass oscillations are believed to originate from different integration algorithms in LabView and Fluent.

## Results and discussion

### Analytical evaluation of rotor stator interaction

Two different approaches have been used to determine the stagnation pressure at the leading edge of the rotor:

Based on statistical evaluation of the inlet velocity profile, $\Delta c$ has been determined and $\Delta w$ and $\Delta p_{stag}$ has been evaluated using eq. (0.6) and eq.(0.7). Based on observation of stagnation point pressure during the CFD calculation the variation has been mapped. The results are tabulated in Table 1, and Figure 8 provides a graphical comparison between the two approaches.

| AoA | foil | 0 | 2 | 4 | 6 | 8 | 10 |
|---|---|---|---|---|---|---|---|
| $c_0$ [m/s] | plain | 8.91 | 9.27 | 9.13 | 8.98 | 8.7 | 9.21 |
| | V1 | 9.17 | 9.09 | 9.08 | 8.86 | 8.97 | 9.1 |
| Δc [m/s] | plain | 1.51 | 2.42 | 2.60 | 2.71 | 2.70 | 4.01 |
| | V1 | 1.51 | 2.10 | 2.64 | 3.33 | 3.90 | 4.74 |
| Δw [m/s] | plain | 1.13 | 1.78 | 1.92 | 2.02 | 2.04 | 2.95 |
| | V1 | 1.11 | 1.55 | 1.96 | 2.49 | 2.90 | 3.51 |
| $\beta_0$ [deg] | plain | 48.3 | 47.2 | 47.6 | 48.1 | 49.0 | 47.4 |
| | V1 | 47.5 | 47.7 | 47.8 | 48.5 | 48.1 | 47.7 |
| w [m/s] | plain | 13.3 | 13.6 | 13.5 | 13.4 | 13.2 | 13.6 |
| | V1 | 13.5 | 13.5 | 13.5 | 13.3 | 13.4 | 13.5 |
| Δp eq. 1.6 [Pa] | plain | 17.7 | 28.4 | 30.6 | 31.9 | 31.8 | 47.2 |
| | V1 | 26.7 | 24.7 | 31.0 | 39.1 | 45.9 | 55.8 |
| Δp CFD [Pa] | plain | 14.2 | 13.9 | 13.2 | 11.7 | 13.1 | 18.5 |
| | V1 | 21.8 | 16.8 | 17.6 | 21.2 | 25.1 | 26.4 |

**Table 1 – Velocity components and stagnation pressure calculated through linear analysis and observed in 2D CFD. u is selected to 10 m/s for all CFD calculations. The density of the fluid in the CFD calculations is ρ=1.22 kgm-3.**

As can be observed from Table 1 and Figure 8, a significant difference between estimated pressure variations based on averaged wake analysis and actual impact is present. This difference is visualized in Figure 11. As of now the difference between the two approaches can be explained with the highly dynamic velocity field downstream the hydrofoil. In **Figure 11** the dynamics is seen when plotting standard deviations together with the average velocity deficit. It must be emphasized that the above analysis is made on the x-velocity component only. For the flow field downstream the foil the y-component, or traverse flow direction, can be

of the same order of magnitude as the x-component. The dynamics of the wake will be highly transient in a stationary frame of reference. However it's evident that well defined structures can be shed. For a complete description of the dynamics two different approaches can be made:
- Characterization of the wake using standard spectrum methods in a typical cross section in the flow field.
- Characterization by the mapping of flow structures in the flow field by the POD analysis.

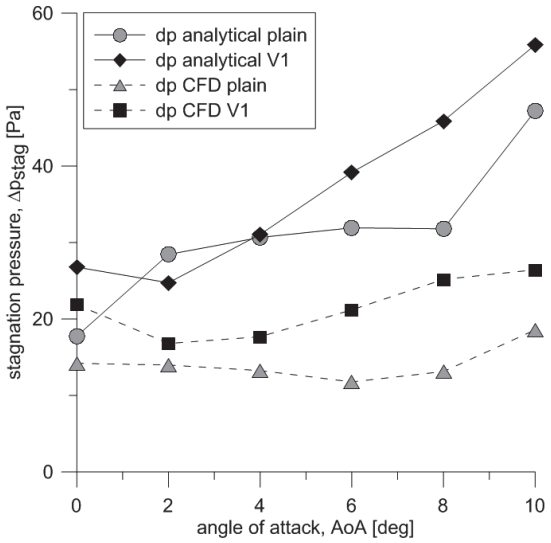


**Figure 8 – Tip pressure, the pressure at the rotor stagnation point, calculated through analytical method and from CFD**

Figure 9 shows that turbulence intensity increases as expected for higher angles of attack. Turbulence intensity also increases with VGs mounted compared to plain foils.

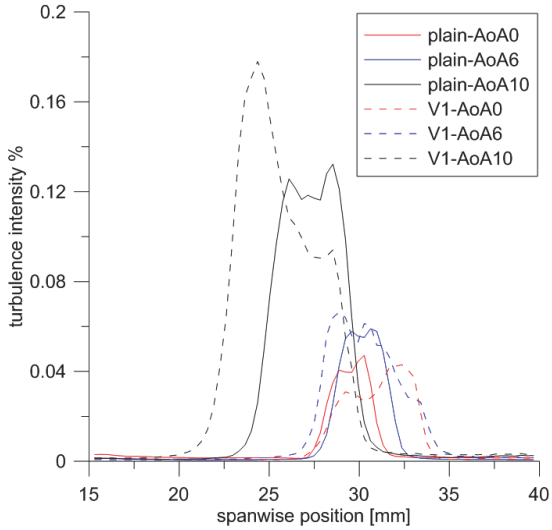


**Figure 9 – Turbulence intensity for various AoA**

Figure 10 shows the frequency spectrum of a point in the center of the plain wake at x/k=0.235 for various AoAs. Note that no distinct shedding peaks are observed as expected, except for AoA8 where the peak is significant at 787.3 Hz. The frequency can occur from coinciding with a resonant frequency of the system. It can also be the shedding frequency, as previous work [1] indicates expected shedding frequency at around 800 Hz at ref. speed of 9 m/s for a NACA0009 hydrofoil.

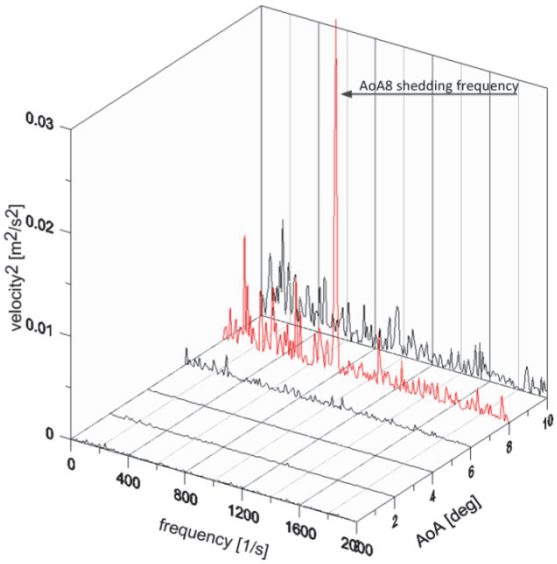


**Figure 10 – Frequency spectrum of span wise velocity component v in center of the plain foil wake at x/k=0.235**

## CFD Results

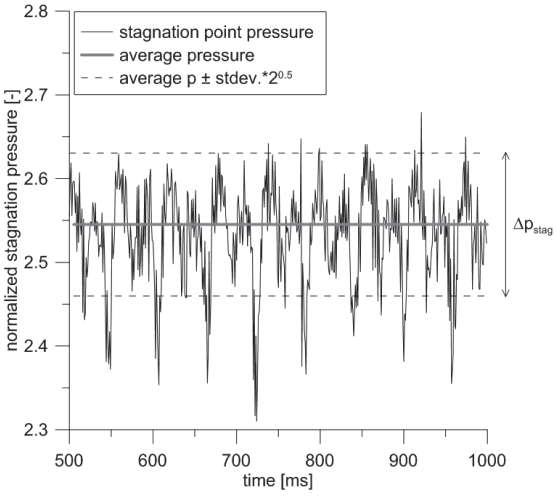


**Figure 11 – Normalized tip pressure, average pressure and average pressure ± standard deviation calculated using CFD for case plain-AoA10**

Tip pressure is normalized by:

$$p_{norm} = \frac{p_{stag}}{\frac{1}{2}\rho w^2} \tag{0.8}$$

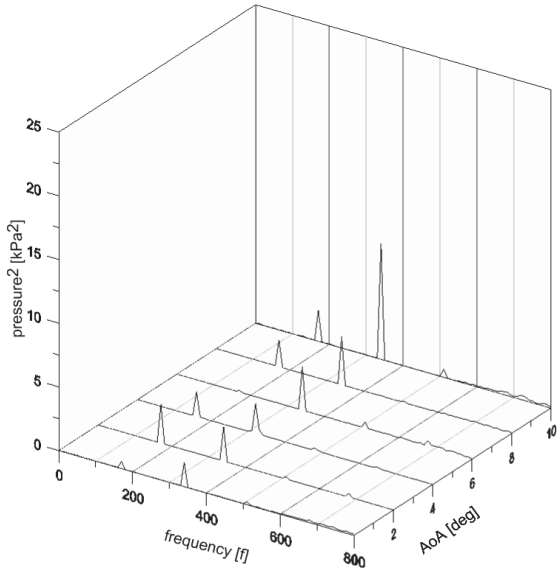


**Figure 12 – Frequency spectrum of plain rotor tip pressure**

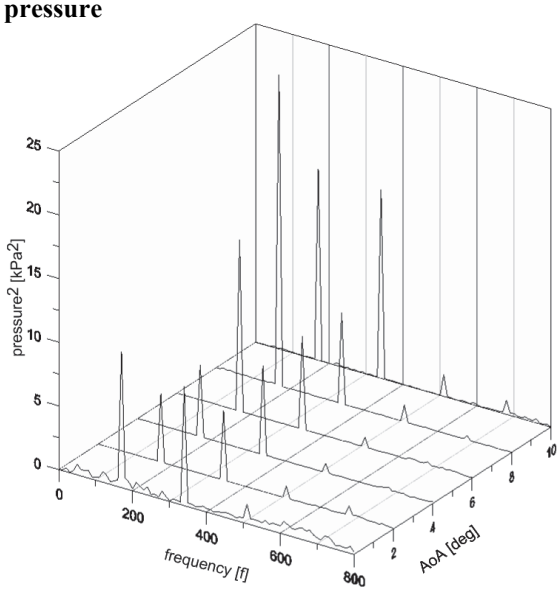


**Figure 13 - Frequency spectrum of V1 rotor tip pressure**

Figure 12 and Figure 13 show the frequency spectrum of the stagnation pressure observed at the rotor tip for plain and V1-foils respectively. The dominant frequencies observed is the rotor passing frequency at 172.1 Hz and its multiples. The amplitude is greater for all V1 cases which were not anticipated.

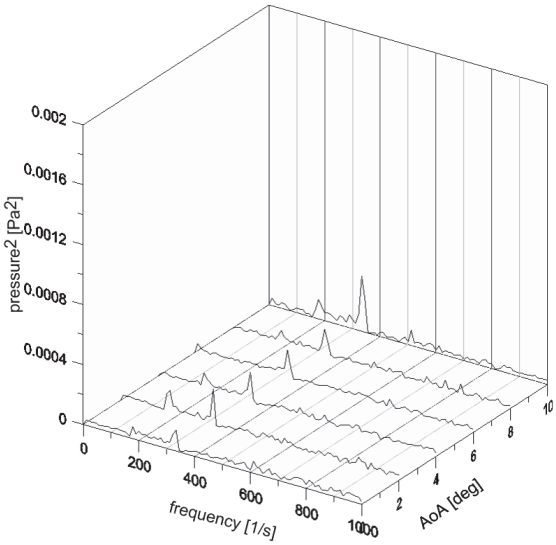


**Figure 14 – Frequency spectrum of plain foil lift force**

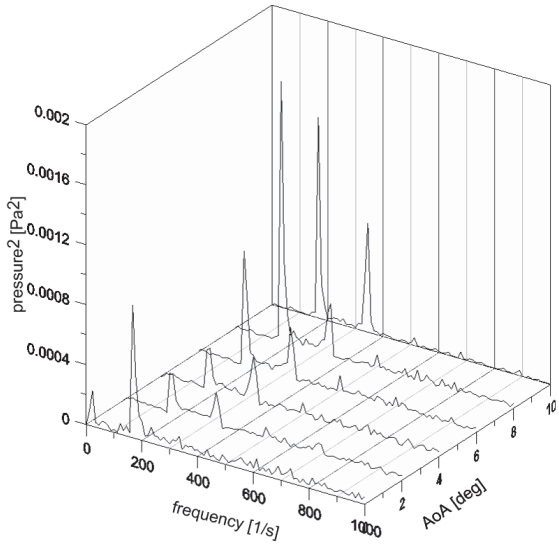


**Figure 15 – Frequency spectrum of V1 foil lift force**

The frequency spectrum of the lift force is showed in Figure 14 and **Figure 15**. The dominant frequency is the 1st multiple of the rotor passing frequency at 344.2 Hz.

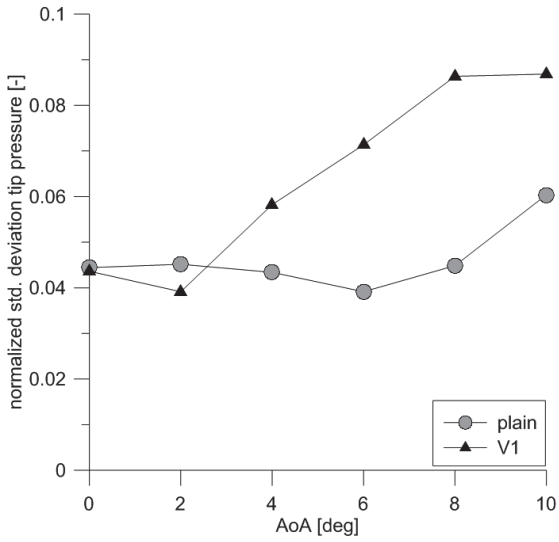


**Figure 16 – Standard deviation of the normalized tip pressure**

Standard deviation of the stagnation pressure at rotor tip can be seen in **Figure 16**. The vortex generators are favorable only for AoA equal 0 and 2 degrees. In the other cases the plain foil yields lower standard deviation.

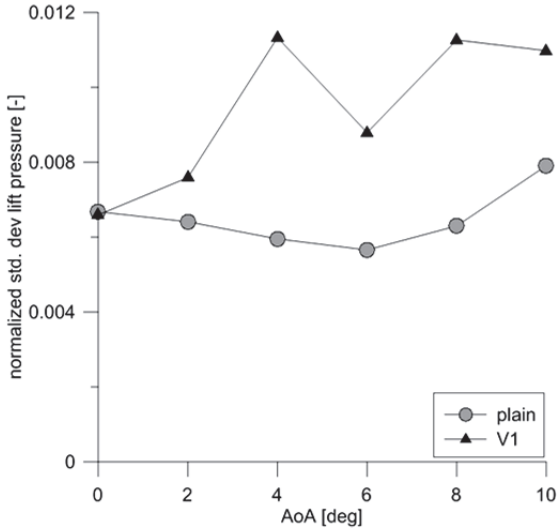


**Figure 17 – Standard deviation of the normalized lift**

The lift force is normalized by:

$$L_{norm} = \frac{L}{\frac{1}{2}\rho w^2 k} \qquad (0.9)$$

The standard deviation of the lift force is plotted in Figure 17. Vortex generators prove larger standard deviation also here for all cases except AoA0.

## POD

POD (Proportional Orthogonal Decomposition) is a powerful mathematical tool which can describe large scale dynamics of a turbulent flow. A deterministic function is projected onto the stochastic field and maximized through a Fredholm integral value problem of the second kind. The dynamics is then described through a finite number of eigenfunctions with corresponding eigenvalues sorted in descending order. Mode 1 contains the most energy, and all modes represent 100 % of the flow energy. One set of eigenfunctions and eigenvalues is referred to as a mode. Addition of all modes will fully reconstruct the original velocity field. The method is described in further detail in [2, 3, 5-7].

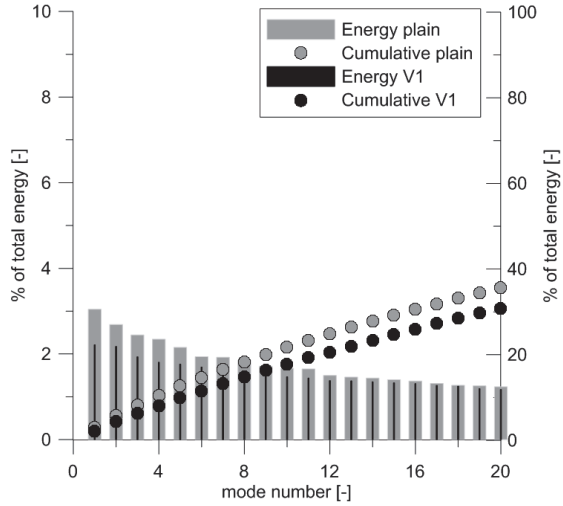


**Figure 18 – POD energy AoA2**

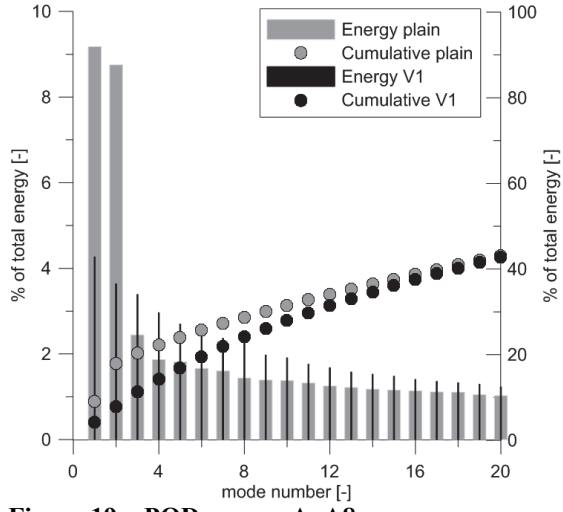


**Figure 19 – POD energy AoA8**

Energy distribution is showed for the first 20 modes for AoA2 and AoA8. AoA2 show only slight decrease in energy in the first modes for the V1 foil, while AoA8 show significant decrease in energy for the two first POD modes. Hence the energy is spread over the other modes since the turbulence is more uniform without large structures. The AoA8 case was the only case showing clear vortex shedding similar to what sheds off a cylinder in the reconstruction field. Vortex shedding off a cylinder is characterized by two large alternating vortices shedding alternately from top and bottom side. POD analysis shows that up to 55 % of the total energy can be found in the two first modes.[2] The VGs tend to smooth out the large structures for case AoA8. Some cases, like AoA0 proved to get more energy in the first modes when applying VGs.

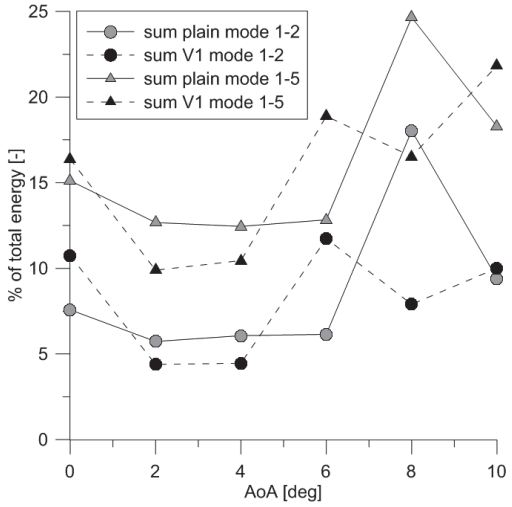


**Figure 20 – Energy in first 2 and 5 POD modes**

POD analysis show in general very small decrease of energy in the first one to five modes when comparing plain and V1-foil, as presented for AoA2 in Figure 18. Some cases, AoA0 and AoA6 show increase in mode one for the V1-foil, but this is due to a large structure observed outside the wake area, or at the left boundary of the wake. Those structures seem unphysical, and originate incorrectly from the POD algorithm. Thus should not this energy be addressed to the first mode only.

Plain-AoA8 proves to contain a larger amount (18 %) of energy in the two first modes than rest of the cases. This energy, in terms of distinct shedding pattern, is noticeably suppressed by the VGs as expected. Hence the energy is distributed across the later modes, which means large and distinct flow structures are suppressed.

Figure 20 shows that more energy is present in the first 2 and 5 modes as AoA increase from 2 deg. Larger AoAs result in larger scale structures in the wake. E.g. when the foil stalls, large structures will shed off the foil similar to what sheds off a cylinder. More energy for the early AoA0 and AoA6 V1-modes as shown in **Figure 20** can be explained by the large unphysical flow structure that appeared in the POD analysis for those cases. Else, the V1-cases prove to have less energy in the early modes, hence less large flow structures.

## Summary and conclusions

Two methods [1] for quantifying the unsteady load on rotating members due to wakes shed from upstream stationary cascades are demonstrated. The methods include both a time-averaged analytical- and a transient numerical approach. The demonstration is made using experimentally obtained transient wake flow fields downstream hydrofoils. The experimental data exist for a number of various configurations; i.e. different Reynolds

number, angle of attacks (AoA) and with the use of vortex generators (VG).

The wake flow fields themselves are also characterized by unsteady features; i.e. shed structures. The CFD quantification technique will capture these structures, while the analytical technique will not. In order to investigate the nature of said structures, and eventually their impact for Rotor-Stator-Interaction, the wakes are analyzed using spectrum techniques and proper orthogonal decomposition (POD).

The leading edge tip pressure variation has been observed, see Figure 8. The results of the study using the analytical technique show that the pressure variation at the rotor tip is increasing as AoA increases, especially with VGs mounted. For the CFD calculation the results show almost constant value for tip-pressure variation regardless of AoA, but lower than calculated analytically. The VG configuration shows poorer performance than the plain hydrofoils also for the CFD technique.

The turbulence intensity (T.I.) is increasing, as expected, in amplitude and width for increasing AoA, see Figure 9. Also an offset of the maximum T.I. level is observed for hydrofoils with a VG configuration.

No distinct frequencies are found when examining the hydrofoil wake, as compared to the cylinder wake [1]. There is one exception though, at the plain-AoA8 case where large amplitude is observed at 787.3 Hz. No other case has such distinct frequency spike at this frequency, although other cases indicate deflection at similar or double frequency.

When applying FFT on the tip pressure and lift force, the rotor passing frequency, 172.1 Hz, is easily recognized in all cases. So is the 1$^{st}$ multiple of this frequency at 344.2 Hz. The multiple has in some cases larger amplitude than the rotor passing frequency. When the same approach was applied on a cylinder [1], both the rotor passing frequency, shedding frequency and rotor passing ± shedding was observed in the tip pressure spectrum. For the movement of the stagnation point the shedding frequency was even the most dominant. Since no distinct shedding frequency is observed in the hydrofoil wake, except for plain-AoA8, it is neither recognized in the FFT of tip pressure, stagnation point or lift force variation for any case.

The standard deviation of the tip pressure for plain and V1 hydrofoil slightly decrease when VGs are mounted for AoA0 and AoA2, while it increase for AoAs greater than 2 deg. Standard deviation of plain tip pressure remains almost constant for plain foil, except for AoA10, while it increase rapidly for AoA greater than 2 deg for the V1 foil.

Standard deviation of lift force results is similar to standard deviation of tip pressure. Plain foil results are almost constant, except for AoA10, while V1 data increase with increasing AoA. Though with an unexpected data point at V1-AoA4.

Mounting of VGs was expected to increase the performance in terms of less shed dynamics, and therefore reducing the dynamics of the tip stagnation pressure and lift amplitude in Rotor Stator Interaction. The poor performance of the VGs can be linked to a larger parasitic drag due to the increase of frontal area, as well as possible

premature flow separation. The mentioned secondary effects will create a fatter wake, and hence increase leading edge tip dynamics. Only velocity information was used at the input in the CFD, but the pressure term also plays an important role shortly downstream the foil. This may explain deviation between analytical and CFD-method as well as poor VG performance in several cases.

POD analysis has proved to work as a useful tool, to visualize flow structures in the flow, although some results tend to be false. The POD analysis in general showed slight decrease in energy of the first modes of the foil with vortex generators compared to the plain hydrofoils. Note that the analysis showed very promising results for AoA8, while errors occurred in the analysis for AoA0 and AoA6, resulting in poor results for those cases.

Shedding of defined structures was only seen for plain-AoA8, and this frequency was not found in the CFD calculated dynamics of tip pressure, stagnation point or lift force variation.

This paper has demonstrated several methods for revealing RSI dynamics based on known wake characteristics:
- An analytical method dependent on the average characteristics of the wake.
- A direct approach using instant conditions of the wake flow field through a given downstream position as input in a 2D CFD calculation.
- POD analysis of the whole TRPIV obtained flow field.

The POD analysis applied in order to understand if the wake, and hence the CFD input, contains shed coherent structures.

## Acknowledgements

The authors are grateful for the contribution by Statkraft who initially funded the wake flow experiments at SAFL. Also the input from Bjarte Grytli Seim, who did most of the experimental work, is highly appreciated.

## Nomenclature

| | |
|---|---|
| AoA, $\alpha$ | = Hydrofoil angle of attack |
| $L$ | = Lift force |
| $L_{norm}$ | = Lift force normalized |
| $p$ | = Pressure |
| $p_{stag}$ | = Stagnation pressure rotor tip |
| $\rho$ | = Density |
| $t$ | = Time |
| $c$ | = Absolute velocity |
| $k$ | = Chord length |
| $u$ | = Rotor velocity |
| $U$ | = Free stream velocity |
| $w$ | = Relative velocity |
| x | = downstream position of hydrofoil |
| Re | = Reynolds number |
| plain | = Plain hydrofoil case |
| V1 | = Hydrofoil with vortex generators V1mm |
| VG | = Vortex generator |

## Subscripts

| | |
|---|---|
| $0$ | = Reference case, related to free stream velocity |
| $i$ | = Index |
| $j$ | = Index |
| wake | = When inside wake |

## References

[1] Ausoni, P., et al., 2006, *Kármán vortex shedding in the wake of a 2D hydrofoil: Measurement and numerical simulation*, in *IAHR Int. Meeting of WG on Cavitation and Dynamic Problems in Hydraulic Machinery and Systems*: Barcelona.

[2] Finstad, P.H.E., 2011, *Method for Characterizing Rotor Stator Interaction Using Experimentally Obtained Wake Flow Fields and CFD*, Vannkraftlaboratoriet, EPT, NTNU.

[3] Hilberg, D., W. Lazik, and H.E. Fiedler, 1994, *The Application of Classical POD and Snapshot POD in a Turbulent Shear Layer with Periodic Structures.* Applied Scientific Research. **53**: p. 283-290.

[4] Kuethe, A.M., 1973, *Control of noise and instabiloties in jet engines, compressors, turbines, heat exchangers and the like*, U.S. Patent, Editor.

[5] Lu, L.J. and C.R. Smith, 1991, *Velocity profile reconstruction using orthogonal decomposition.* Experiments in Fluids. **11**: p. 247-254.

[6] Lumley, J.L. and P. Bakewell, 1967, *Viscous sublayer and adjacent wall region in turbulent pipe flow.* The Physics of Fluids. **10**(9): p. 1880-1889.

[7] Tutkun, M., 2008, *Structure of Zero Pressure Gradient High Reynolds Number Turbulent Boundary Layers*, Chalmers University of Technology.

[8] Wosnik, M. 2005. *Description of SAFL high speed water tunnel and experimental equipment*. Available from: http://cav.safl.umn.edu/facilities.htm .

## 5.1 Additional hydrofoil results

### 5.1.1 Stagnation point dynamics

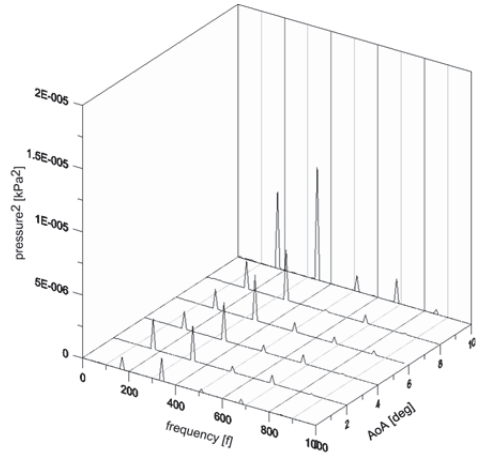


**Figure 25 – Frequency spectrum of stagnation point dynamics for plain case**

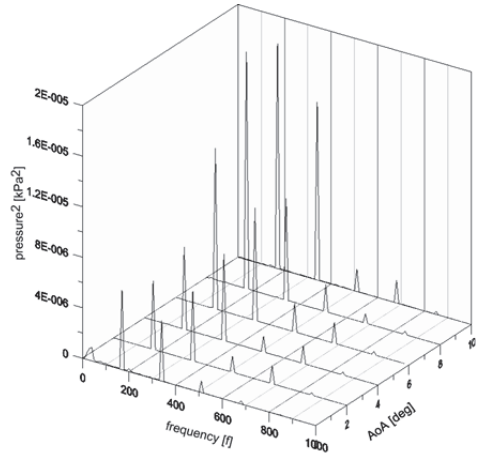


**Figure 26 – Frequency spectrum of stagnation point dynamics for V1-case**

Figure 25 and Figure 26 show the frequency spectrum of the dynamics in the stagnation point for plain- and V1-case respectively. The dominant frequencies are the rotor passing frequency and its multiples.

The wake energy addressed to vortex shedding in the hydrofoil wake was also compared from two different aspects as for the cylinder wake. POD-mode 1

and 2 contained 18 % of the total energy while the frequency spectrum of the v-velocity component averaged from 12x15 x-y positions respectively, addressed 20 % of the total wake energy to the vortex shedding for plain case AoA=8. Since no clear shedding frequencies were pointed out for the other AoAs, this comparison could only be done at AoA=8.

### 5.1.1 POD eigenfunctions

Contour plots of the eigenfunctions for the four first POD-modes for plain hydrofoil AoA=2 are shown in Figure 27 to Figure 30. The eigenfunctions for the four first POD-modes for V1 hydrofoil AoA=2 are shown in Figure 31 to Figure 34. The eigenfunctions for the four first POD-modes for plain hydrofoil AoA=8 are shown in Figure 35 to Figure 38. The eigenfunctions for the four first POD-modes for V1 hydrofoil AoA=8 are shown in Figure 39 to Figure 42.

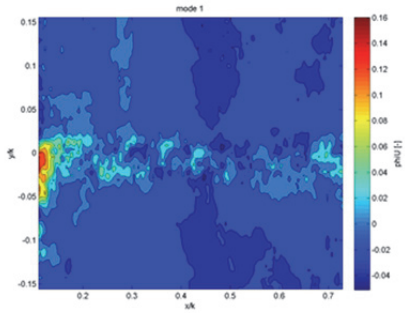


**Figure 27 – plain AoA2 mode 1**

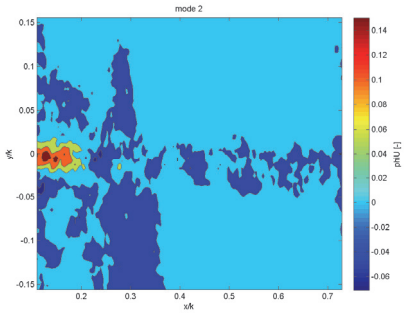


**Figure 28 – plain AoA2 mode 2**

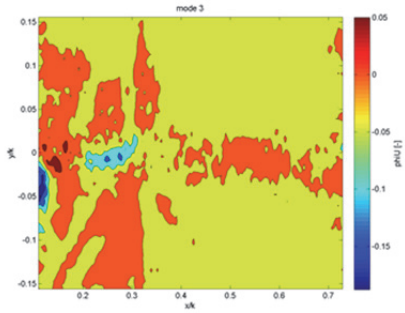


**Figure 29 – plain AoA2 mode 3**

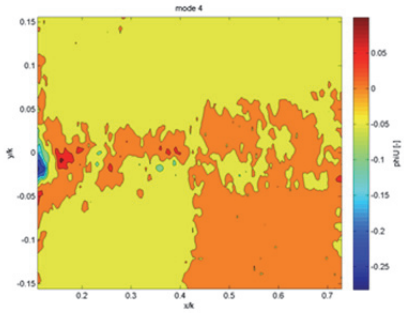


**Figure 30 – plain AoA2 mode 4**

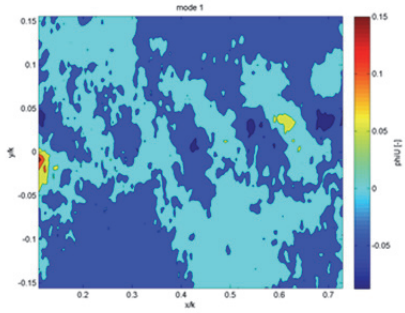


**Figure 31 – V1 AoA2 mode1**

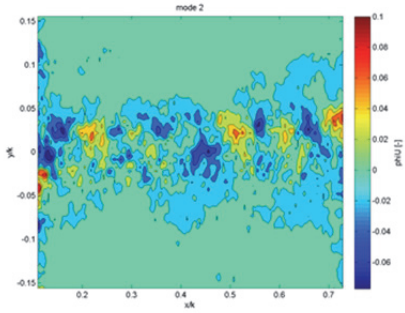


**Figure 32 – V1 AoA2 mode 2**

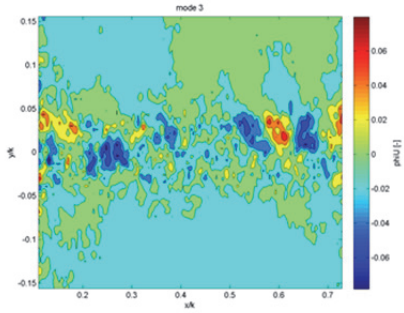


**Figure 33 – V1 AoA2 mode 3**

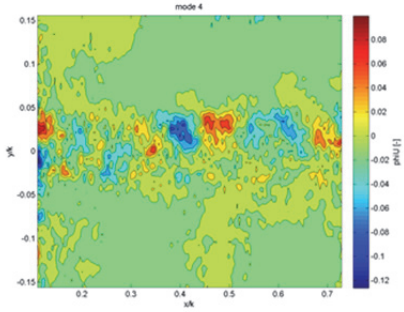


**Figure 34 – V1 AoA2 mode 4**

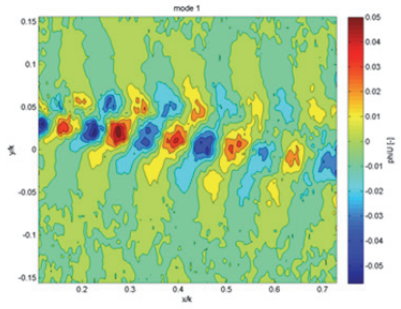


**Figure 35 – plain AoA8 mode 1**

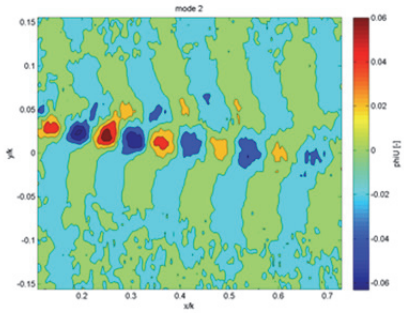


**Figure 36 – plain AoA8 mode 2**

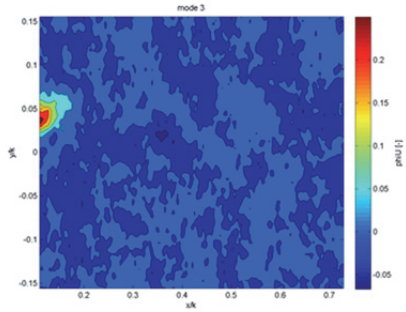


**Figure 37 – plain AoA8 mode 3**

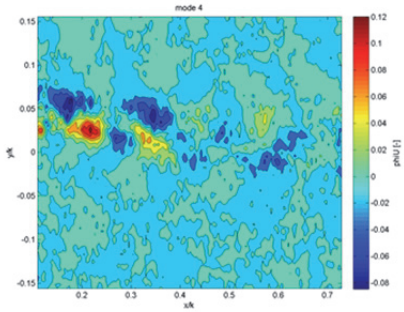


**Figure 38 – plain AoA8 mode 4**

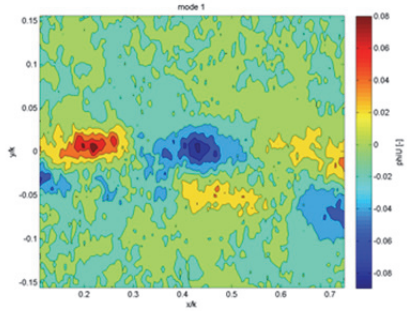


**Figure 39 – V1 AoA8 mode 1**

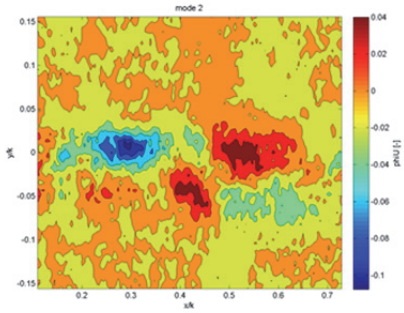


**Figure 40 – V1 AoA8 mode 2**

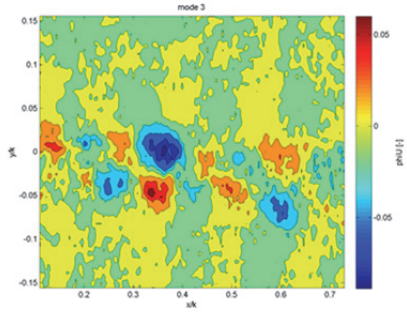


**Figure 41 – V1 AoA8 mode 3**

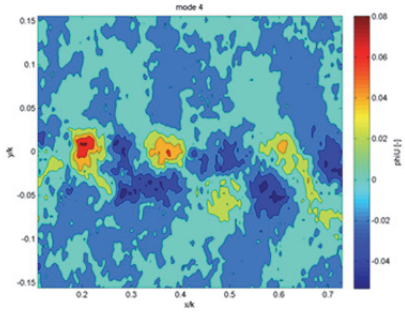


**Figure 42 – V1 AoA8 mode 4**

# 6 Draft tube flow

## 6.1 Background

It is evident that pressure pulsations in draft tubes can lead to vibrations, power fluctuations, structure fatigue, efficiency loss, noise, etc., all disturbing and possibly destructive effects in a power plant. Many studies are performed on the draft tube pulsations and draft tube surge. E.g. it's well known that the Rheingans frequency appears at part load when the draft tube flow surges and that it is approximately 1/3 of the rotational speed. [58] But yet is an explanation of its occurrence and behavior to be presented. The draft tube flow is highly dynamic, especially at off design points. Sources to the strong dynamics can be possibly vortex rope (Rheingans), disturbance from the draft tube bend further downstream, separation, shedding or cavitation on the runner blades in addition to an already turbulent flow which by nature fluctuates.

The objective of this work is to gain knowledge on the dynamics of the draft tube flow by investigating the pressure fluctuations in radial and tangential direction in a 2D plane of the draft tube. Earlier studies mostly perform wall measurements only. The 2D plane pressure data are to be analyzed with POD in order to map large structures of the flow.

## 6.2 Svorka Power plant

Svorka power plant was set into production in 1963 and is located in Surnadal in Møre og Romsdal. The power plant is owned and operated at a 50/50 share between Statkraft and Svorka Energi. The turbine

| Turbine | Power | Annual production | Head | Flow rate | Rotational speed | Speed number |
|---|---|---|---|---|---|---|
| Francis | 25 MW | 111 GWh | 260 m | 10 m3/s | 600 rpm | 0.3 |

**Table 3 – Svorka power plant data [73] [53]**

**Figure 43 – Svorka Power plant**

Svorka power plant is well suited for the radial draft tube measurements as it is easy accessible and not situated underground as most power plants. Svorka has already served as test facility for a water injection system [53] into the draft tube in order to reduce cavitation and draft tube pulsations. The experiences from this project are positive and good ballast for new investigations as the responsible company, FDB is involved in both projects. It is also of great value that the owners, Statkraft and Svorka Energi, are co-operative regarding installation of equipment and changing the production scheme. If the current work gives promising results, a natural continuation would be to measure with the water injection system activated.

## 6.3 Measuring equipment and procedure

### 6.3.1 Pressure transducers

The pressure transducers used in the experiments are full bridge cylindrical KULITE xcl152 with absolute range from 0-3.5 bar. They are small with a diameter of 3.8 mm and the output is a -0.25 - 0.25 mV signal.

### 6.3.2 Measuring probes

The two measuring probes of length Le=700 mm are made of stainless steel with outer diameter of $D_o$=20 mm and inner diameter $D_i$=4mm. Due to limited space between the wall and the draft tube the probes had to be designed to split in two parts. The two parts can easily be mechanically joined using a threaded connection. A handle is mounted at the back of the probes for easy operation.

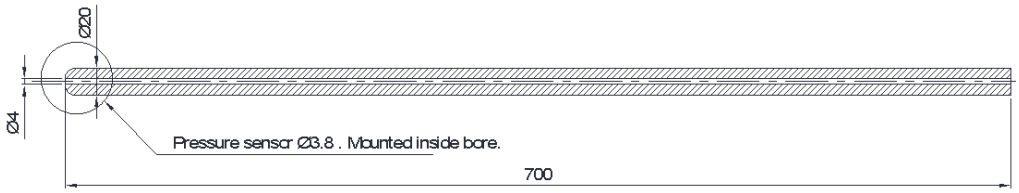


**Figure 44 – Sketch of measurement probe**

**Figure 45 – Measurement probe with sealing system. Part with threads is mounted to the valve which is screwed on the pipe stub**

### 6.3.3 Mounting of pressure transducers into probe

The pressure transducers were mounted flush with the end of the probe by silicon. Mounting the pressure transducers into the probes was a precise operation, and it was important that no silicon was spilled to the front of the transducer which could possibly clog and damage the sensor membrane. Once the pressure transducer is fixed the operation cannot be undone.

### 6.3.4 Pipe stubs and valves

8 holes were drilled in the draft tube at 1.22 m beneath the turbine separated by $\Delta\theta=30°$. In addition, 8 pipe stubs had to be designed and manufactured for mounting around the drilled holes in the draft tube. The pipe stubs have two purposes:

- Absorb the load as the probes are inserted into the draft tube
- Threads for mounting of valves

The pipe stubs have inner diameter $D_i$=20.2 mm and 1 inch outer threads for mounting the valves. Gate valves are mounted on the pipe stubs so the probes

can be inserted through the valve and pipe stub. SveenMek were hired for the drilling and mounting of the stubs and valves. A special sealing nut is mounted to the valve to ensure complete sealing between valve and measuring probe.

**Figure 46 – Drilling holes and mounting pipe stubs on draft tube wall**

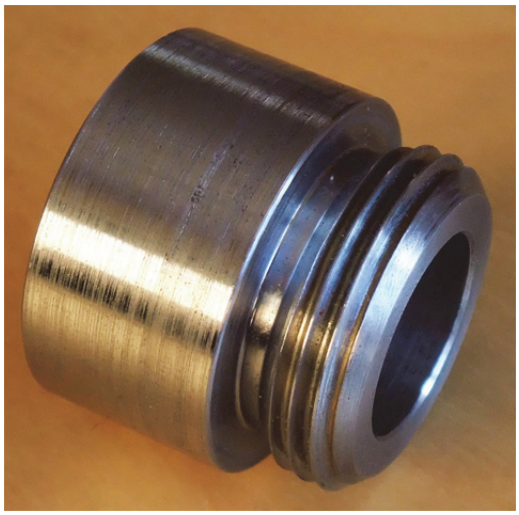

**Figure 47 – Threaded pipe stub**

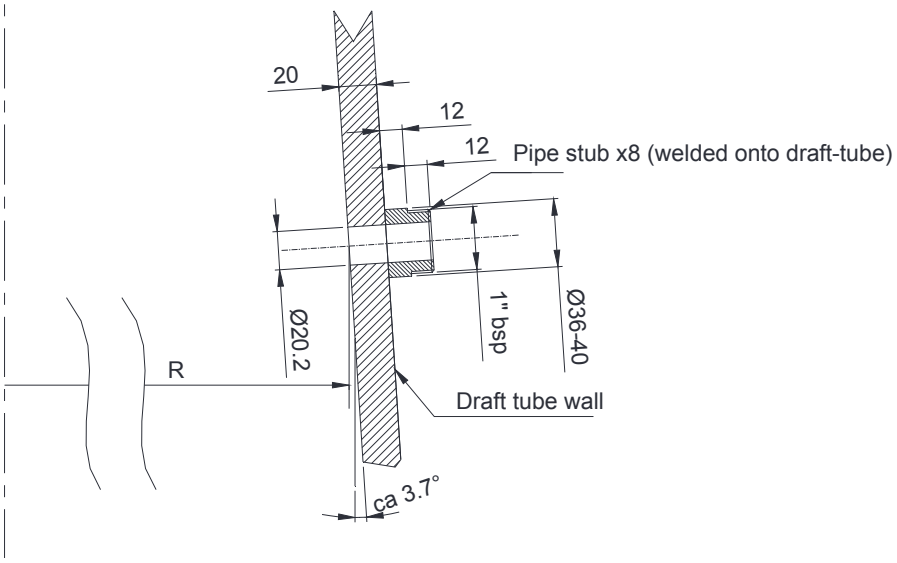


**Figure 48 – Mounting of pipe stub**

### 6.3.5 Calibration of pressure transducers

The KULITE xcl 152 pressure transducers were calibrated using a dead weight manometer. Calibration took place after the transducers were mounted in the probes.

The pressure transducer signal cable is connected to a National Instruments module, NI 9237 which is connected to a National Instruments cDAQ 9178. The signal is transferred to a laptop and read by a LabView acquisition program. By reading the output signal (mV) and knowing the exact pressure in weights put on the dead weight manometer the linear relation is obtained. The two sensors are named after the end of their serial number, and will further be denoted as P101 and P95.

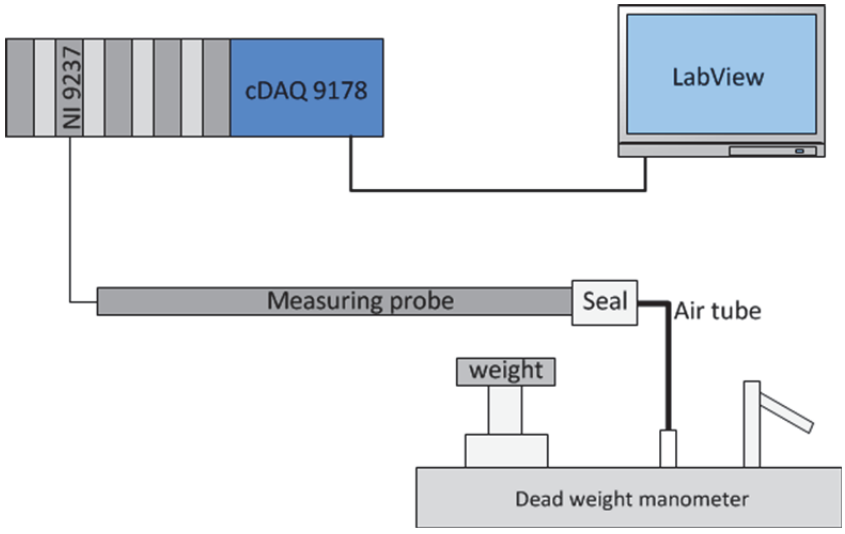


**Figure 49 – Calibration set-up**

The calibration results can be seen in Figure 50.

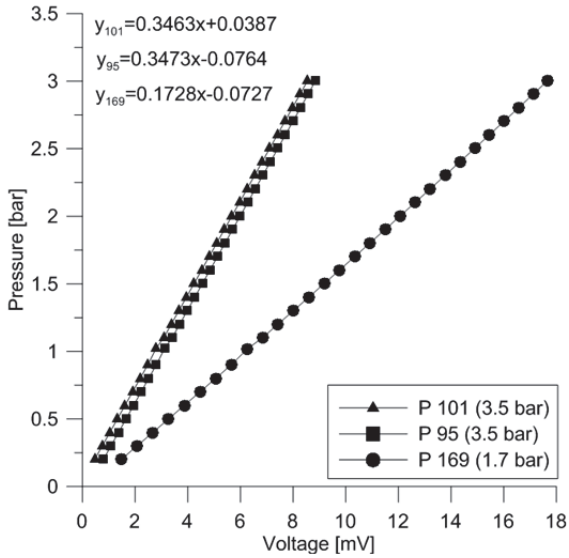


**Figure 50 – Calibration results for pressure transducers P101 and P95**

Note that the pressure is absolute. Following total systematic errors were obtained:

| Sensor | Max error in calibrated interval | Max error in measuring interval |
|---|---|---|
| P101 | 0.01833 % | 0.00875 % |
| P95 | 0.01806 % | 0.00873 % |
| P169 | 0.04306 % | 0.01206 % |

**Table 4 – Total systematic errors**

### 6.3.6 Measurement procedure

The pressure measurements take place in the draft tube downstream the turbine. While measuring, the turbine runs at constant power. One operation point have been investigated. P=12 MW, which is known for high pressure pulsations and cavitation. At this operation point the meridian flow through the draft tube is $U_m$ = 3.5 m/s. See measurement set-up in Figure 51 and the measurement scheme in Figure 52. The two measurement probes are used for paired measurements as described in Figure 52. Probe 1 is always located at θ=0°. Probe 1 is first held at constant r while Probe 2 is traversed at all r for the given θ. Then Probe 1 is moved one r increment and Probe 2 again traverses all radiuses at the given θ. This is repeated for all θs. Each θ-pair gives 6x6=36 measurement pairs. For 7 θ-pairs, it results in 252 pairs of measurements. For

the first pair, at θ=0°, the probes are aligned vertically, with 7.5 cm vertical separation. All other pairs are measured in the same plane.

| Δr | Grid points r | Δθ | θ-lines | T | f | # of pairs |
|---|---|---|---|---|---|---|
| 0.109 m | 6 | 30° | 7 | 90 sec | 10000 Hz | 252 |

**Table 5 – Measuring properties**

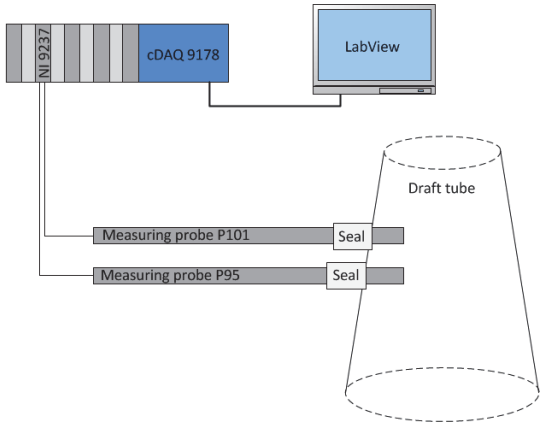


**Figure 51 – Measurement set-up**

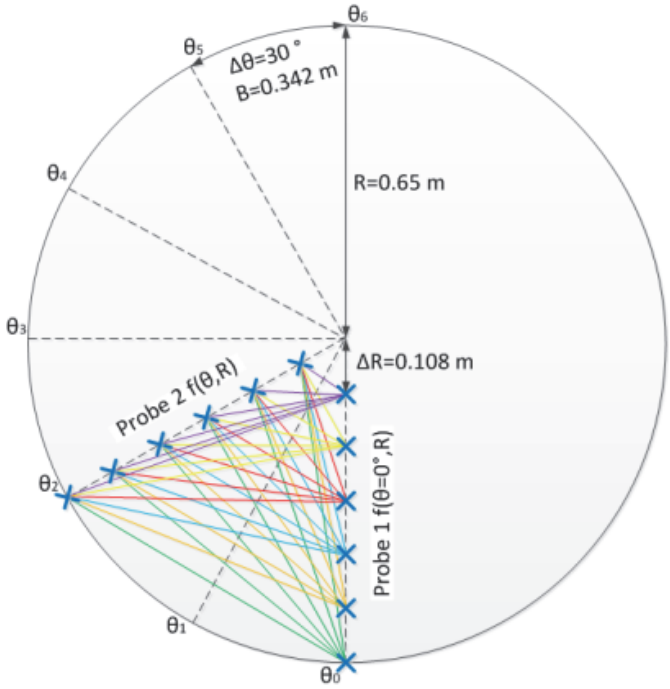


**Figure 52 – Measuring scheme in the draft tube**

**Figure 53 – Measurement in progress**

### 6.3.7 Challenges

Since the space between the wall and draft tube is limited, the measuring probes had to be divided in two connecting parts at some measuring points. The wires from the pressure transducers are located through both hollow parts of the probe and exiting at the end where they are connected to a more solid cable which connects to the cDAQ 9178. As the wires are very thin and vulnerable, caution must be taken when operating the probes and especially when the probes are divided. The rear part of the probe must be held my hand and not to be dropped as this will break the wires or pull out the pressure transducer from the probe.

During the first measuring session the P95 sensor drowned due to leakage through silicon seal where it was glued into the probe and from leakage through the probe joint. This sensor was later replaced by a new sensor denoted P169. The P169 sensor's range is 0-1.7 bar absolute and has threads which makes mounting into the probe and avoid leakage easier.

### 6.3.8 Data handling

All data are recorded by a LabView data acquisition program. Every operation point has a folder where every measurement pair is saved as a separate file. The data is saved as tab delimited .txt files so it is convenient for further post processing and for examining by POD.

### 6.3.9 Post processing

The data are further to be analyzed by POD (Proportional Orthogonal Decomposition) which is a mathematical correlation tool for mapping of dynamic structures and their energy portion of the total flow energy. In order to make the data ready for POD-analysis, some post processing is required.

## 6.4 Results

### 6.4.1 Statistics

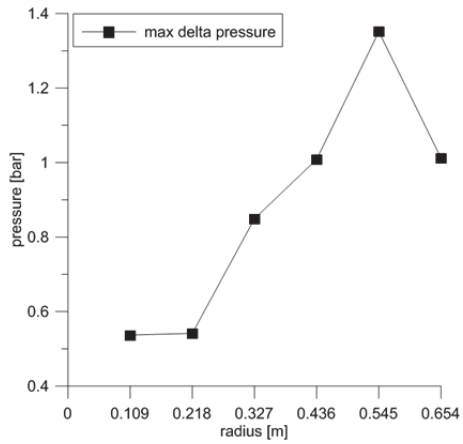


**Figure 54 – Maximum Δp 12 MW**

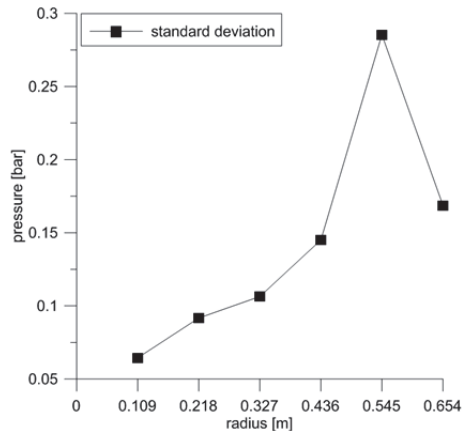


**Figure 55 – Standard deviation 12 MW**

Maximum pressure difference (peak to peak) and standard deviation as a function of the radius can be seen in Figure 54 and Figure 55 respectively. R=0.654 refers to the draft tube wall. The data are based on the θ=60° traverse measurements.

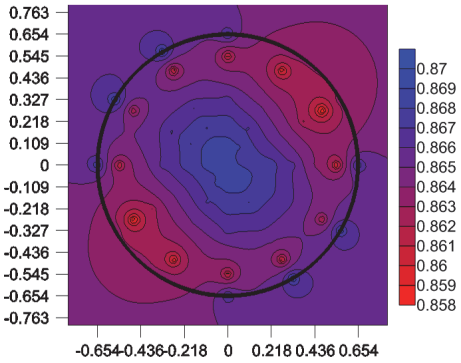


**Figure 56 – Mean pressure contours**

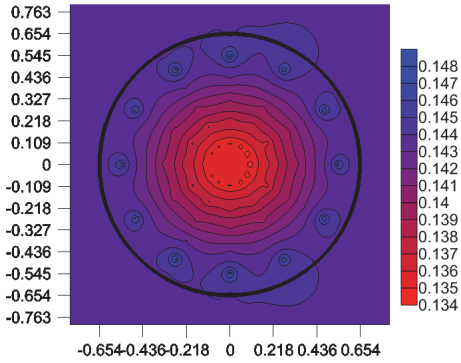


**Figure 57 – Std. dev. pressure contours**

Contours of the mean pressure and standard deviation of the pressure is plotted in Figure 56 and Figure 57 respectively.

### 6.4.2 Expected frequencies

| Turbine properties | Value | Denotation | Characteristic frequency |
|---|---|---|---|
| Rotational speed | 600 rpm | $f_n$ | 10 Hz |
| Rheingans | ≈0.3* fn | $f_R$ | 3.3 Hz |
| Runner vanes | 15 | $f_{RV}$ | 150 Hz |
| Guide vanes | 20 | $f_{GV}$ | 200 Hz |

**Table 6 – Characteristic frequencies of Svorka power plant**

### 6.4.3 Pressure fluctuations

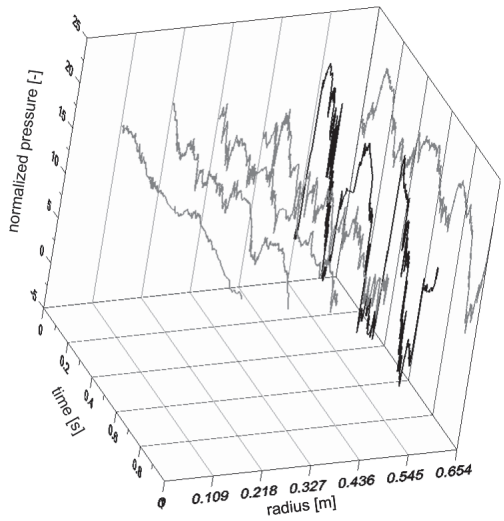


**Figure 58 – Time series as a function of radius – 12 MW**

A one second snapshot of the normalized pressure as a function of time and radius can be seen in Figure 58. The pressure is normalized by:

$$p_{norm} = \frac{p}{\frac{1}{2}\rho U^2} \tag{6.1}$$

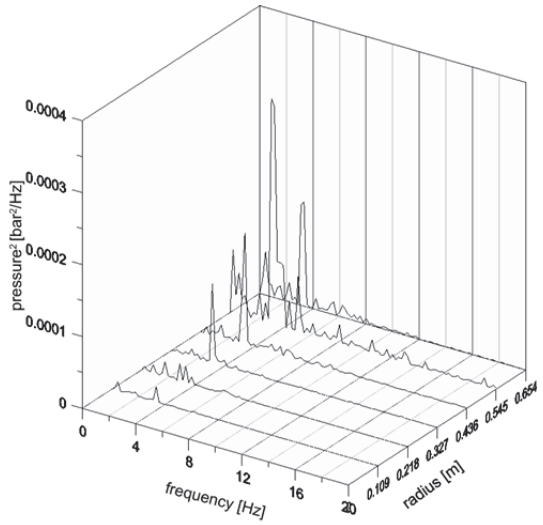


**Figure 59 – Frequency spectrum 0-20 Hz - 12 MW**

The frequency spectrum as a function of radius is shown in Figure 59 for the frequency range where the vortex rope is operating and where most of the energy is located.

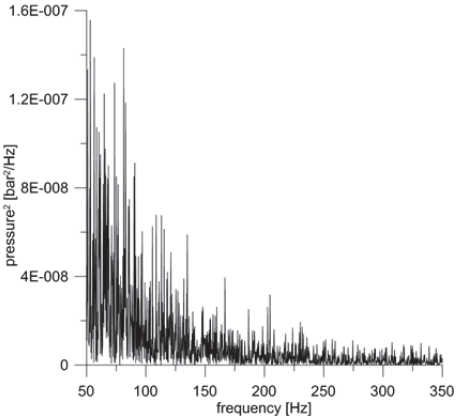


**Figure 60 – Frequency spectrum 50-350 Hz at draft tube wall, theta=60 deg – 12 MW**

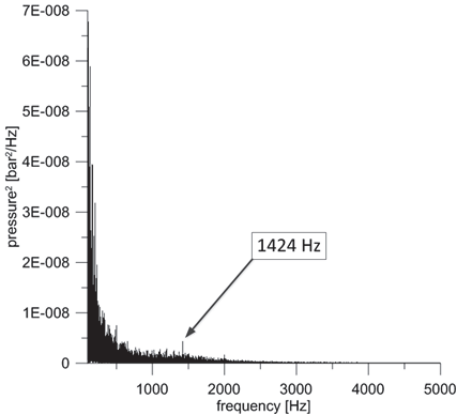


**Figure 61 - Frequency spectrum 100-5000 Hz at draft tube wall, theta=60 deg – 12 MW**

The frequency spectrum at the draft tube wall measured at theta=60 deg is presented in Figure 60 and Figure 61. The energy rapidly decreases from 0 to 200 Hz. To obtain better readability the first 100 Hz are left out in Figure 61 in search of dominant frequencies in the high frequency range.

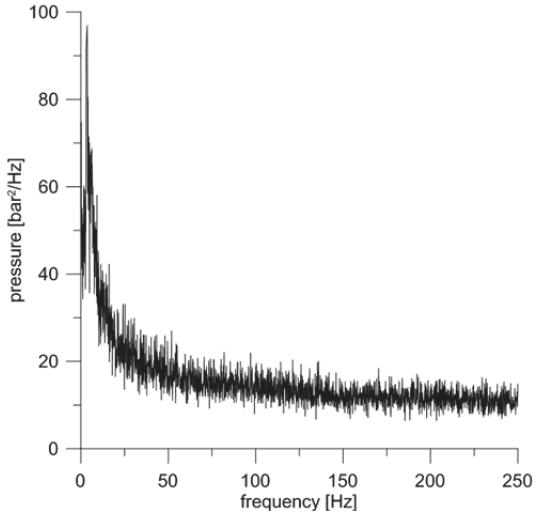


**Figure 62 – Energy spectrum of amplitude demodulation from 1000-5000 Hz at draft tube wall, theta=60 deg – 12 MW**

Figure 62 shows the energy spectrum of amplitude demodulation of the wall pressure signal for theta=60 deg.

### 6.4.4 Axisymmetric assumption

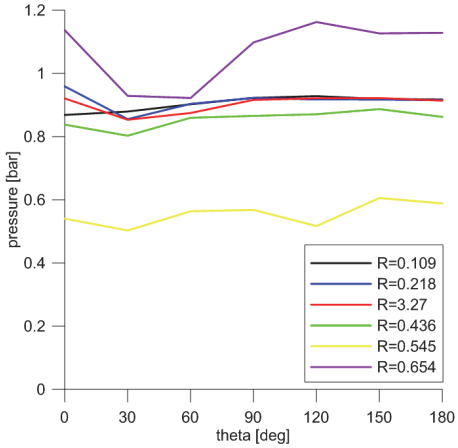


**Figure 63 – Mean pressure along theta**

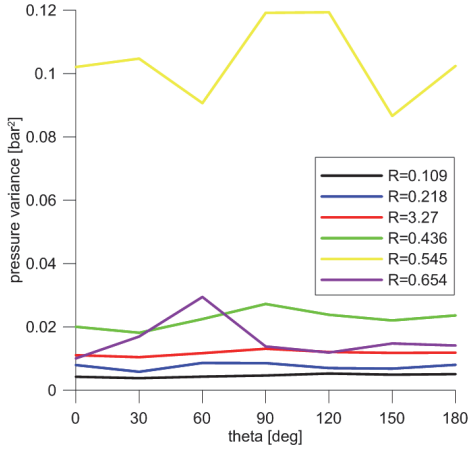


**Figure 64 – Pressure variance along theta**

The mean pressure and the pressure variance is plotted as a function of theta to check axisymmetry in Figure 63 and Figure 64 respectively.

### 6.4.5 Results from POD analysis

#### *6.4.5.1 Integral time scale*

In this case we obtain 20 integral time scale cycles in each block of 1 second when using average time scale of 0.05 seconds. The integral time scales measured in the draft tube are shown in Figure 65 and Figure 66.

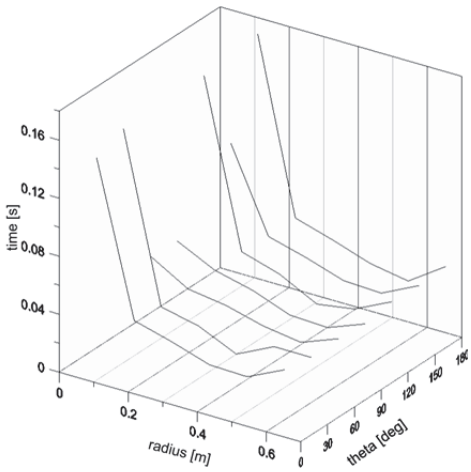


**Figure 65 – Integral time scale as function of theta and radius**

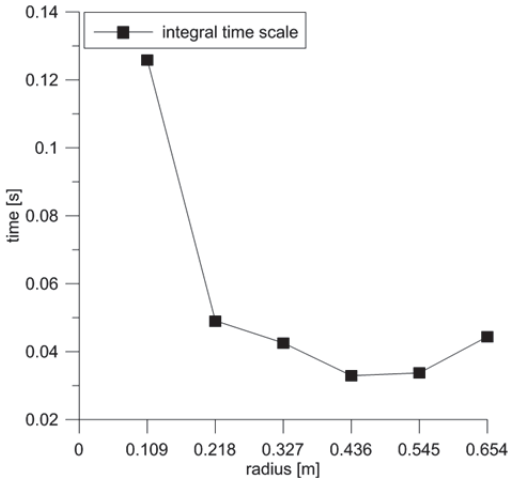


**Figure 66 – Integral time scale Λ as function of radius averaged over all angular positions**

### *6.4.5.2 POD properties*

| Tot data points | Λ | Blocks | Block length | Data points / block | Λ / block | POD modes |
|---|---|---|---|---|---|---|
| 900 000 | ≈0.05 s | 90 | 1 s | 10 000 | 20 | 6 |

**Table 7 – POD properties**

### *6.4.5.3 Spectrum along each azimuthal mode*

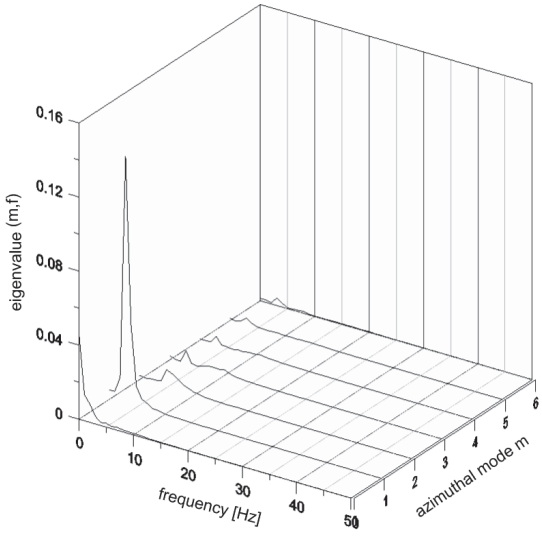


**Figure 67 – Summed eigenspectra over all positive POD modes along each azimuthal mode**

The summed eigenspectra over all POD modes are shown in Figure 67. Only positive eigenvalues are summed. Negative eigenvalues are set to zero. The spectrum is only shown in the range 0-50 Hz as the energy rapidly decrease for higher frequencies.

#### *6.4.5.4 Eigenvalue distribution over azimuthal modes*

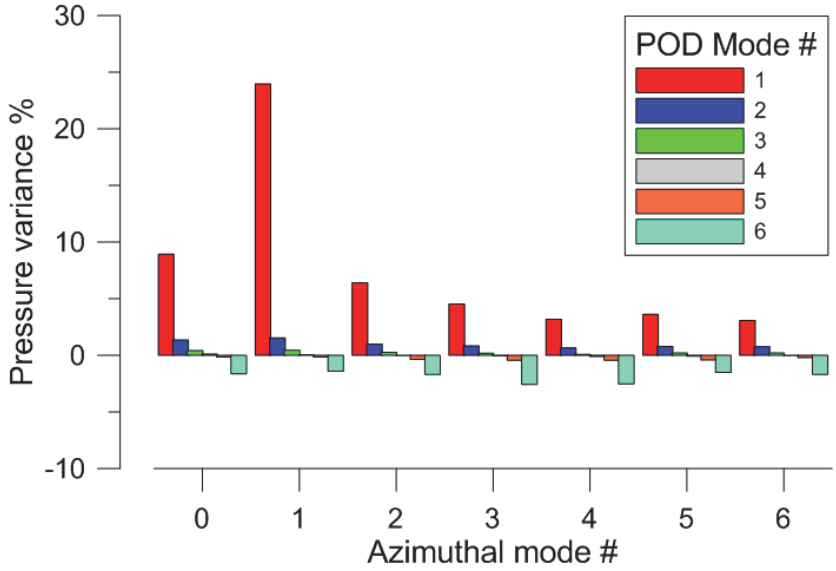


**Figure 68 – POD-modes along each azimuthal mode**

The eigenvalues representing the 6 POD modes at each azimuthal mode are shown in Figure 68. Note negative eigenvalues representing the later POD modes (4), 5 and 6. Because of symmetry, azimuthal mode 1-5 are identical and correspond to azimuthal mode 11-7, and the latter azimuthal modes are not shown, but they contribute to the total pressure variance in the flow. Therefore each eigenvalue in azimuthal mode 1-5 must be multiplied by 2 to obtain the correct pressure variance represented by the POD modes.

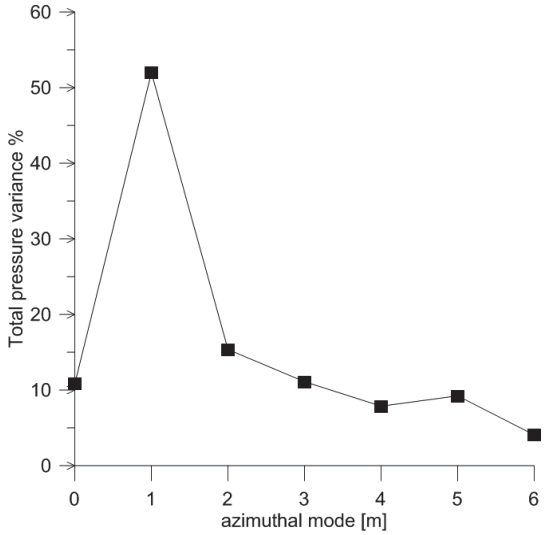


**Figure 69 – Sum of positive POD-modes**

Figure 69 shows the sum of the positive POD modes at each azimuthal mode. The pressure variance in the POD modes at azimuthal mode 11-7 are added to the pressure variance in azimuthal mode 1-5 respectively to show the total pressure variance distribution at each azimuthal mode.

# 7 Discussion

## 7.1 Discussion of wake study

### 7.1.1 Cylinder wake

The work on the cylinder wake [74] presents a new way of studying wake flow and rotor-stator interaction where experimental PIV data, CFD and POD are combined. This study investigates the wake from a cylinder at reference speeds in the range of 1-6 m/s.

Wake width and turbulence intensity width is found to be independent of the reference velocity, but the wake magnitude and turbulence intensity increase in amplitude with larger reference velocity. This is in accordance with reported [75] findings.

The leading edge stagnation pressure on the rotor is first expressed by the velocity diagrams in order to compare with the results from the CFD. The analytical model under predicts the CFD results with a factor of slightly less than 0.5. The mismatch can occur from interference from the potential field around the rotor with the stator wake velocity- and pressure field.

The standard deviation of the leading edge stagnation pressure and lift variation does not change much as the reference speed increase. Although U=1 m/s has a noticeable lower standard deviation. As expected, a synthetic wake where the wake is stationary and time averaged at all positions as input, gives significantly lower stagnation pressure- and lift fluctuations. This is clearly seen in the standard deviation plots, figure 22 and figure 23 in Paper 1. Synthetic wake was only simulated for U=4 m/s due to limited time.

The rotor-stator system is characterized by the blade passing frequency and the vortex shedding frequency. Both frequencies can be found when studying the leading edge stagnation pressure fluctuation (blade passing dominant), movement of the stagnation point (vortex shedding dominant) and in the lift fluctuations (blade passing dominant). Frequencies equal the sum of both and the difference between rotor passing and vortex shedding was also found but could not be related to any physical phenomenon.

The POD reveals the vortex shedding structures, and as much as 50-65 % of the total energy can be found in the two first POD modes. The two first modes are addressed to the shedding of alternating vortices off the cylinder. Vortex shedding energy is extracted through POD (the two first modes) and from the frequency spectrum of the v-component in the wake velocity field. The energy in the frequency spectrum is based on the average value from 12 x-positions and 15 y-positions. Comparison of the two energy extractions are made in Figure 24 with good coherence. The POD energy is in general found lower, but with similar trend as the reference speed change. As the POD decomposes the energy into finite POD modes, one can't assume POD mode 1 and 2 to capture exactly the energy amount associated with vortex shedding. Some of this energy can also be found at later modes. The plot in Figure 24 shows that it is reasonable to believe that the POD capture the majority of the energy related to vortex shedding in mode 1 and 2 when the vortex shedding is of significant size.

The method examines several aspects regarding wake flow and rotor stator interaction, and helps in understanding the behavior of a dynamic wake. It is important to better understand the dynamic wake behavior and the effects of it in order to better predict the true load on the turbine structure. Numerical simulations such as CFD are often used when designing turbines, but the load originating from the rotor-stator interaction is often modeled as a sinusoidal load. We want to demonstrate that one solution can be to use experimental wake data as input in order to obtain a more realistic flow through the turbine with respect to dynamics originating from wake flow. To develop the method, a cylinder wake is used as the dynamic wake behavior already is well known from previous studies. As the method is verified and tested for a known case it can further be used for more complex and realistic flow problems such as looking at the wake from a hydrofoil similar to a guide vane.

### 7.1.2 Hydrofoil wake

The investigation on wake flow and rotor-stator interaction from the hydrofoil wake [76] is based on the method developed by studying the cylinder wake. A NACA 0015 hydrofoil investigated in this study is similar to the guide vane shape used in Francis turbines. The results obtained in the cylinder study are of good help to better verify and understand the findings in this hydrofoil study.

While the cylinder was studied with respect to various reference velocities, the hydrofoil is studied with respect to various angle of attacks while the reference speed is held constant at U=9 m/s. It is also of major interest to study the effect of mounting vortex generators on the suction side of the hydrofoil.

Note that paper 2 [76] refers to various methods used to analyze the hydrofoil wake and the wake applied in a rotor-stator interaction case. Those are referred to as an analytical approach, implementation in CFD and the use of POD. The superior method developed in paper 1 [74] consist of those different analysis approaches, misleadingly also denoted methods in paper 2.

The time averaged wake profile along with turbulence intensity both increase in width when AoA is increased. The same effect is seen when introducing vortex generators at constant AoA. Regarding amplitude in the time averaged wake profile and turbulence intensity they both increase by increased AoA. When Introducing VGs, the time averaged wake profile decrease in amplitude for AoA=0 and AoA=2. At AoA=4 the amplitude is approximately constant, while it rise for AoA>4 when introducing the VGs. The turbulence intensity remains almost the same in amplitude with and without VGs up to AoA=4. For AoA=6 and higher the turbulence intensity profile also increase when VGs are introduced.

When studying the fluctuations in the wake, vortex shedding is only found at one case, AoA=8. Vortex shedding was expected to be found with various intensity at all AoAs. It is strange to only find vortex shedding at AoA=8. If there's a point where vortex shedding is triggered one would expect even larger structures to shed for increasing AoA as the flow moves towards separation. Even when the flow fully separates from the foil large structures are expected to shed, though at lower frequency.

The leading edge stagnation pressure on the rotor in the RSI-case is predicted by an analytical approach where the stagnation pressure is expressed by velocity components. The stagnation pressure is also monitored during the simulations. Time averaged stagnation pressure and the analytical approach for both plain- and V1-case are compared, but with poor coherence. While the analytical approach predicts a rise in stagnation pressure for increasing AoA,

the CFD shows the stagnation pressure to remain fairly constant for both cases with V1 somewhat higher than the plain case. Mismatch can occur from disturbances from the potential flow around the rotor which may affect the velocity- and pressure field upstream and around the rotor leading edge.

Standard deviation can be a good measure on the general variation in a signal. The standard deviation is plotted for leading edge stagnation pressure as well as for the lift variation for plain and V1 case. It shows that the pressure fluctuations are slightly lower or similar for the V1 case AoA=0 and AoA=2 degrees. At higher AoA the standard deviation increase when vortex generators are introduced. The dominant frequencies found in the leading edge stagnation pressure and lift variations is the rotor passing frequency. No shedding frequency is observed, although shedding is clearly observed when looking at the u or v-velocity component in the wake at AoA=8 for the plain case. As shedding is observed at AoA=8, as well as the finding of shedding frequencies in similar cylinder results, it was expected to observe the shedding frequency in the leading edge stagnation pressure and the lift variation for the hydrofoil wake. Especially at AoA=8 where shedding clearly is observed. It is of interest to note that the amplitude of the rotor passing frequency observed in the leading edge stagnation pressure and the lift fluctuations are higher for all AoAs for all VG cases. Multiples of the rotor passing frequency are visible for both fluctuations, and especially the $1^{st}$ multiple which is even more dominant than in the plain case for both the leading edge stagnation pressure and lift fluctuation.

Dynamics in the stagnation point location is also looked into. See Figure 25 and Figure 26. Both the rotor passing frequency and the vortex shedding frequency were discovered in the cylinder wake, with the latter as the more dominant. No vortex shedding frequency was discovered in the dynamics of the stagnation point in any hydrofoil wakes. Though, the rotor passing frequency and multiples are present in all cases. The amplitude also increase for the V1 case compared to the plain case. The results are surprising, as it was expected to discover the vortex shedding frequency in the stagnation point dynamics for AoA=8. The coarse frequency resolution and spectral leakage can be a reason for not observing the vortex shedding.

Applying the POD on the plain- and V1-case show similar results for all AoAs except for AoA=8. These cases show that the effect of the VGs is to slightly shift the energy in the early POD-modes to later POD modes. The energy is evenly distributed with only about 3 % of the energy in the first mode. This indicates that there are no large structures that contain the majority of the energy in the wake, and hence that there are no large structures that the vortex generators can break down into smaller structures. The POD showed odd and unphysical structures in POD-mode 1 for AoA=0 and AoA=6. In order to interpret the results correctly this mode has to be discarded. This has to be taken into consideration when studying the figures showing energy in mode 1-2 and 1-5 with and without VGs. When the $1^{st}$ mode in those cases are discarded the trend is similar to what found for AoA=2 and AoA=4. These poor results are most likely to originate from the process where PIV-pictures are converted to xy-coordinates and uv-velocity field in a small area just at the trailing edge of the hydrofoil.

For AoA=8 the POD analysis clearly shows larger structures which consist of significantly more energy in POD-mode 1 and 2 compared to the other cases for the plain hydrofoil. Approximately 18 % of the flow energy can be found in the two first modes, represented by the eigenvalues of the POD. POD has the nature to address vortex shedding to the two first modes as it is vortices alternating shed off the top and bottom side of the object. Comparison of the energy in mode 1 and 2 for plain- and V1-case show that the V1-case have reduced the energy in the two first modes to 9 %. The POD has proved to reveal vortex shedding for AoA=8 as well as showing that vortex generators can break down the structures with large energy at early modes and distribute the energy to later POD-modes.

Plotting of the eigenfunctions, which shows the structures, also confirms presence of vortex shedding for AoA=8, but not for the other AoAs where no large energy rich structures are found. Se Figure 27 to Figure 42.

The comparison between energy addressed to vortex shedding based on POD mode 1 and 2 (18 %), and the energy calculated from the average frequency spectrum of 12x15 x-y positions for plain case AoA=8 (20 %), show very good agreement. This procedure was also carried out at some singular points in the

wake with very similar results and supports the expectations that POD can reveal repetitive flow structures also of less magnitude than in the cylinder case shown earlier.

### 7.1.3 Advantages of the overall method

Since data are collected in a laboratory it is possible to set the appropriate conditions and investigate isolated phenomena so say free of disturbances that would be present in a full scale power plant. It is also much easier to measure on a small laboratory set-up.

The method investigates several important aspects in wake flow and rotor stator interaction. All aspects are used to obtain a better understanding of the dynamics present in wake flow and rotor-stator interaction.

The time averaged data showing velocity deficit and turbulence intensity give a good picture on how these properties change with increased reference velocity or angle of attack. The effect of mounting flow control devices as vortex generators is also seen clearly.

The method reveals the characteristic frequencies in terms of vortex shedding and rotor passing frequency when they are present in the cylinder case. Those frequencies are later found with different magnitude in the dynamics of the leading edge stagnation pressure, lift fluctuation and stagnation point movement.

POD has an important role in revealing the major flow structures energy wise which it prove to do well. It's results with respect to vortex shedding are also consistent with energy extracted from the frequency spectrum.

Comparing several analyses with and without vortex generators gives a good picture of the overall effect of those.

### 7.1.4 Disadvantages of the overall method

As the method is based on collecting experimental data from "ideal" conditions in a laboratory and later put into a simplified 2-D simulation model, there are several aspects that cause uncertainties and differences compared to a real full scale scenario.

Due to high Reynolds numbers, the flow is 3 dimensional. The 3-D effects and their magnitude are not possible to know as the measurement of the data and hence the simulation is in 2-D. It is difficult to tell how much important information that are lost due to this. The 3-D effects can describe the small observed mass flow variations at the rotor inlet between each time step which caused the case to be simulated compressible.

The attempt of describing the rotor leading edge stagnation pressure by velocity triangles have not proved to consist well with simulated results.

The fact of only experience vortex shedding at AoA=8 is questionable. Other studies has shown that this is somewhat present at all AoAs and it increase in magnitude as AoA increase.

Not all analysis are consistent of whether vortex generators are beneficial or not. Looking at std. deviation of the rotor leading edge pressure and the amplitude in the spectrum when introducing VGs, they increase in the case where vortex shedding is observed. Though, the POD shows that the VGs suppress the vortex shedding.

## 7.2 Discussion of draft tube study

### 7.2.1 Measuring procedure

There are several uncertainties and simplifications in the measurements. The pressure is always measured normal to the draft tube wall as the sensor was mounted flush at the end of the probe. Doing this it is not possible to distinguish static and dynamic pressure, since the direction of the flow is not known. As the measurements had to be prepared and carried out quickly with little down time on the power plant, we were restricted to a quick and simple measuring method. Both costs, time and space aspects made automated measurements inappropriate which is desired for many directional pressure measurements. Manual pitot measurements are possible, but very time consuming for many data points, so this option was also discarded. Even the pressure measurements are a mix of static and dynamic pressure, they give a good picture of the pressure fluctuations present in the draft tube. As the sensor is mounted flush at the end of the probe it experiences mostly flow

flowing perpendicular to the sensor, and the measured pressure signal is regarded close to static pressure. Manual traversing of the probe and possible positioning and angular errors of the drilled holes are sources of error. Experience from the measurements can estimate the radial position to be within 1 cm at each radial position. POD will anyway find the dominant structures in the signal, but one must remember what the signal represent. In this case a pressure force which an object in the flow will experience. For demonstration and first use of POD these measurements are regarded satisfying. For further use and development with POD more accurate measurements with separated static or dynamic pressure must be considered.

### 7.2.2 Pressure pulsations and characteristic frequencies

When studying p2p-values and standard deviation in pressure at various R as presented in Figure 54 and Figure 55 respectively, it is obvious that the pressure pulsations increase in magnitude for larger R with a peak at R5=0.545 m. The draft tube wall pressure at R6 is at level with R4. These results indicate that a strong swirl is present rotating with the core close to R5. It is difficult to tell whether the swirl is a cavitated vortex rope and the exact size.

The contour plots of the mean pressure and standard deviation of the pressure in Figure 56 and Figure 57 show how mean pressure and fluctuation magnitude is in the draft tube plane. They both show larger deviations in magnitude at R5 and also at R6 at the draft tube wall. This also clearly indicates that a strong fluctuating swirl is present, rotating in the area around R5.

The characteristic frequencies in terms of rotational frequency, blade passing frequencies and Rheingans frequency are presented in Table 6. Frequency spectrum of the pressure at various R in Figure 59 shows that the Rheingans frequency at approximately 3.2 Hz is present at all R with a peak at R5. This frequency is in good agreement with expected Rheingans frequency.

Neither the rotational speed frequency at 10 Hz, nor any of the blade passing frequencies at 150 and 200 Hz are found as distinct peaks in the frequency spectrums. See Figure 59 and Figure 60 for the frequency spectrum at the wall, R6. The frequencies were neither found at other radial positions. It is likely to believe that higher frequency oscillations originating from inside the turbine

will be attenuated and suppressed by the dominating dynamics of the vortex rope. A small peak is noticed at 1424 Hz. A simple prediction shows that this can be vortex shedding from any of the 3 vanes, but as it is small in amplitude it is most likely to be noise.

Figure 62 shows the energy spectrum of amplitude demodulation of the wall pressure signal for theta=60 degrees from 1000-5000 Hz. By demodulating the amplitude in the frequency spectrum at a given band it is possible to see if the fluctuations in this frequency band are modulated by lower frequencies. The frequencies in the range of 1000-5000 Hz are only found to be modulated by the vortex rope at 3.2 Hz as this is the only distinct peak in Figure 62. Here one could also expect to see the rotational speed frequency (10 Hz) as well as the blade passing frequencies (150 and 200 Hz), but there are no signs of those frequencies modulating the high frequency fluctuations. This method can be used to reveal cavitation which give frequency fluctuations in the range 10-20 kHz.

### 7.2.3 Integral time scale

The integral time scale is presented as a function of radius and theta in Figure 65 and as an averaged value over all angular positions in Figure 66. The integral time scale show similar values along the radius with high values (0.14 seconds) at R1 and rapidly decreasing to below 0.05 seconds at larger radius. Theta 60, 90 and 150 does not show the large values at R1. Pressure fluctuations at R1 are lower in magnitude than at higher radius and less distinct fluctuations are observed. See Figure 58 and Figure 59. The longer integral time scale is believed to be in connection with the steadier motion observed at low radius.

Integral time scale calculation is important for deciding the block length which the total record is divided into. Different block lengths were tried out. Longer block lengths give the benefit of higher frequency resolution and better convergence of the statistics which is necessary for precise results. Only data separated by 2 times the integral time scale gives additional information about the structures in the flow. As the total record length is given, 90 seconds in this case, it is important to find the balance between block length and number of blocks. Very long record lengths would not result in compromising block lengths and number of blocs as in this case, but measuring time at the power plant was

limited. Many blocks are important to have converging statistics, and reduces the uncertainty. Block lengths of 1, 2, 5 and 9 seconds were tried out, resulting in corresponding 90, 45, 18 and 10 blocks. Longer blocks resulted in higher frequency resolution and better match between frequency peak in the eigenspectra and the Rheingans frequency discussed in chapter 7.2.5. The major disadvantage of the increased block length was the formulation of larger negative eigenvalues at POD mode (4), 5 and 6. When summing the eigenvalues (pressure variance) over all azimuthal modes the total sum deviated more from 100 % when the block length increased. At 9 seconds block length the total pressure variance summed to 150 %. Only positive eigenvalues are summed, and the negative ones are set to zero. At 1 second block length the eigenvalues summed up to 110.5 % total pressure variance when excluding the negative eigenvalues. Increasing the block length did not give much change in the eigenspectra, except from higher absolute values. To keep the negative eigenvalues as small as possible and to reduce the uncertainty, 1 second block lengths were chosen. Shorter block length would give very poor frequency resolution, and capture less than 3 revolutions of the vortex rope.

### 7.2.4 Axisymmetry

The draft tube flow was assumed axisymmetric of practical reasons related to method complexity and time/space limitations on site mentioned in chapter 2.7.3. Axisymmetry means that the pressure is homogenous in the azimuthal direction, meaning mean pressure is equal at any angular position for a given radius. Figure 63, a plot of the mean pressure along theta and Figure 64, a plot of the standard deviation of the pressure along theta show that the axisymmetric assumption is reasonable for most radiuses. Mean pressure deviates the most at the wall (R6) while the standard deviation of the pressure deviates most at R5 where the strong swirl or vortex rope is travelling.

### 7.2.5 Summed eigenspectra over positive POD modes

Solving the POD results in eigenvalues as a function of POD modes (n), frequency (f) and azimuthal modes (m). Figure 67 shows the summed eigenvalues (n) over all positive POD modes, referred to as eigenspectra, as a function of frequency and azimuthal mode. As can be seen in Figure 68 some eigenvalues are negative. They are set to zero in this summation. The dominant POD mode is mode 1. This means that the pressure variance in eigenvalue 1 is

associated with a change in pressure propagating in the same direction over the radius. See Figure 18 for detailed description.

The peak observed in the spectrum is the Rheingans frequency at 3.2 Hz. It is observed in all azimuthal modes, except azimuthal mode 0, see Figure 19. For azimuthal mode 0 the spectrum shows higher energy as the frequency approaches zero. The spectrum attenuates for higher frequencies. This indicates that very low frequency fluctuations drive the vertical pressure motion represented by azimuthal mode 0. Zero frequency is the average value of the signal, and a peak here indicates a constant change in pressure at azimuthal mode 0.

For the other motions represented by azimuthal mode 1-6 the Rheingans frequency is the dominant source of motion. No other distinct peaks are observed, and the energy is rapidly decreasing for higher frequencies. Therefore only 0-50 Hz spectrum is shown. Although the Rheingans frequency is visible at all azimuthal modes greater than 0, it is very dominant in azimuthal mode 1. This implies that the Rheingans frequency is a very important factor for experiencing pressure fluctuation across the cross section as shown in Figure 19 for azimuthal mode 1.

As the block length had to be reduced to only 1 seconds, the frequency resolution is poor, only 1 Hz. The frequency peaks in Figure 67 do not perfectly correspond with 3.2 Hz, but they are close (2-4 Hz). The poor frequency resolution is blamed for not hitting spot on. The Rheingans frequency is the only distinct frequency found in earlier analysis of the time pressure signal and expected to be found in the eigenspectra.

### 7.2.6 Eigenvalue distribution over azimuthal mode

Eigenvalues (POD modes) are plotted as a function of azimuthal mode in Figure 68. This figure shows how the pressure variance is distributed over the different azimuthal modes and the motion they represent shown in Figure 19. Because of the symmetry condition, azimuthal mode 1-5 are identical to azimuthal mode 11-7 respectively, and the latter azimuthal modes are not shown. It is clear that POD mode 1 is most dominant at all azimuthal modes. Summation of the positive POD modes in azimuthal mode 1 which is by far most dominant of

the azimuthal modes show that 26 % of the pressure variance is found in azimuthal mode 1. As this mode is equal to azimuthal mode 11, the pressure variance can be summed twice to obtain the total contribution. Hence, 52 % of the total pressure variance is addressed to azimuthal mode 1. Looking at the eigenspectra in Figure 67, which mainly consist of the contribution from POD mode 1, it is clear that the Rheingans frequency is the major executer of the azimuthal mode 1 motion. The energy plotted in Figure 69 is compensated for the effect of symmetry condition and shows the total pressure variance contribution from azimuthal mode 0-6.

Note that the values in Figure 68 and Figure 69 are plotted as they occur from the POD directly, and are not compensated for the uncertainty of the negative eigenvalues discussed in chapter 7.2.3.

By addressing large pressure variation portions to given azimuthal modes it is possible to determine the dominant pressure motions. This is important to know in order to implement possible flow control. If one is able to remove the azimuthal mode 1 by flow control, close to 50 % of the total pressure pulsations can be suppressed.

The results must be interpreted with the axisymmetric assumption in mind. The validity of the axisymmetric assumption will increase as the operational point approaches BEP. In this work, results from partial discharge (48% load) only is shown. Based on previous publications [67, 68, 77] the assumption is regarded fair in the area of interest for draft tube flow at partial discharge. The flow field exiting the runner is very close to axisymmetric, but develops to a less axisymmetric flow further down in the draft tube. Especially at part load where a strong swirl or vortex rope is present, the swirl develops away from the draft tube center and approaches the wall. Further, when the flow goes through the draft tube, the vortex rope will reach vortex breakdown and enter a turbulent transition area where the vortex develop from a consistent cavitated vortex to bubbly flow.

### 7.2.7 Eigenfunctions

The eigenfunctions resulting from the POD analysis are not given attention in this work. They can be used together with the eigenvalues to reconstruct the

original pressure signal. What is more of interest, is to couple them with wall pressure sensors. By doing this it is possible to obtain POD results “real time” for other operational points where one full mapping of the pressure field as presented in this work works as a calibration. Real time POD results can be valuable as a controlling parameter in “flow control” applications. Looking into the eigenfunctions and further implementation for use in active flow control is discussed in the further work chapter, 9.

## 7.3 What do the wake- and draft-tube study have in common?

This work covers two main topics within secondary flow fields in Francis turbines:

- **Wake flow/rotor-stator interaction**
- **Draft tube flow**

both topics are extensive and could be studied more thorough independently. The wake/rotor-stator phenomena is located before the runner, while the draft tube flow is after the runner making them separate phenomena. Though it is likely to expect them to somehow influence each other. It is believed that the blade passing pressure or vortex shedding can propagate down to the draft tube, as well as draft tube pressure pulsation can cause mass flow fluctuations propagating up through the runner to the inlet. The wake/rotor-stator study was isolated, so it could not be influenced by the draft tube flow. The draft tube study could have been influenced by blade passing and dynamics occurring at the turbine inlet, but no clear signs of that was observed in this work. The two phenomena are important to understand independently in addition to their influence on each other. They have both been major source of cracks, and at worst structural failure in several turbines.

This work introduces new ways of analyzing secondary flow field issues. The wake study takes advantage of combining advanced flow mapping tools as the TRPIV with CFD. This combination makes it possible to utilize experimental data in an efficient way with CFD. Combining these analysis with traditional analysis methods gives a wider background and base to understand the flow phenomena.

Another approach is to map the flow or pressure field of interest and get an overview of the dominant structures present in the field. This is the strength of POD analysis applied both on the wake study and in the draft tube study. POD has been used extensively in classical turbulence research, but is little used in industrial applications. The POD can help understanding the dynamic flow field better. By addressing pressure variance in the field of interest to given POD- and azimuthal modes, it is possible to manipulate the given modes by flow control applications.

The two different flow phenomena were chosen because of their high importance in the Francis turbine in addition to high level improvement potential. Experimental data was also easy to access for both wakes and in the draft tube. Working with two different problems was a good chance to develop knowledge and experience using POD on different applications, which the author nor any of the research group at NTNU had previous experience with. Further development and use of POD in the study of industrial flow applications is believed to have a high potential.

# 8 Conclusions

## 8.1 Conclusions on wake flow and RSI

A method to investigate wake flow and rotor-stator interaction by a combination of experimental data, CFD and POD have been developed and applied on a cylinder wake- and a hydrofoil wake case.

Characteristic frequencies of the system are found to be the vortex shedding frequency and the rotor passing frequency.

Vortex shedding is always present in the cylinder wake, but only found at AoA=8 in the hydrofoil wake.

For the cylinder case, the vortex shedding frequency is the dominant frequency in the dynamics of the stagnation point and the lift fluctuations, while the rotor passing frequency is most dominant for the stagnation pressure dynamics.

The rotor passing frequency is the dominant frequency found in stagnation point, stagnation pressure and lift fluctuations for the hydrofoil case.

Vortex generators do in general increase wake dynamics, except for very low AoA where they perform equal to plain foil results.

Vortex generators prove to break vortex shedding structures where this is present at AoA=8.

POD reveals if energy rich structures are present in the flow, and addresses the energy content related to those structures with good accuracy.

## 8.2 Conclusions on draft tube flow

Dynamic pressure measurements are carried out in the draft tube at Svorka power plant running at 12 MW (48 % load).

Pressure fluctuations are found to be very dependent on the radius with a peak at R5 at 83 % of the radius.

The Rheingans frequency originating from a rotating vortex rope is found at 3.2 Hz – in good agreement with expected findings.

There are no sign of frequencies connected to rotational speed (10 Hz) or blade passing (150 and 200 Hz) in any analysis methods.

POD is applied on the dynamic pressure data and 52 % of the pressure pulsation variance is addressed to azimuthal mode 1.

A base set of POD results are obtained which can be used in techniques to obtain real time POD results. Real time POD may work as input parameter in active flow control applications.

# 9 Further work

A natural continuation of the work on wake flow and rotor-stator interaction will be to continue PIV measurements of the hydrofoils with increased range of AoAs. As complete stall was not experienced in the data presented here, PIV measurements should be completed on wake data for remaining AoAs until full stall is obtained and analyzed with similar methods as presented in this work. Vortex generators can also be implemented on the guide vanes in a model turbine in the laboratory to investigate the effect of pressure pulsations on a model turbine. As the vortex generators only show improved results in given operation modes, effort can be put in investigating the possibilities of adaptive flow control methods with similar effects as the vortex generators.

The radial dynamic draft tube measurements have so far only been measured at one operation point (12 MW), and mapping of more operation points would be of interest.

The draft tube measurements performed and presented can help determining damaging and unwanted operation points of the Francis turbine. An active flow control method which injects water contra rotary into the draft tube has been developed by Kjeldsen and Francke [53] to reduce pressure pulsations and cavitation occurring at part load operation. The system is automated in order to be applied when needed only. A set of parameters have been pointed out to determine when the water injection system shall be activated. The parameters, such as draft tube wall pressure pulsations and shaft vibrations are real-time monitored. It is desired to perform measurements and the POD analysis when the water injection is in operation to compare results with no water injection activated.

Using POD in draft tube flow can be developed further by taking advantages of experiences made in this study. The POD accuracy should be improved by longer record lengths which can give more data blocks for improved accuracy. Negative eigenvalues should be removed or minimized. Experience from this work shows that more data blocks help on that. Longer data series also give room for higher resolved frequency spectrum by increasing the block length. POD should also be applied at other operational points in order to compare

results. Maybe characteristic frequencies from the rotational speed or blade passing will show up at other operational points.

The POD method presented in the thesis can give valuable information about flow patterns present in a draft tube of a Francis turbine. To obtain a good picture of the true pressure field, the eigenfunctions have to be back projected onto the original pressure field. Then it is possible to study the shape of the pressure field, and also to relate it to the velocity field inside the draft tube. To better understand the physics occurring in the draft tube from POD, it would be of interest to map several horizontal planes to see how axisymmetry and dominant structures develop from close to the runner outlet to past the bend.

This has been a first step to apply the measurement technique on a draft tube flow. The POD-results can possibly work as another determining parameter for flow control applications such as the water injection system or other hydro power surveillance systems. Since the measurements are complex and very time consuming, it is difficult to directly implement the method in a real-time surveillance system. By mapping the flow field as presented in this work, the resulting eigenfunctions from the POD analysis can be coupled with a single pressure sensor in the draft tube as a calibration. From this coupling it is possible to extract new corresponding eigenvalues from a single wall mounted pressure sensor, and then obtain the POD results at other operation points. The method is called Linear Stochastic Estimation - LSE and is yet to be investigated further for this application. See [78, 79] for background and details on use of the LSE method. A further study on implementation of LSE can both be studied in the laboratory and in the full scale power plant at Svorka.

# Bibliography


1. Energidepartementet, O.o. *Energi i Norge*. 2012; Available from: http://www.regjeringen.no/nb/dep/oed/tema/fornybar-energi.html?id=86981.
2. Brekke, H., *Pumper & Turbiner.* Kompendium, 2003.
3. Antonsen, Ø., *Unsteady flow in wicket gate and runner with focus on static and dynamic load on runner*, in *EPT, Vannkraftlaboratoriet*2007, NTNU.
4. Chen, X., *Theoretical and experimental Study of flow through the double cascade of a Francis Turbine*, 1992, NTNU.
5. Larsson, C., *Experimental and theoretical analysis of inlet flow of a Francis Turbine Runner*, 2003, NTNU.
6. Jernsletten, J., *Analysis of a non- stationary flow in a Francis reversible pump turbine runner*, 1995, NTH.
7. Kobro, E., *Measurement of pressure pulsations in Francis turbines*, 2010, Norges teknisk-naturvitenskapelige universitet: Trondheim. p. 1 b. (flere pag.).
8. Vekve, T., *An experimental investigation of draft tube flow.* 2004(NTNU-EPT).
9. Oledal, M., *Cavitation in complex separated flows*, in *Faculty of Engineering Science and Technology*2002, Norwegian University of Science and Technology: Fakultet for ingeniørvitenskap og teknologi. p. 133.
10. Ausoni, P., *Turbulent vortex shedding from a blunt trailing edge hydrofoil*, 2009: Lausanne.
11. Ausoni, P., *Hydrofoil roughness effects on von karman vortex shedding*, in *2nd IAHR International Meeting of the Workgroup on Cavitation and Dynamic Problems in Hydraulic Machinery and Systems*2007: Timisoara, Romania.
12. Zobeiri, A., *Vortex shedding from blunt and oblique trailing edge hydrofoil*, in *3rd IAHR International Meeting of the Workgroup on Cavitation and Dynamic Problems in Hydraulic Machinery and Systems*2009: Brno.
13. Zobeiri, A., *Experimental investigation of the vortex shedding in the wake of oblique and blunt trailing edge hydrofoil using PIV-POD.* 2010.
14. Heskestad, G. and D.R. Olberts, *Influence of trailing-edge geometry on hydraulic-turbine-blade vibration resulting from vortex excitation.* Journal of Engineering for Power, 1960. **82**: p. 8.

15. Vu, T.C., et al., *Unsteady CFD prediction of von Kármán vortex shedding in hydraulic turbine stay vanes.* 2007.
16. Münch, C., et al., *2D oscillating hydrofoil*, in *2nd IAHR International Meeting of the Workgroup on Cavitation and Dynamic Problems in Hydraulic Machinery and Systems*2007: Timisoara, Romania.
17. Escaler, X., et al., *Cavitation monitoring of hydro turbines: Tests in a Francis turbine model*, in *Supporting Information for EPAPS - Whale flippers*2006.
18. Munch, C., et al., *Hydro elastic behaviour of vibrating blades*, in *24th IAHR Symposium on Hydraulic Machinery and Systems*2008.
19. Ausoni, P., et al., *Cavitation influence on von Karman Vortex Shedding and induced hydrofoil vibrations.* JOURNAL OF FLUIDS ENGINEERING, 2007. **129**.
20. Ausoni, P., et al., *Kármán vortex shedding in the wake of a 2D hydrofoil: Measurement and numerical simulation*, in *IAHR Int. Meeting of WG on Cavitation and Dynamic Problems in Hydraulic Machinery and Systems*2006: Barcelona.
21. Ausoni, P., et al., *Cavitation effects on fluid structure interaction in the case of a 2D hydrofoil*, in *2005 ASME Fluids Engineering Division Summer Conference*2005: Houston.
22. Arndt, R.E.A., *Cavitation in vorticial flows.* Annu. Rev. Fluid Mech, 2002.
23. Barbri, C., D.P. Favier, and C.A. Maresca, *Vortex shedding and lock-on of a circular cylinder in oscillatory flow.* J. Fluid Mech., 1984. **170**: p. 527-544.
24. Mutschke, G., et al., *Separation control at hydrofoils using Lorentz forces.* European journal of Mechanics B/Fluids, 2006. **25**.
25. Miklosovic, D.S., et al., *Leading-edge tubercles delay stall on humpback whale (Megaptera novaeangliae) flippers.* Physics of Fluids, 2004. **16**(5).
26. Nierop, E.A.v., S. Alben, and M.P. Brenner, *How Bumps on Whale Flippers Delay Stall: An Aerodynamic Model.* 2008.
27. Lumley, J.L., *Interpretation of Time Spectra Measured in High-Intensity Shear Flows.* Physics of Fluids, 1965. **8**: p. 1056-10-62.
28. Lumley, J.L. and P. Bakewell, *Viscous sublayer and adjacent wall region in turbulent pipe flow.* The Physics of Fluids, 1967. **10**(9): p. 1880-1889.
29. Lumley, J.L., *Structure of Inhomogeneous Turbulent Flows.* Atmospheric turbulence and radio wave propagation, 1967: p. pp. 166-176.
30. George, W.K., *Insight into the Dynamics of Coherent Structures from a Proper Orthogonal Decomposition.* Structure of Near Wall Turbulence, Proceedings of Symposium on Near Wall Turbulence, 1988: p. 168-180.

31. Glauser, M.N. and W.K. George, *Orthogonal Decomposition of the Axisymmetric Jet Mixing Layer Including Azimuthal Dependence.* Advances in Turbulence, 1987: p. 357-366.
32. Glauser, M.N. and W.K. George, *A Dynamical Systems Model for the Axisymmetric Jet Mixing Layer*, in *Proceedings 10th Australian Fluid Mechanics Conference*1987.
33. Glauser, M.N., S.J. Leib, and W.K. George, *Coherent Structures in the Axisymmetric Turbulent Jet Mixing Layer.* 1984.
34. Tutkun, M., *Three component vertical proper orthogonal decomposition of velocity profile behind a disk.* 2008.
35. Sirovich, L., M. Kirby, and M. Winter, *An eigenfunction approach to large scale transitional structures in jet flow.* 1990.
36. Arndt, R.E.A., *The proper orthogonal decomposition of pressure fluctuations surrounding a turbulent jet.* 1997.
37. Arndt, R.E.A., *POD notes*, 2010.
38. Lu, L.J. and C.R. Smith, *Velocity profile reconstruction using orthogonal decomposition.* Experiments in Fluids, 1991. **11**: p. 247-254.
39. Francke, H.H., et al., *Kompendie i Høytrykks Vannkraftmaskiner*, 2009.
40. Kjølle, A., *Vannkraftmaskiner*, Universitetsforlaget, Editor 1980.
41. Kjølle, A., *Hydropower in Norway - Mechanical Equipment*, 2001.
42. White, F.M., *Fluid mechanics*. 5th ed2003, Boston: McGraw-Hill. xiii, 866 p.
43. Çengel, Y.A., J.M. Cimbala, and M. Kanoğlu, *Fluid mechanics: fundamentals and applications*2010, Boston: McGraw-Hill. XXV, 980 s.
44. *Aerospace.org*. 2012; Available from: http://www.aerospaceweb.org/question/aerodynamics/q0228.shtml.
45. *Turbulent cylinder wakes*. 2012; Available from: http://electron6.phys.utk.edu/101/CH6/Turbulent%20wakes.htm.
46. Schlichting, H., K. Gersten, and K. Mayes, *Boundary-layer theory*2000, Berlin: Springer. XXIII, 801 s.
47. Seim, B.G., *Study of hydrofoil wakes using PIV and CFD*, 2009, NTNU: Trondheim.
48. Sience, W., *Weird Clouds Look Even Better From Space*, 2012.
49. 7, L., *von Karman vortices*, 2012.
50. Lockey, K.J., et al., *Flow induced vibrations at stay vanes: Experience at site and CFD simulation of von Karman vortex shedding*, 2006.
51. *Strouhal number vs Reynolds number*. 2012; Available from: http://hmf.enseeiht.fr/travaux/CD0102/travaux/optmfn/gpfmho/01-02/grp6/pages/strouhal.htm.

52. Nicolet, C., N. Ruchonnet, and F. Avellan, *One-Dimensional Modeling of Rotor Stator Interaction in Francis Pump-Turbine*, in *23rd IAHR*2006: Yokohoma.
53. Francke, H.H., *Increasing hydro turbine operation range and efficienciesusing water injection in draft tubes*, 2010, Norges teknisk-naturvitenskapelige universitet: Trondheim. p. VI, 147 s.
54. Dahlhaug, O.G., *Draft tube swirl*, 2009: NTNU, Vannkraftlaboratoriet.
55. Jacob, T., J.-E. Prènat, and G. Buffet, *Improving the stability of operation of a 90 MW francis turbine.* 1995.
56. Reisiga, S., et al., *Jet control of the draft tube vortex rope in francis turbine at partial discharge.* 2006(23rd IAHR Symposium - Yokohama).
57. Gearhart, W.S., A.M. Yocum, and T. Seybert, *Studies of a method to prevent draft tube surge in pump-turbines.* 1978. **TM-78-56**.
58. Rheingans, W.J., *Power Swings in Hydroelectric Power Plants.* Transactions of ASME, 1940. **62**.
59. Instruments, N., *Labview Manual*, N. Instruments, Editor 2008.
60. Haugan, K., *Trykkpulsasjoner I francisturbiner.* 2007(NTNU-EPT).
61. O'Neill, P.L., et al., *Autocorrelation functions and the determination of integral length with reference to experimental and numerical data*, in *15th Australasian Fluid Mechanics Conference*2004: The University of Sydney, Australia.
62. Tutkun, M., *Structure of Zero Pressure Gradient High Reynolds Number Turbulent Boundary Layers*, 2008, Chalmers University of Technology.
63. Tropea, C., A.L. Yarin, and J.F. Foss, *Springer Handbook of Experimental Fluid Mechanics*. Vol. 1. 2007: Springer.
64. Hilberg, D., W. Lazik, and H.E. Fiedler, *The application of classical and snapshot POD in a turbulent shear layer with periodic structures.* Applied Scientific Research, 1993. **53**.
65. Hilberg, D., W. Lazik, and H.E. Fiedler, *The Application of Classical POD and Snapshot POD in a Turbulent Shear Layer with Periodic Structures.* Applied Scientific Research, 1994. **53**: p. 283-290.
66. Xiano, H. and J. Li, *Unsteady Calculation in Hydraulic Turbine Induced by Rotor Stator*, 2009, School of Power and Machinery Engineering.
67. Susan-Resiga, R., et al., *Axisymmetric swirling flow simulation of the draft tube vortex in Francis turbines at partial discharge*, in *IAHR*2008: Iguassu.
68. Kirschner, O., et al., *Swirling flow in a straight cone draft tube: Axisymmetric flow analysis and comparison with circumferentally averaged PIV measurements*, in *IAHR international meeting of the workgroup on cavitation and dynamic probles in hydraulic machinery and systems*2007: Timisoara.

69. J.Delville, *Characterization of the Organization in Shear Layers via the Proper Orhogonal Decomposition.* Applied Scientific Research, 1994. **53**: p. 263-281.
70. Johansson, P.B.V. and W.K. George, *Proper orthogonal decomposition of an axisymmetric turbulent wake behind a disk.* Physics of Fluids, 2002. **14**: p. 2508-2514.
71. Wosnik, M. *Description of SAFL high speed water tunnel and experimental equipment*. 2005; Available from: http://cav.safl.umn.edu/facilities.htm.
72. MIT. *Xfoil*. 2012; Available from: http://web.mit.edu/drela/Public/web/xfoil/.
73. *Svorka Produksjon*. 2011; Available from: http://produksjon.svorka.no/index.php/produksjonsanlegg/svorka-kraftverk.
74. Finstad, P.H.E., M. Kjeldsen, and R.E.A. Arndt, *Method for Characterizing Rotor Stator Interaction Using Experimentally Obtained Wake Flow Fields and CFD*, 2011, NTNU - Vannkraftlaboratoriet: Trondheim.
75. Chibana, M. and W. Kay, *Hot wires, wakes and drag measurement*, 2004: Purdue University School of Aeronautics and Astronautics.
76. Finstad, P.H.E., M. Kjeldsen, and R.E.A. Arndt, *Characterizing rotor-stator interaction - RSI in hydrofoil wake using CFD and experimentally obtained wake flow fields*, in *ISROMAC 14*2012: Honolulu.
77. Susan-Resiga, R., et al., *Three-dimensioal versus two dimensional axisymmetric analysis for decelerated swirling flows*, in *Conference on modelling fluid flow*2009: Budapest.
78. Bonnet, J.P., et al., *Stochastic estimation and proper orthogonal decomposition: Complementary techniques for identifying structure.* Experiments in Fluids, 1994. **17**.
79. Hudy, L.M., A. Naguib, and W.M. Humphreys, *Stochastic estimation of a separated-flow field using wall-pressure-array measurements.* Physics of Fluids, 2007. **19**.

# Appendix

## Misprint in Paper 2

Note that there is a misprint in paper 2, "*Characterizing rotor-stator interaction - RSI in hydrofoil wake using CFD and experimentally obtained wake flow fields*" [76] on page 2, column 2 where it says the vortex generators are mounted in the rear section of the suction side. They are mounted at x/k=0.38 which corresponds to a position closer to the hydrofoil leading edge than the trailing edge.